ABSTRACT

Title of Dissertation:	REGIONAL PREFERENCES IN THE SEASONAL AND MULTIDECADAL LOSS OF ARCTIC SEA ICE: THE ROLE OF CONTINENTAL RUNOFF
	Rebecca Elaine Eager, Doctor of Philosophy, 2022
Dissertation directed by:	Professor Sumant Nigam, Department of Atmospheric and Oceanic Science
	Associate Research Professor Alfredo Ruiz-Barradas, Department of Atmospheric and Oceanic Science

Arctic sea ice is of great importance as both a key indicator and a driver of climate change. Sea ice is highly sensitive to temperature changes of the overlying atmosphere and the underlying ocean. The declining trend of Arctic sea ice, especially in late summer when seasonal ice extent is also a minimum, is widely considered a key indicator of the global warming of the planet. This dissertation finds that the observed trends in late summer Arctic sea ice are greatly impacted by natural decadal-to-multidecadal climate variability, mainly by sea surface temperature variability in the Atlantic and Pacific Oceans. The Atlantic Multidecadal Oscillation and Pacific Decadal Variability – via a Pan Pacific mode – each contribute a loss of 3-4% of sea ice concentration (SIC) per decade to the overall loss of 24% per decade since 1979.

To better understand the mechanisms driving these trends, the impact of decadal and multidecadal climate variability on the Arctic atmosphere, ocean, and continental hydrology is investigated. Multidecadal climate variability leads to regional and seasonal impacts on atmospheric circulation, ocean heat content, and ocean salinity that vary across the Arctic. Modification of the atmospheric circulation on decadal and multidecadal time scales impacts warm inflow into the Arctic from the North Atlantic and North Pacific, and also leads to redistribution of sea ice in the Arctic.

Vertical profiles of ocean temperature and salinity near the mouth of the Arctic rivers provides a means to investigate the impact of variability in continental hydrology on the Arctic marginal seas through the input of freshwater and heat. In the Beaufort Sea, the Atlantic Multidecadal Oscillation leads to increased ocean temperatures and decreased ocean salinity at the mouth of the Mackenzie River, corresponding in time to the annual June peak in river discharge. Finally, the impact of Mackenzie River discharge variability on the freshwater content, temperatures, and SIC in the Beaufort Sea is assessed.

REGIONAL PREFERENCES IN THE SEASONAL AND MULTIDECADAL LOSS OF ARCTIC SEA ICE: THE ROLE OF CONTINENTAL RUNOFF

by

Rebecca Elaine Eager

Dissertation submitted to the Faculty of the Graduate School of the
University of Maryland, College Park, in partial fulfillment
of the requirements for the degree of
Doctor of Philosophy
2022

Advisory Committee:
Professor Sumant Nigam, Co-Chair
Associate Research Professor Alfredo Ruiz-Barradas, Co-Chair
Professor Shunlin Liang, Dean's Representative
Professor Raghu Murtugudde
Professor Rachel Pinker

Dedication

For my grandparents and my parents

Acknowledgements

I would like to first acknowledge Dr. Sumant Nigam and Dr. Alfredo Ruiz-Barradas and thank them for their willingness to serve as my advisors. I learned a tremendous amount from them, both in classes and through research, about how to be a better scientist. I would like to thank them for their patience and understanding as I navigated doctoral studies part-time while working full time.

I would also like to thank Dr. Raghu Murtugudde, Dr. Rachel Pinker, and Dr. Shunlin Liang for agreeing to take the time to sit on this committee.

I would like to thank Dr. Daqing Yang for providing the Mackenzie River water temperature dataset.

To my family, my friends, and, especially these last two years, my neighbors: thank you for being there with me and for me through this journey.

Table of Contents

List of Tables

List of Figures

Chapter 1: Introduction

1.1 Motivation

In the Arctic, sea ice is of great importance as it is both a key indicator and a driver of climate change. Sea ice is highly sensitive to temperature changes of the overlying atmosphere and the underlying ocean. Sea ice impacts not only surface reflectivity (albedo) but also the ocean-atmosphere exchange of moisture, regional ocean currents, and clouds. The declining trend of Arctic sea ice, especially in late summer when seasonal ice extent is also a minimum, is widely considered a key indicator of the global warming of the planet. Several studies have also argued that the declining Arctic sea ice, in turn, is a driver of extratropical climate variability and change such as possibly contributing to a southward shift of the summer jet stream over Europe and increased summer precipitation in northern Europe (Screen 2013) and influencing the easterly zonal wind component, resulting in a more meridional flow pattern over the mid-latitudes (Overland and Wang 2010).

The Arctic Ocean, and in general the Arctic region, is a critical component of the climate system. This ocean is largely surrounded by the North America and Eurasian continents, with important links to the Pacific Ocean via the Bering Strait and to the Atlantic Ocean via the Labrador, Norwegian and Greenland Seas (Figure 1.1). The Arctic Ocean has a much wider continental shelf along the Eurasian continent than along the North American continent (Figure 1.2). The major seas surrounding the central Arctic are the Beaufort, Chukchi, East Siberian, Laptev, Kara, and Barents Seas. The main ocean currents in the Arctic region include the North Atlantic Drift, the Beaufort Gyre, and the Transpolar Drift Stream (Figure 1.1). The North Atlantic Drift brings relatively warm and saline Atlantic water into the Arctic while the Beaufort Gyre is an anticyclonic circulation in the Pacific sector. The Transpolar Drift Stream moves water from the Siberian coast, largely freshwater runoff from rivers in Russia, across the North Pole and southward to Greenland and into the North Atlantic via the Fram Strait. The Arctic Ocean contains only about 1% of the global ocean volume, but it is the most river-influenced ocean basin on the planet, receiving about 11% of the world's river outflow (McClelland et al. 2012). The major rivers that drain into the Arctic Ocean (Figure 1.2, counter-clockwise from the lower right) are: Ob, Yenisey, Lena, Kolyma, Yukon, and Mackenzie Rivers. In light of its geometry and location, the Arctic basin is sensitive to the variability and change occurring in the adjoining oceans and continents, and the overlying atmosphere, making diagnoses of regional Arctic climate variability and change challenging.

Non-seasonal sea ice variations in the Arctic reflect both natural climate variability and anthropogenic climate change. Natural climate variability at interannual-to-decadal timescales that may impact the Arctic climate includes phenomena such as the Northern Annual Mode (NAM; also called the Arctic Oscillation, AO; Thompson and Wallace 1998); its close and more widely known cousin, the North Atlantic Oscillation (NAO, Hurrell 1995); and the Pacific Decadal Oscillation (PDO, Mantua et al. 1997; Mantua and Hare 2002; also called North Pacific decadal variability, PDV-NP, Guan and Nigam 2008). These natural modes of climate variability can alter the regional patterns and intensity of storm tracks, the prevailing winds, surface air temperatures, precipitation, snow accumulation, sea ice accumulation and extent, ocean currents and associated ocean heat transport (Mysak 2001; Rigor and Wallace 2004; Polykov et al. 2005; Shimada et al. 2006), and greenhouse gas loading (Zhang and Walsh 2006).

Record-breaking loss of Arctic sea ice was observed in the past two decades (2007 and 2012; Figure 1.3). Not surprisingly, the sea ice loss was most pronounced in September – the month of minimum sea ice extent, climatologically. The recent losses were notable in the Pacific sector, extending westward from the Beaufort Sea to the Laptev Sea. A chain of events is believed to have led to the September 2007 sea ice minimum. A persistent positive phase of the NAM/AO from 1989 to 1995 caused wind patterns that flushed thick ice from the central Arctic to the Atlantic through the Fram Strait during the months of December through March, resulting in a thinner ice pack (Nghiem et al. 2007; Maslanik et al. 2007b). The atmospheric circulation pattern in September 2007 was characterized by anomalously high pressure over the central Arctic Ocean, a northward shift of the Beaufort High, and lower than normal pressure over northern Siberia caused by negative AO and positive Dipole Anomaly phases. This led to (1) positive air temperature anomalies and melting in the East Siberian and Chukchi Seas (Stroeve et al. 2008) and (2) southerly winds that enhanced transport of ice away from the Siberian and Alaskan coasts toward the North Pole, lessened ice growth, and increased ice melt (Comiso et al. 2008; Ogi and Wallace 2007; Ogi et al. 2008). Kay et al. (2008) found that the warm and dry conditions associated with the anticyclonic circulation over the central Arctic during Summer 2007 led to reduced cloudiness and enhanced downwelling shortwave radiation, which increased melt at the ice surface and heated the ocean surface layer, which indirectly enhanced the basal ice melt. These acted in conjunction with the thinner ice pack to cause the then-record low Arctic sea ice extent in September 2007 of 4.155 million km^2 (Stroeve et al. 2008).

In contrast, the September 2012 Arctic sea ice extent minimum has been attributed primarily to a strong, long-lived cyclone that moved into the Arctic in August 2012 and caused the sea ice to break up, making it more susceptible to melt (Parkinson and Comiso 2013). Prior to the August cyclone, the sea ice in the Beaufort Sea had been fragmented into floes (cohesive sheets of ice floating in the water) by strong winds over the Beaufort Gyre in June and July. This led to enhanced melting when relatively warmer river water was discharged from the Mackenzie River into the Beaufort Sea in July 2012 (Nghiem et al. 2014) and caused large sea ice concentration anomalies in the Beaufort Sea. Combined with the sharp reduction of sea ice by the August cyclone further to the west, September 2012 holds the current record for daily minimum September sea ice extent at 3.387 million km^2 (Figure 1.3); it is evident that in no year since 2007 has the September monthly mean sea ice extent rebounded to pre-2007 levels. The September 2020 average sea ice extent of 4.0 million km^2 was only the second lowest in the 42-year satellite record.

That several extreme Arctic sea ice loss years are clustered in the past 14 years raises the question of whether we are presently in a phase of multidecadal natural variability in which Arctic sea ice extent/thickness is below normal. Day et al. (2012) and Miles et al. (2014) noted Atlantic multidecadal variability in Arctic total sea ice extent. Yu et al. (2017) found that global (Arctic and Antarctic) seasonal sea ice concentration time series is positively correlated to the Atlantic Multidecadal Oscillation (AMO, Enfield et al. 2001; Guan and Nigam 2009) index and negatively correlated to the Pacific Decadal Oscillation (PDO, Mantua et al. 1997; Mantua and Hare 2002) index. Ice export through the Fram Strait appears to also be linked to multidecadal natural variability (Smedsrud et al. 2017). The AMO seems to play an important role in Arctic climate variability in view of its strong footprint on North Atlantic sea surface temperature (SST) and surface/subsurface salinity (Kavvada et al. 2013), on the hydroclimate of the adjoining continents (Nigam et al. 2011), and on winter/spring sea ice conditions in the preinstrumental record (Miles et al. 2014). Seasonal anomalies of ocean heat content during 1996 and 2007 (high and low ice years, respectively) exhibited a pattern reminiscent of the AMO impact (Kavvada et al. 2013), further spurring interest in this mode of climate variability. However, anthropogenic warming and the related long-term declining trend in Arctic sea ice extent in the recent past is another possibility.

It should be noted that the terminology surrounding the AMO and the mechanism(s) generating the AMO are actively being debated in the literature. The AMO (Kerr 2000) index is traditionally defined as the 10-year running mean of linearly detrended SST anomalies averaged over the entire North Atlantic (Enfield et al. 2001) and has a cycle of about 65-80 years. Alternatively, this variability in North Atlantic SST is also referred to as Atlantic Multidecadal Variability (AMV), to recognize that the observed multidecadal fluctuations in the Atlantic may consist of a broader range of low-frequency signals and to de-emphasize the notion of it being an oscillation at a single frequency (Zhang et al. 2019; Sutton et al. 2018; Zhang 2017).

The recent review article by Zhang et al. (2019) synthesizes paleoproxy, modern observations, and climate simulations to investigate the linkage between the AMOC and AMV. They also discuss each proposed mechanism for observed AMV, including whether or not it is consistent with key elements of observed AMV. Proposed mechanisms for the observed AMO/AMV have included the Atlantic Meridional Overturning Circulation (AMOC; Oelsmann et al. 2020; Zhang et al. 2019); a direct red noise response of the North Atlantic SST to stochastic atmospheric-induced surface heat flux forcing (Clement et al. 2015); and external radiative forcing due to anthropogenic aerosols, solar variations, and/or volcanic eruptions (Bellomo et al. 2018; Bellucci et al. 2017; Booth et al. 2012; Dunstone et al. 2013; Mann & Emanuel 2006; Murphy et al. 2017; Otterå et al. 2010; Zanchettin et al. 2013). Another possibility suggested is that an oscillatory internally-forced signal exists but has been misidentified due to statistical procedures that do not properly account for the forced component (Mann et al. 2020; Mann et al. 2014; Mann & Emanuel 2006; Frankcombe et al. 2015; Frankcombe al. 2018).

Zhang et al. (2019) found the observational and modeling results to be consistent with a central role for multidecadal AMOC variability in AMV. Multidecadal changes in the AMOC and associated heat transport across midlatitudes (inferred from sea level anomalies at U.S. east coast gauge stations) have been found to be strongly linked to the observed AMV (McCarthy et al. 2015). Several studies have found anomalous Atlantic meridional heat transport induced by multidecadal

AMOC variability plays an important role in the linkage with AMV (e.g., Danabasoglu et al. 2012; Knight et al. 2005; Wills et al. 2019; Zhang & Zhang, 2015). Additionally, multidecadal AMOC variability as a key driver for observed AMV is consistent with all six observed key elements of AMV (Zhang et al. 2019).

The large-scale stochastic atmosphere-induced surface heat flux forcing mechanism has been proposed because the North Atlantic SST patterns associated with the AMV and the North Atlantic SST spectra are similar in CGCMs with ocean dynamics and in slab ocean models without ocean dynamics (Clement et al. 2015). However, as described in Zhang et al. (2019), unlike slab ocean models, multidecadal net downward surface heat flux anomalies in CGCMs are not a forcing for AMV but instead have a negative correlation/regression with AMV. In addition, they argue this mechanism does not explain the Atlantic dipole SST pattern, the observed anticorrelation between multidecadal tropical North Atlantic surface and subsurface temperature variations, the high coherence among observed subpolar North Atlantic SST, SSS, upper ocean heat and salt content at multidecadal (but not interannual) timescales, and decadal persistence of the observed subpolar North Atlantic SST and SSS variations.

The external radiative forcings mechanism, specifically due to anthropogenic aerosols, has been hypothesized because, in twentieth-century externally-forced coupled general circulation models (CGCM), an increase in the linearly detrended AMV SST index is found to be forced by the increased downward shortwave radiative heat flux induced by the decreased anthropogenic aerosols through their interaction with clouds (Booth et al. 2012). However, the aerosol-forcing mechanism is not supported by many of the observed key elements of AMV, including the observed Atlantic dipole SST pattern and the observed anticorrelation between multidecadal tropical North Atlantic surface and subsurface temperature variations (Zhang et al. 2019).

Recent papers by Mann et al. (2020) and Mann et al. (2021) investigate the influence of external radiative forcing through a comparison of the CMIP5 multimodel Last Millennium simulation ensemble (driven with estimated natural forcing over the preindustrial period: volcanic, solar, astronomical, greenhouse gas, land-use change) and the CMIP5 control simulations (no forced variability). In the control simulations, they found no ensemble-wide evidence for a multidecadal spectral peak (Mann et al. 2020). In the Last Millennium simulation ensemble, they estimated the forced-only component of temperature variation by averaging over the ensemble and found statistically significant spectral peaks that correspond to the ~20 to 30-year interdecadal range and the ~50 to 70-year multidecadal range (Mann et al. 2021). They conclude that the origin of the spectral peaks identified in the analysis of the Last Millennium simulations is due to the long-term changes in radiative forcing, primarily due to volcanic eruptions. Their overall conclusion is that the collective available evidence from observations climate model simulations point toward externally-forced multidecadal oscillations due to anthropogenic forcings during the historical period and the coincidental multidecadal pacing of tropical volcanic eruptions in past centuries, and that there is no compelling evidence for a purely internal multidecadal AMO/AMV cycle (Mann et al. 2021).

As summarized by Zhang et al. (2019), understanding the linkage between the AMOC and AMV is challenging due substantial biases most climate models have in simulating a realistic AMOC structure and associated Atlantic meridional heat transport and the limited observational record duration (about 100-150 years). The new CMIP6 model simulations provide an updated opportunity to explore and understand the mechanism(s) leading to AMV.

The focus of this introductory chapter is on describing the climatology of the Arctic and presenting background information that will be leveraged throughout the later chapters. Section 1.2 describes the data sets used throughout this dissertation. Section 1.3 presents the atmospheric and oceanic climatology of the Arctic, while Section 1.4 introduces the Arctic freshwater system. Section 1.5 provides more details about the rivers in the Arctic. Section 1.6 discusses the objective of this dissertation, and Section 1.7 describes the structure of the remaining chapters.

1.2 Data Sets

1.2.1 Atmospheric Reanalysis and Ocean Analysis

Atmospheric reanalysis data from two sources were used to investigate the climatology of the Arctic atmosphere. NCEP-NCAR reanalysis data, available from 1949 to 2016 at 2.5° spatial resolution, were used to study the climatological atmospheric circulation in the lower atmosphere from the surface to 850 hPa (Kalnay et al. 1996). The NCEP-NCAR data were downloaded from the Columbia Data Library website (http://iridl.ldeo.columbia.edu/SOURCES/.NOAA/.NCEP-

NCAR/.CDAS-1/.MONTHLY/) on 23 February 2016. Data from the Era-Interim reanalysis (1979-2015) was used to study the climatological cloud cover and radiation fields of the Arctic (Dee et al. 2011; ECMWF 2012). The total cloud cover fields were available at 0.75° x 0.75° spatial resolution. Downward shortwave radiation and downward longwave radiation at the surface were downloaded on 19 June 2016; these data were available on grids of 0.703° x ~0.702° for the 1979-2012 time period.

Data to study the ocean climatology comes from the UK Meteorological Office Hadley Centre's EN version 4.2.1, downloaded on 18 October 2018 (Good et al. 2013). EN4.2.1 is a quality-controlled objective analysis of the subsurface ocean data including sea water salinity and ocean temperature which have been bias corrected with Levitus WOA09 data (Levitus et al. 2009a). Ocean heat content (OHC) has been computed from the ocean temperature profiles as the vertically-integrated heat content in an ocean column extending from the ocean surface to particular depths.

Monthly near-surface gridded temperatures over land from 1901-2016 are available from the Climate Research Unit time series (CRU TS) dataset at 0.5° spatial resolution (Harris et al. 2020). The version 4.01 data set (University of East Anglia Climate Research Unit et al. 2017) was used to estimate river temperatures for the North American rivers, which had limited river temperature measurements as compared to the available river temperature measurements from the Eurasian rivers. Once the version 4.02 data set (University of East Anglia Climate Research Unit et al. 2019) became available, it was used in later analyses to support greater understanding of the continental temperature and hydrology of the Arctic region.

1.2.2 Sea Ice Concentration

Monthly mean sea ice concentration (SIC) fields from the Hadley Centre's Sea Ice and Sea Surface Temperature data set (HadISST2.2) version 2.2.0.0 is available globally for 1850 to present at 1° spatial resolution (Titchner and Rayner 2014). The data was downloaded from the UK Met Office Hadley Center observation datasets website (metoffice.gov.uk/hadobs/hadisst2/) on 5 March 2018. The primary source for SIC from 1979 onwards is passive microwave satellite sensor data from the Scanning Multichannel Microwave Radiometer (SMMR) until August 1987 and from the Special Sensor Microwave/Imager (SSM/I) and Special Sensor Microwave Imager/Sounder (SSMI/S) starting in July 1987. Prior to 1979, HadISST2 uses sea ice charts and a compilation of sea ice charts and reports from Walsh and Chapman (Walsh 1978; Walsh and Johnson 1978; Chapman and Walsh 1991; Walsh and Chapman 2001).

A second SIC data set, the Gridded Monthly Sea Ice Extent and Concentration, 1850 Onward (SIBT1850), provides quarter-degree resolution for the SIC and sea ice extent (SIE) fields from 1850 to 2013 (Walsh et al. 2015). This additional dataset was used to investigate the robustness of the analysis results from the HadISST2.2 data set. The monthly SIC fields in SIBT1850 represent snapshots of the SIC on the 15th day of each month, in contrast to the monthly mean SIC fields in HadISST2.2. Like HadISST2.2, the source of SIC data from 1979 onwards is passive microwave satellite data. Prior to 1979, sources for SIC include ship reports, airplane surveys, and analyses by national ice services (Walsh et al. 2017). The description of the development of the SIBT1850 data set is described in Walsh et al. (2017), and summarized here. For data sources that reported the location of the ice-edge, the sea ice concentration was estimated from a series of gradients derived from pre-existing monthly fields for 1953-2002, taking into account seasonal and regional variability. For time periods and locations without data, linear temporal interpolation was used if there was SIC data in the previous and subsequent months, and otherwise an analog procedure was used to fill in the missing data.

1.2.3 Precipitation and Evapotranspiration

The Global Precipitation Climatology Centre (GPCC) Full Data Monthly Version 2018 (v8; Schneider et al. 2018) is available from 1891 to 2016. The GPCC precipitation data set is based on quality-controlled data from 67,200 stations that had records of 10 years or longer and is optimized for use in water budget studies. Accumulated monthly precipitation is available at resolutions of 0.25°, 0.5°, 1°, and 2.5°; the 0.25°-resolution data is used in this research, to coincide with the time period of the other precipitation data set. This data set was downloaded on 14 February 2020 from the Columbia Data Library website (https://iridl.ldeo.columbia.edu/SOURCES/.WCRP/.GCOS/.GPCC/.FDP/.version2018/). The accumulated monthly precipitation was converted from mm to monthly average precipitation, with units of mm day^{-1}. The mean seasonal precipitation was calculated as the average over each season, where winter is December-February, spring is March-May, summer is June-August, and autumn is September-November.

The Terrestrial Precipitation Version 5.01 data set (UDEL; Matsuura and Willmott 2018a, downloaded on 12 November 2018), available from the Department of Geography at the University of Delaware, consists of monthly-total rain gauge-measured precipitation from 1900 to 2017. UDEL is compiled from a variety of sources including the Global Historical Climatology Network dataset, a version of the Daily Global Historical Climatology Network (Menne et al. 2012), and archives and station data from Canada, Russia, Greenland, India, Africa, and South America. The station values of monthly total rain gauge-measured precipitation were interpolated to a 0.5° x 0.5° grid and climatologically-aided interpolation (Willmott and Robeson 1995) was used to estimate the monthly total precipitation fields. The number of stations used in each month ranged from 7,500 to 40,500. Precipitation data in this data set have not been adjusted to account for bias due to rain gauge undercatch.

In addition to the Terrestrial Precipitation data set, the Monthly Terrestrial Water Budget Time Series Version 4.01 is also available for 1900-2017 (Matsuura and Willmott 2018b, downloaded on 12 November 2018). Using a modified version of the Thornthwaite water-budget procedure (Willmott et al. 1985), the monthly water budget fields were estimated from the gridded monthly-average temperature and monthly-total precipitation fields using semi-empirical relationships between observed monthly total precipitation and estimated monthly potential evapotranspiration and assuming the soil water-holding capacity was constant at 150 mm. The calculations were performed for each grid node. Available water budget fields include the following: monthly potential evapotranspiration, monthly actual evapotranspiration, monthly deficit (potential minus actual evapotranspiration), mid-monthly soil-moisture depth, mid-monthly water equivalent of the snow pack, monthly snow melt, and monthly surplus.

1.2.4 River Discharge and Runoff

As described by the United States Geological Survey (USGS), river discharge is the volume of water moving down a stream or river per unit of time, and in general is computed by multiplying the area of water in a channel cross-section by the average velocity of the water in that cross-section. River discharge stations of interest in this study are maintained by the Federal Service for Hydrometeorology and Environmental Monitoring in Russia (Roshydromet), the Water Survey of Canada (WSC), and the USGS. Measurements are available starting in the 1930s for the Ob, Yenisey, and Lena Rivers, and starting in the 1970s for the Kolyma, Yukon, and Mackenzie Rivers. The number of discharge monitoring sites in Russia increased from the 1930s to about 1980, while the number of stations in North America did not start increasing until the 1950s. The number of monitoring sites has decreased from the 1980s to 2000 and has remained fairly constant since then (McClelland et al. 2015). Arctic river discharge data sets used in this study were from R-ArcticNET version 4 and the Arctic Great Rivers Observatory (ArcticGRO). The periods of data availability from the two sources are provided in Table 1.1.

The Regional, Electronic, Hydrographic Data Network for the Arctic region, R-ArcticNET (http://www.r-arcticnet.sr.unh.edu/v4.0/index.html), is an internet-based regional hydrometeorological databank to support pan-Arctic hydrological sciences and water resource assessment in the Arctic (Lammers et al. 2001). It compiled monthly mean river discharge data from more than 3,700 gauges throughout the pan-Arctic drainage system from multiple sources in North America, Europe, and Asia. For the six major Arctic rivers, data extend through 1999 or 2000, depending on the river.

The Arctic Great Rivers Observatory (ArcticGRO; https://arcticgreatrivers.org/) maintains a database of daily river discharge measurements beginning in 1999 and continuing to the present for the major Arctic rivers (Shiklomanov et al. 2018). Versions of the discharge data from ArcticGRO are named by date; the 31 December 2019 data set was used in this study for the river discharge data. Data certified by the national hydrological institutions and provisional data are included in the updated record, with provisional data flagged.

As described in the ArcticGRO metadata, discharge data from the Kolyma River are provided for two proximate sites because data are not available from a single collection site for the full time period. Station information for the two gauging stations on the Kolyma River indicate they are located at the same latitude and longitude and the total basin drainage area is the same for both stations. Data from the two stations do not overlap in time, with one station operating until 2008 and the other starting in 2009. In the research presented here, the discharge measurements for the two gauge stations on the Kolyma River are considered as one time series.

The GRUN data set is a global gridded monthly reconstruction of runoff for 1902 to 2014 (Ghiggi et al. 2019). Runoff was reconstructed by training a machine learning algorithm using streamflow observations to predict monthly runoff based on precipitation and temperature from an atmospheric reanalysis. GRUN data are available on a 0.5° latitude-longitude grid. The runoff data were regridded to a 0.25° latitude-longitude grid to match the GPCC data.

1.2.5 River Water Temperature

River water temperatures are available from three sources. The ART-Russia river temperature study (Lammers et al. 2007a) consists of 10-day mean river water temperatures from 1929 to 2003. Most of the data is from the mid-1930s to the early 1990s. The water temperature measurements and river discharge measurements were used to calculate the energy flux (Lammers et al. 2007b). The ART-Russia stations were co-located with the river discharge stations. A data set containing river temperature data for the Mackenzie River from 1960 to 2010 was provided by Dr. Daqing Yang of Environment Canada; this will be referred to as the Yang data set. ArcticGRO also provides a water quality data set that includes river temperatures and was collected during several sampling efforts: Pan-Arctic River Transport of Nutrients, Organic Matter, and Suspended Sediments (PARTNERS) Project (2003-2007) and the Arctic Great Rivers Observatory Project, which has three phases thus far: ArcticGRO I (2009-2011), ArcticGRO II (2012-2016) and ArcticGRO III (2017-2020). River temperature data contained in the ArcticGRO Water Quality Data version 12 June 2018 was used (Holmes et al. 2018).

For the Mackenzie River, river temperature measurements from the Yang data set and the ArcticGRO data sets were taken at different locations, the distance between the two measurement locations is 2.6 km, and thus there is anticipated to be little to no difference in river temperature. ArcticGRO temperature measurements for the Lena River are from Zhigansk, which is located about 460 km south of Kusur. For the Yenisey River, the ArcticGRO measurement site at Dudinka is about 220 km north of Igarka. For the Kolyma River, the ArcticGRO measurement site at Cherskiy is about 100 km to the northeast of Kolymskoye. The river station locations for water temperature are listed in Table 1.2.

1.3 Climatology

The seasonal average SIC for the 1958 to 2013 time period is shown in Figure 1.4. While sea ice data exist back to 1850, the focus of the research presented in this dissertation is on the post-International Geophysical Year (IGY) period, from 1958 to 2013. Seasonal SIC fields were generated by computing the mean over their usual 3-month Northern Hemisphere season: winter (December to February), spring (March to May), summer (June to August) and fall (September to November). The Arctic Ocean is ice covered in the winter and spring. Melting of the sea ice begins along the coasts in summer; starting in June near the mouths of the Ob, Yenisey, Lena, and Mackenzie Rivers and then evident along the coasts throughout the Arctic in July. The retreat of ice becomes more pronounced by August and reaches a maximum (i.e., minimum ice extent) in September. Ice is preferentially lost along the coastlines in the marginal ice zone, beginning with the regions near the Bering Strait inflow and near river mouths, rather than being uniformly distributed over the Arctic; ice loss is also not zonally uniform – higher concentrations of sea ice remain at lower latitudes on the North American side than the Eurasian side in September. The sea ice retreat in the Chukchi and Kara Seas is the most striking with an annual 15° latitude retreat of the sea ice edge.

To try to understand these regional differences, we started with the climatology of the Arctic, for both the atmosphere and ocean. Incoming solar radiation is limited to late March through late September, during the long polar summer days; however, the ubiquitous cloud cover limits the amount of solar radiation that reaches the surface while at the same time increasing the thermal radiation to the surface. The polar ocean mixed layer also undergoes seasonal changes due to heat exchange with the atmosphere and inflow into the basin, which are reflected in the ocean heat content (OHC) and salinity. This layer, which is in contact with the overlying sea ice, can influence the basal ice melt. Atmospheric circulation patterns and ocean currents transport ice within the Arctic, eventually flushing ice into the North Atlantic. These will be discussed in more detail in the following sections.

1.3.1 Atmospheric Climatology

The primary atmospheric circulation features in the high latitudes are the Beaufort, Siberian, and North American Highs and the Icelandic and Aleutian Lows. The seasonal climatological mean sea level pressure for 1979-2015 is shown in Figure 1.5. During winter, the ice-covered Arctic Ocean acts as a continent and high pressure at low levels extends from northeastern Eurasia to north-central Canada, spanning the Chukchi and Beaufort Seas. The Icelandic and Aleutian lows are strongest in winter, with the North Atlantic storm track extending into the Norwegian and Barents Seas, as evidenced in the region of low pressure stretching from the tip of Greenland to the northeast. In the spring, the North Atlantic storm track, Icelandic Low, and Aleutian Low all weaken and the Siberian High retreats. The Beaufort High becomes more pronounced and is centered over the Beaufort Sea. The mean sea level pressure in the Beaufort High reaches a peak of 1020 hPa in March (Serreze and Barrett 2011). The Beaufort High drives the anticyclonic Beaufort Gyre. Ekman transport causes ice to move toward the center of the gyre (i.e., to the right) and away from the Alaskan coast; even during seasons with high ice concentrations, the sea ice is not static. Mean sea level pressure is fairly uniform across the Arctic in summer, with the Beaufort High shrinking in size and strength and shifting nearer the Alaskan coast (Serreze and Barrett 2011). The Beaufort High reappears in autumn as an extension of the Siberian High. The Beaufort High is a surface-based feature and while it is marginally evident in spring at 925 hPa and as a break in broad low geopotential heights across the Arctic in other seasons, it is not well-defined at 850 hPa.

The climatological total cloud cover is shown in Figure 1.6. During the winter, stratus clouds form due to radiational cooling and the cold air remains trapped under a surface-based inversion. During the polar night, there is insufficient vertical mixing to erode the inversion and the clouds remain. Cloud cover is highest along the coasts during the winter, reflecting an increased presence of water vapor, in contrast to the frozen and dry central Arctic. Low-level stratus peaks in the summer months over the central Arctic as both local and remote sources of water vapor are more available. The relatively warm, moist air advected into the Arctic condenses due to radiative and diffusive cooling to the colder surface and longwave emission to space (Herman and Goody 1976) and forms a radiation fog layer. The fog layer deepens into a stratus layer due to radiative cooling and turbulent mixing at the top of the layer. Because the sun remains at a constant, very low position in the sky and the underlying ice surface maintains a uniform temperature, the stratus cloud never dissolves. Middle and upper-level clouds form due to the presence of frontal systems

(Curry and Herman 1985) with a maximum (minimum) in the winter (summer) months corresponding to the maximum (minimum) in cyclone frequency (Curry et al. 1996). In the marginal ice zone, clouds are frequently associated with frontal systems and may be convective, especially in autumn when baroclinic effects are the strongest (Curry et al. 1990).

The total downward surface solar plus thermal radiation is shown in Figure 1.7 and the sum of the seasonal departures of the downward surface solar radiation and downward surface thermal radiation from the respective annual means is shown in Figure 1.8. During most of the autumn and winter (late September to late March), downward radiation is limited to longwave radiation from clouds and water vapor in the atmosphere. The sun is below the horizon most of the time, resulting in little to no incoming solar radiation. The zonal asymmetry in the winter total downward surface radiation field is caused by the North Atlantic storm track, which brings storms and their associated cloudiness, increasing the downward longwave radiation to the surface into the Barents Sea. Solar radiation increases in the spring and peaks in summer as the sun comes over the horizon. Downward thermal radiation also increases in spring and summer as cloud cover and re-radiation to the surface increases. Both downward surface solar and thermal radiation decrease in the autumn. It should be noted that, throughout the year, upward thermal radiation exceeds downward thermal radiation in the Arctic.

The near-surface air temperature over land in the northern part of the Northern Hemisphere is shown in Figure 1.9. This figure also shows the outlines of the six major river basins in the Arctic (refer to Figure 1.2 for identification of the river basins). As with solar radiation, temperatures in the Arctic exhibit a strong seasonal cycle. In the Siberian Arctic, temperatures in the winter range from -15°C to -40°C, and are about -10°C to -20°C in northwest North America. During in the summer, temperatures are 5°C to 15°C in the Siberian Arctic and about 10°C in northwest North America. In the spring and autumn, freezing temperature persist in eastern Siberian, while they reach -5°C to 5°C in western Siberia and northwest North America.

The precipitation over the land in the northern part of the Northern Hemisphere is shown in Figure 1.10, along with the river basin outlines. Precipitation exhibits strong seasonality in the vicinity of the river basins with the bulk of the precipitation occurring during the summer with values up to about 3 mm day^{-1}, and tapering off in the autumn. In the winter and spring, there is about 1 mm day^{-1} or less of precipitation. Outside of the river basins, there are high amounts of precipitation throughout the year along the Pacific coast of Alaska due to orographic forcing. Eastern North America and Western Europe also experience higher levels of precipitation throughout the year.

1.3.2 Oceanic Climatology

The Arctic Ocean can be divided into four major layers, starting at the surface and increasing in depth: the polar mixed layer, the halocline, Atlantic Water, and Arctic Deep Water. The polar mixed layer contains cold, low saline freshwater from Pacific water inflow, river runoff, sea ice melt, and net precipitation. This freshwater plays an important role by maintaining the stratification of the Arctic Ocean, which restricts mixing between the surface and deeper ocean layers and insulates the sea ice from the heat stored in the relatively warmer Atlantic waters below. The layer of Atlantic Water is typically found at depths of about 400-1000 m in the western Arctic and 100-1000 m in the eastern Arctic. Freshwater is also important to sea ice formation as sea ice is able to form more easily in less saline waters. Ocean heat content and salinity of the uppermost layer of the ocean, both climatologies and departures from climatology, are thus important to the overlying sea ice, as this is the layer in contact with the ice.

The seasonal climatology of the ocean heat content (OHC) in the uppermost 25 m is shown in Figure 1.11. This figure shows the integrated heat content for the top 25 m of the ocean. Warm water entering the Arctic, specifically entering the Barents Sea, due to the North Atlantic Drift is evident in all seasons. Warm Pacific waters can also be seen entering the Arctic through the Bering Strait. Seasonal departures of OHC from the annual mean are shown for all four seasons in Figure 1.12. The area with the most pronounced departure of OHC from the annual mean stretches from Greenland into the Barents Sea. During the winter, strong flow around the Icelandic Low causes mechanical mixing of the ocean mixed layer, resulting in strong upward latent and sensible heat fluxes that cool the upper ocean. In the summer, the upper-ocean warms by absorbing heat from both downward thermal emission from clouds (this region is about 80% cloud covered) and incoming solar radiation during the long polar summer days. The winds are also weaker in summer, which reduces the mixing and further stabilizes the water column. During winter and spring (summer and autumn), the OHC along the Alaskan coast is less (greater) than the annual mean. Warm inflow across the Bering Strait is seen in summer, along with a region of warmer waters just west of the Canadian Arctic Archipelago. In contrast, the Kara Sea and Baffin Bay are warmer than the annual mean in winter and cooler than the annual mean in summer and autumn. In the Kara Sea, this warm water comes from the North Atlantic Drift, which brings warm, salty water (apparent from the next figure) into the region which cools and sinks as it enters the Norwegian and Greenland Seas. In the winter, southerly winds on the eastern edge of the Icelandic Low push water away from the coast and cause upwelling of the warm water.

The salinity in the surface layer, i.e., the layer adjacent to the overlying ice cover, is also of interest. The highest salinity waters in the Arctic (34-35) are found in the Norwegian, Greenland, and Barents Seas due to salty waters from the North Atlantic and from salt rejection during ice formation (Figure 1.13). Salinity is much lower along the Russian and North American coasts, particularly at river mouths where freshwater is released into the Arctic. Seasonal anomalies of near-surface (5 m depth) salinity are shown in Figure 1.14. Most prominent in the summer, but evident at some river mouths starting in the spring, the freshwater from Arctic rivers reduces the salinity by as much as 3.5 from the annual mean in the Beaufort, East Siberian, and Kara Seas.

<u>1.4 Introduction to the Arctic Freshwater System</u>

The Arctic freshwater system has been the focus of major international scientific programs over the past twenty-five years, beginning with the Arctic Climate System Study (ACSYS) in 1994. Programs since then include a NATO Advanced Research Workshop called “The Freshwater Budget of the Arctic Ocean” (FWBAO), Arctic-HYDRA (Hydrological Cycle Monitoring, Modelling, and Assessment

Program), the pan-Arctic Community-wide Hydrological Analysis and Monitoring Program (Arctic-CHAMP), Freshwater Integration study (FWI), and most recently the Arctic Freshwater Synthesis (Prowse et al. 2015). The focus of these projects has included determining the Arctic freshwater budget, assessing the variability of freshwater input to the Arctic Ocean, and understanding how the Arctic freshwater hydrologic system could be altered by changes in climate.

An early version of the freshwater budget in the Arctic Ocean was assembled by Aagaard and Carmack (1989). They calculated sources and sinks of freshwater independently, without trying to balance the budget due to the uncertainties in each of the various terms of the budget. Sources of freshwater to the Arctic Ocean include river runoff, net precipitation (precipitation minus evapotranspiration), liquid freshwater entering through the Bering Strait, and liquid freshwater entering with the Norwegian Coastal Current. Freshwater sinks include export of liquid water through the Canadian Arctic Archipelago, ice and liquid export through Fram Strait, saline water import through Barents Sea, and saline water import with the West Spitsbergen Current. Additional sources and sinks that Aagaard and Carmack (1989) omitted, due to their negligible size relative to the other sources, include import of ice through Bering Strait, export of ice through the Canadian Arctic Archipelago, and export of freshwater south of Spitsbergen. Additionally, sea ice melt also provides a source of freshwater to the Arctic Ocean. The inventory of freshwater in the central Arctic Ocean has increased during the period starting in the first half of the 1990s through 2005 (Jones et al. 2008; Newton et al. 2013).

1.5 Arctic Rivers

The Arctic Ocean freshwater budget constructed by Serreze et al. (2006), to build on that done by Aagaard and Carmack (1989), found that 38% of the annual mean freshwater input into the Arctic Ocean is from river discharge. Total river runoff entering the Arctic was estimated by Aagaard and Carmack (1989) to be about 3,300 km^3 $year^{-1}$, or about 35 cm $year^{-1}$, based on a value by Treshnikov (1985). Haine et al. (2015) updated the value of the runoff from rivers, streams, and groundwater to the Arctic, Canadian Arctic Archipelago, and Baffin Bay, based on the 1980-2000 period, to be 3,900 ± 390 km^3 $year^{-1}$. Haine et al. (2015) calculated that number as the average of the runoff from the ERA-Interim reanalysis product (4,200 km^3 $year^{-1}$) and from river discharge observations that were extrapolated to fill data gaps (3,600 km^3 $year^{-1}$).

Six major rivers, and many smaller ones, flow northward from North America, Europe, and Asia, emptying into the seas surrounding the Arctic Ocean. The major rivers are the Ob, Yenisey, Lena, and Kolyma Rivers in Russia and the Mackenzie and Yukon Rivers in North America (Figure 1.2). River discharge measurements from gauge stations located nearest the mouth of each river is used to quantify the discharge exiting each river. Monitoring stations for the six major rivers capture discharge for about 53% of the pan-Arctic watershed (McClelland et al. 2015). The locations of these rivers, the basins that supply the water for those rivers, and the basin topography are shown in Figure 1.2. Details about the size of each basin's watershed, total annual discharge, and gauge station location are provided in Table 1.1. All rivers experience low-level streamflow and low discharge during winter months. The streamflow increases in the spring as snow melts and discharge increases as the river ice melts. Peak river discharge occurs in all six rivers in June and then tapers off through the summer and fall.

1.6 Research Objectives

As noted in Section 1.1, several studies have discussed the potential influence of Atlantic multidecadal variability or the AMO on sea ice in the Arctic (Day et al. 2012; Miles et al. 2014; Yu et al. 2017). The mechanism linking the AMO and sea ice, however, was not uncovered in these previous studies. The AMO is known to have a strong footprint on the hydroclimate of the adjoining continents (Nigam et al. 2011). The strong seasonal anomalies of salinity and OHC, particularly in the vicinity of the Arctic river mouths led to the following hypothesis: multidecadal and regional variations in Arctic SIC can be attributed in part to the AMO through modifications to the temperature and quantity of freshwater river inflow into the Arctic. Following this line of reasoning, during the warm phase AMO, warmer river water speeds basal ice melt while the fresh, warm water acts to stabilize the ocean surface layer. As ice melts, additional freshwater is added to the ocean, leading to further stabilization. The ice free ocean can also now be heated more easily by downward solar and thermal radiation. While sea ice melt occurs annually, the warm phase of the AMO accentuates the ice loss in particular regions of the Arctic.

To further test this hypothesis, the influence of decadal and multidecadal climate variability on Arctic sea ice concentration is investigated from analysis of observed data. This research is interested in identifying the contributions of the low-frequency modes on the observed summer ice trends, and establishing the extent of the continental pathway linking sea ice variability with variability in the regional hydroclimate and river streamflow variability. In this research, the low-frequency variability modes were obtained from the spatiotemporal analysis of 118 years of observed SST data from Nigam et al. (2020) that allowed the objective identification of modes of Pacific decadal variability (PDV), having footprints in the midlatitudes of the North Pacific (PDV-NP) and footprints in the Pan-Pacific domain (PDV-PP), as well as the identification of modes in the Atlantic Ocean, such as the AMO, a Low-frequency NAO mode (LF-NAO), and a Sub-Arctic decadal variability (SADV) mode. This research perspective, based on SST-based modes of decadal-to-multidecadal climate variability, is new in sea ice research, which has typically focused on analyzing the influence of interannual variability modes of atmospheric origin.

1.7 Dissertation Structure

The remaining chapters of this dissertation present the analyses and results as follows: Chapter 2 presents the influence of decadal and multidecadal climate variability on Arctic sea ice, while Chapter 3 discusses the impact of decadal and multidecadal climate variability on the Arctic atmosphere, ocean, and continental hydrology. Chapter 4 provides a summary and the overall conclusions.

Table 1.1. List of river discharge gauge stations including their location, distance from the mouth of the river, and the data availability. The mean annual discharge is for the 1999-2008 period (2001-2008 for Yukon) from Holmes et al. (2019) and assumes the unmonitored portion of the watershed has the same amount of runoff as the monitored part of the watershed.

River	**Gauge Station (distance from mouth, km)**	**Gauge Station Location**	**Outlet Location**	**R-ArcticNET discharge (monthly)**	**Arctic GRO**	**Watershed (million km^2)[1]**		**Mean annual discharge (km^3 year^{-1})[1]**	
						Upstream of Gauge Station	**Total**	**Upstream of Gauge Station**	**Total**
Ob	Salekhard (137)[2]	66.63N, 66.0E	Kara Sea	01/1930-12/1999	01/1999-12/2019	2.99	2.99	427	427
Yenisey	Igarka (687)[2]	67.43N, 86.48E	Kara Sea	01/1936-12/1999	01/1999-12/2019	2.40	2.54	636	673
Lena	Kusur (211)[2]	70.68N, 127.39E	Laptev Sea	11/1934-12/2000	01/1999-12/2019	2.43	2.46	581	588
Kolyma	Kolymskoye (212)	68.73N, 158.72E	East Siberian Sea	01/1978-12/2000	03/2009-12/2019	0.53	0.65	111	136
	Kolymsk-1 (212)			01/1977-12/1985	01/1999-12/2008				
Yukon	Pilot Station (225)	61.93N, 162.88W	Bering Sea	01/1975-12/2003	04/2001-10/2019	0.83	0.83	208	208
Mackenzie	Arctic Red River (292)	67.45N, 133.74W	Beaufort Sea	01/1972-12/2000, monthly	01/1999-12/2019	1.68	1.78	298	316

[1] Holmes et al. 2012

[2] Shiklomanov and Lammers 2014

Table 1.2. Location of river water temperature measurement sites.

River	Water Temperature Station	Location (latitude, longitude)	ArcticGRO temperature (daily)	ART 10-day mean temperature	Yang
Ob	Salekhard (GRO, ART)	66.63N, 66.60E	07/2003-01/2018	05/1936-10/1998	N/A
Yenisey	Dudinka (GRO)	69.383N, 86.15E	07/2003-01/2018	N/A	N/A
	Igarka (ART)	67.43N, 86.48E	N/A	06/1936-10/2001	N/A
Lena	Zhigansk (GRO)	66.767N, 123.367E	08/2003-03/2018	N/A	N/A
	Kusur (ART)	70.68N, 127.39E	N/A	06/1936-12/2001	N/A
Kolyma	Cherskiy (GRO)	68.75N, 161.3E	08/2003-12/2017	N/A	N/A
	Kolymskoye (ART)	68.73N, 158.72E	N/A	06/1965-10/2001	N/A
Yukon	Pilot Station (GRO)	61.93N, 162.87W	06/2003-1/2018	N/A	N/A
Mackenzie	Tsiigehthic (GRO)	67.43N, 133.75W	06/2003-02/2018	N/A	06/1960-06/2010

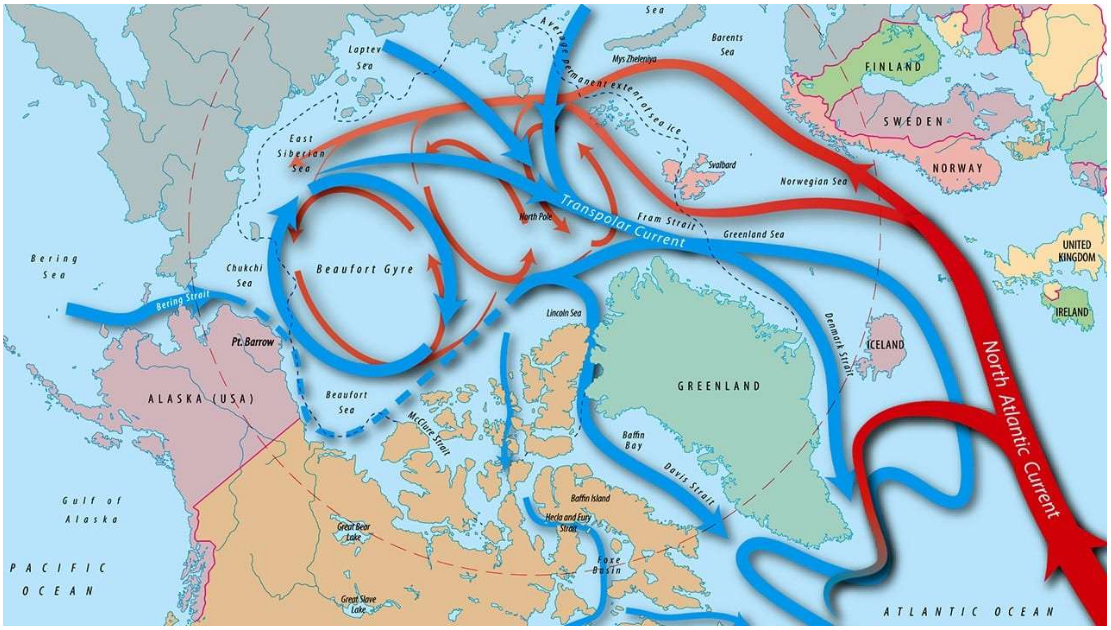

Figure 1.1. Map of the Arctic including ocean currents and locations of the seas that surround the central Arctic. © Woods Hole Oceanographic Institution, J. Cook.

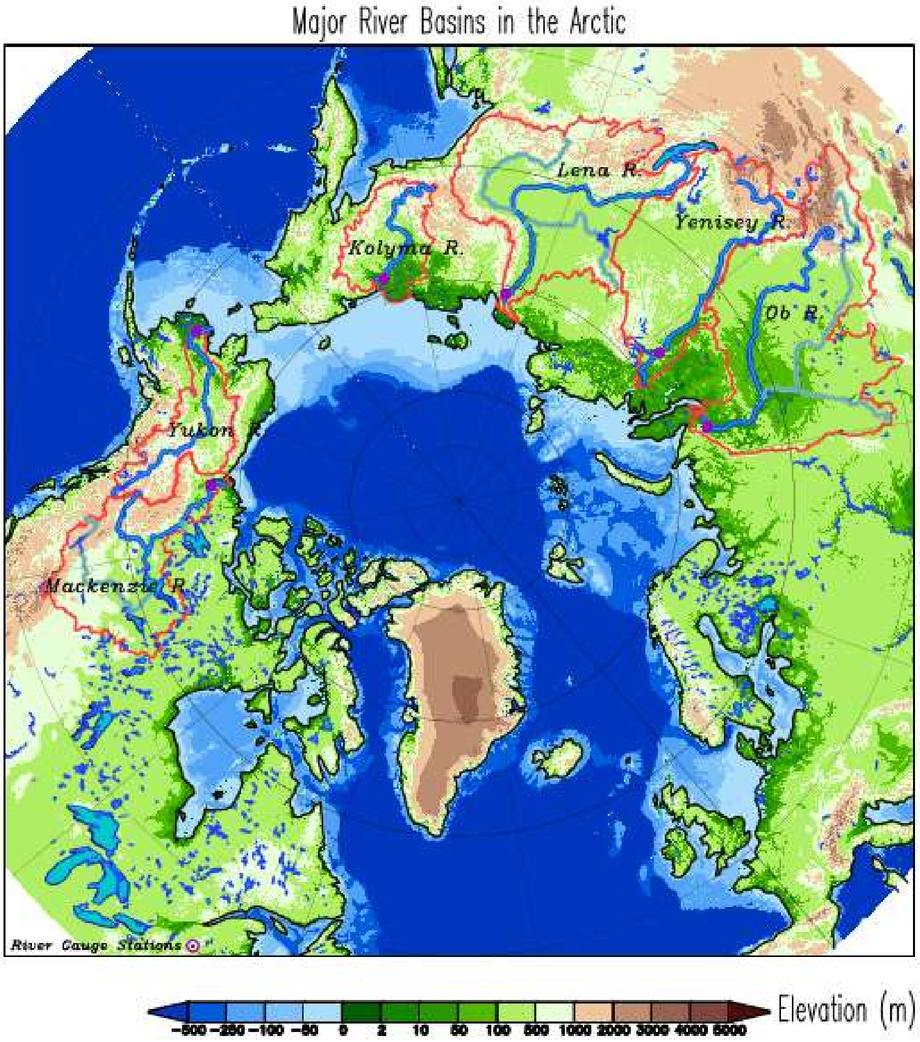

Figure 1.2. Topography and bathymetry map of the Arctic. The basins of the six major Arctic rivers (Ob, Yenisey, Lena, Kolyma, Yukon, and Mackenzie) are outlined in red. The main stem of each river is shown in blue and major tributaries are shown in light blue. The location of the river gauge station nearest the mouth of each river is noted by a purple circle. Bathymetry and topography data are obtained from the 1 arc-minute global relief ETOPO1 data set (Amante and Eakins 2009). River gauge stations are listed in Table 1.1 and include Salehard (Ob), Igarka (Yenisey), Kusur (Lena), Kolymskoye and Kolymsk (Kolyma), Pilot Station (Yukon), and Arctic Red River (Mackenzie).

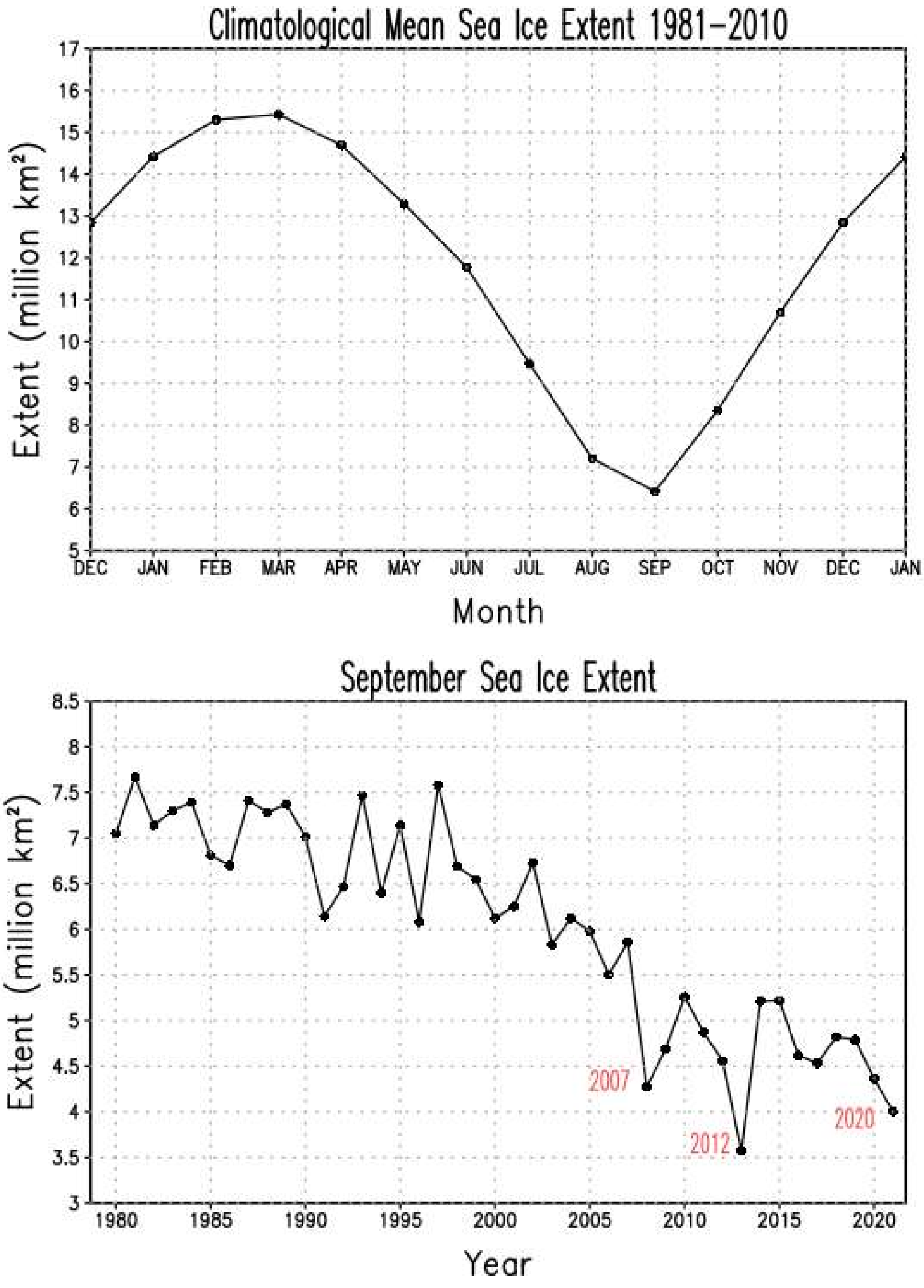

Figure 1.3. (Top) Climatological Arctic sea ice extent for 1981-2010 and (bottom) monthly mean September Arctic sea ice extent for 1979-2019, obtained from the National Snow & Ice Data Center's Sea Ice Index, Version 3 (Fetterer et al. 2017). The three years with the lowest mean September SIE (2007, 2012, and 2020) are labeled.

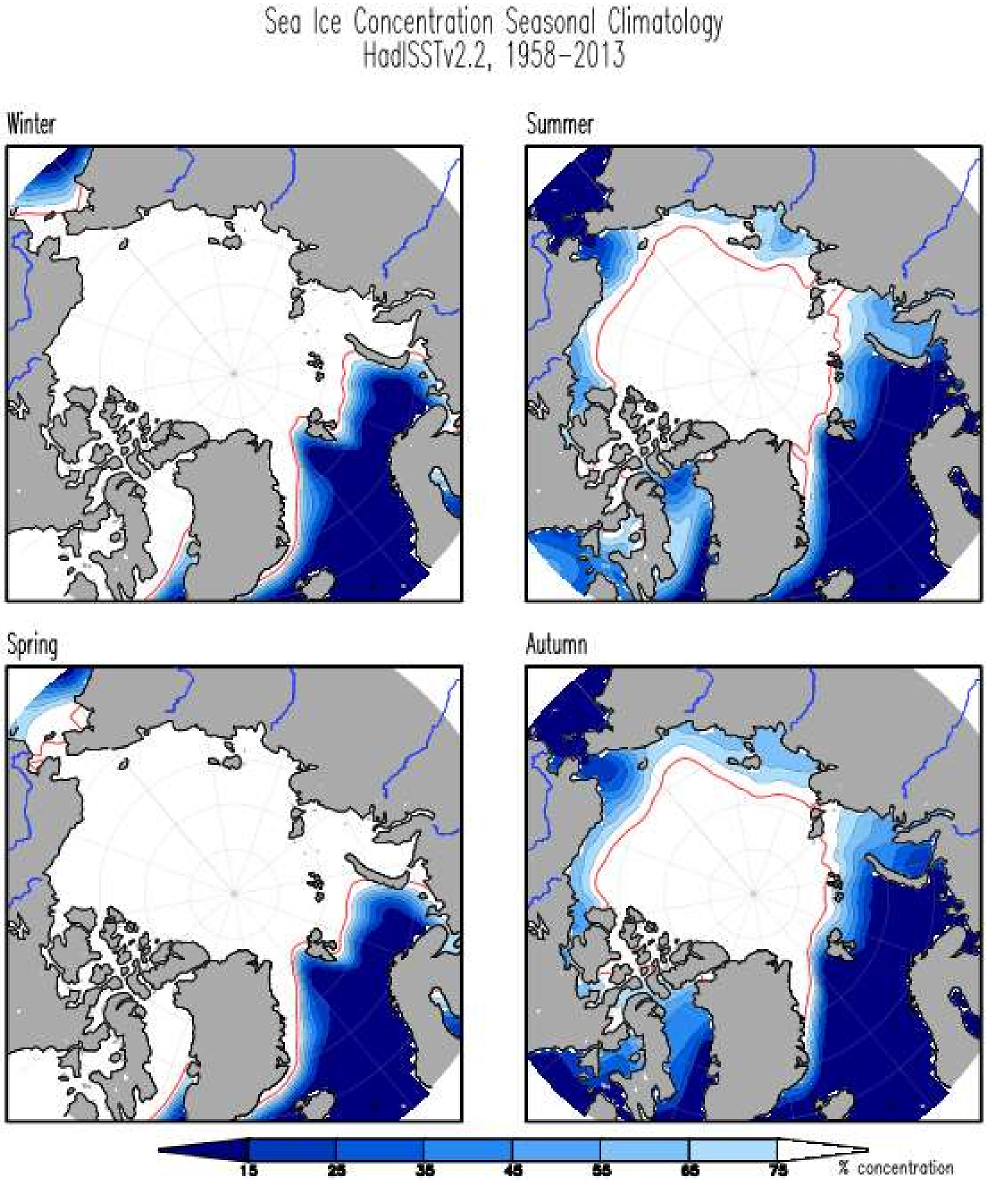

Figure 1.4. Seasonal climatology of Arctic sea ice concentration with seasons defined as winter (DJF), spring (MAM), summer (JJA), and autumn (SON). Sea ice concentration data are from HadISST2.2. Climatology is calculated from January 1958 to December 2013. Concentration is contoured every 10% from 15 to 75% and the 85% contour is plotted in red. Rivers are plotted in blue. Plots have been smoothed once using smth9.

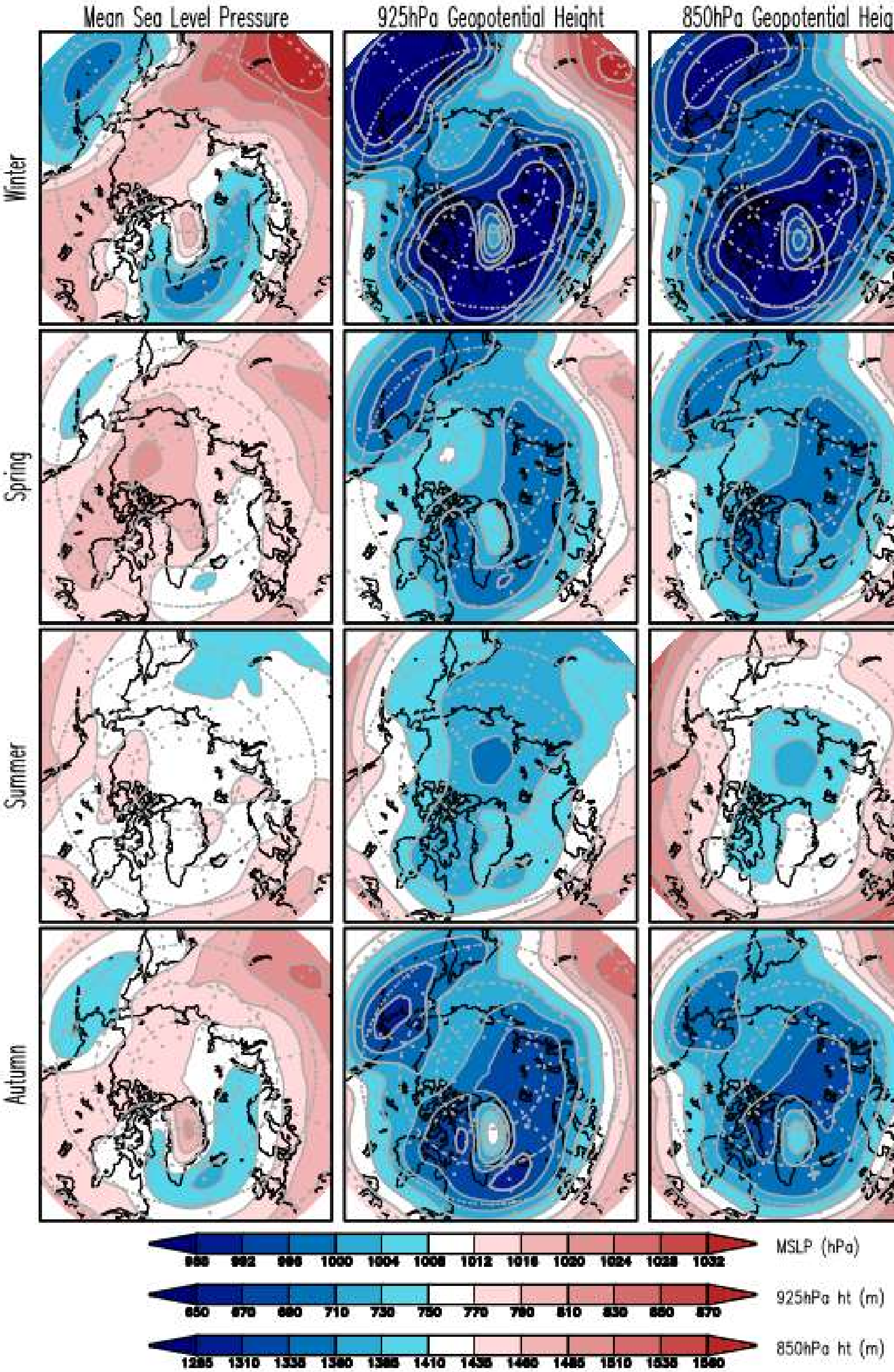

Figure 1.5. Seasonal climatology of (left) mean sea level pressure, (center) 925 hPa geopotential height, and (right) 850 hPa geopotential height for the 1979-2015 period. From top to bottom, the rows are winter (DJF), spring (MAM), summer (JJA), and autumn (SON). Contours are plotted every 4 hPa for MSLP, every 20 m for 925 mb geopotential height, and every 25 m for 850 mb geopotential height. Data from NCEP-NCAR reanalysis. Plots have been smoothed once using smth9.

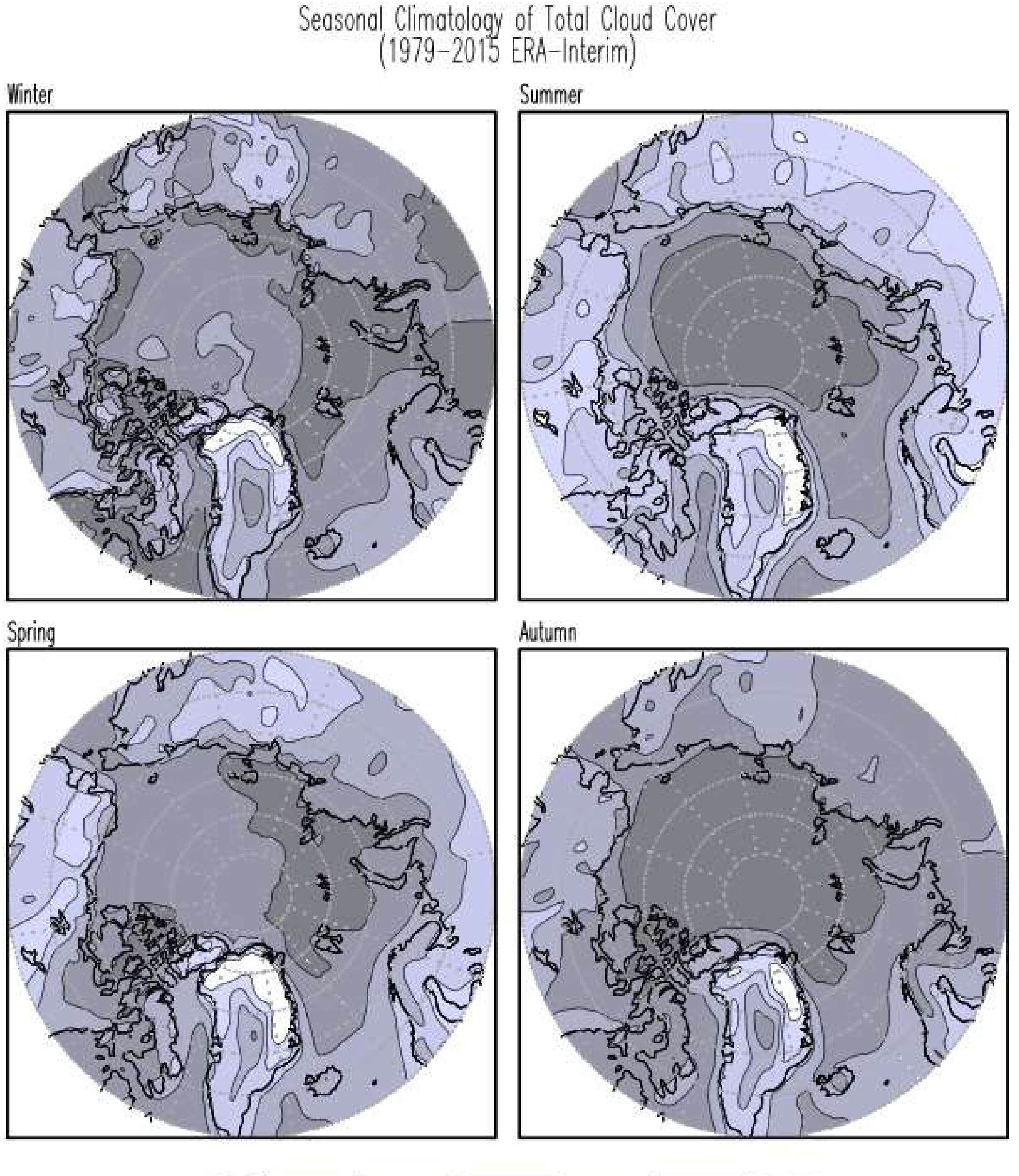

Figure 1.6. Seasonal climatology of total cloud cover for 1979-2015. Contours are plotted every 0.1 (10%) from 0.5 to 1.0 (50-100% cloud cover). Data from ERA-Interim reanalysis. Plots have been smoothed once using smth9.

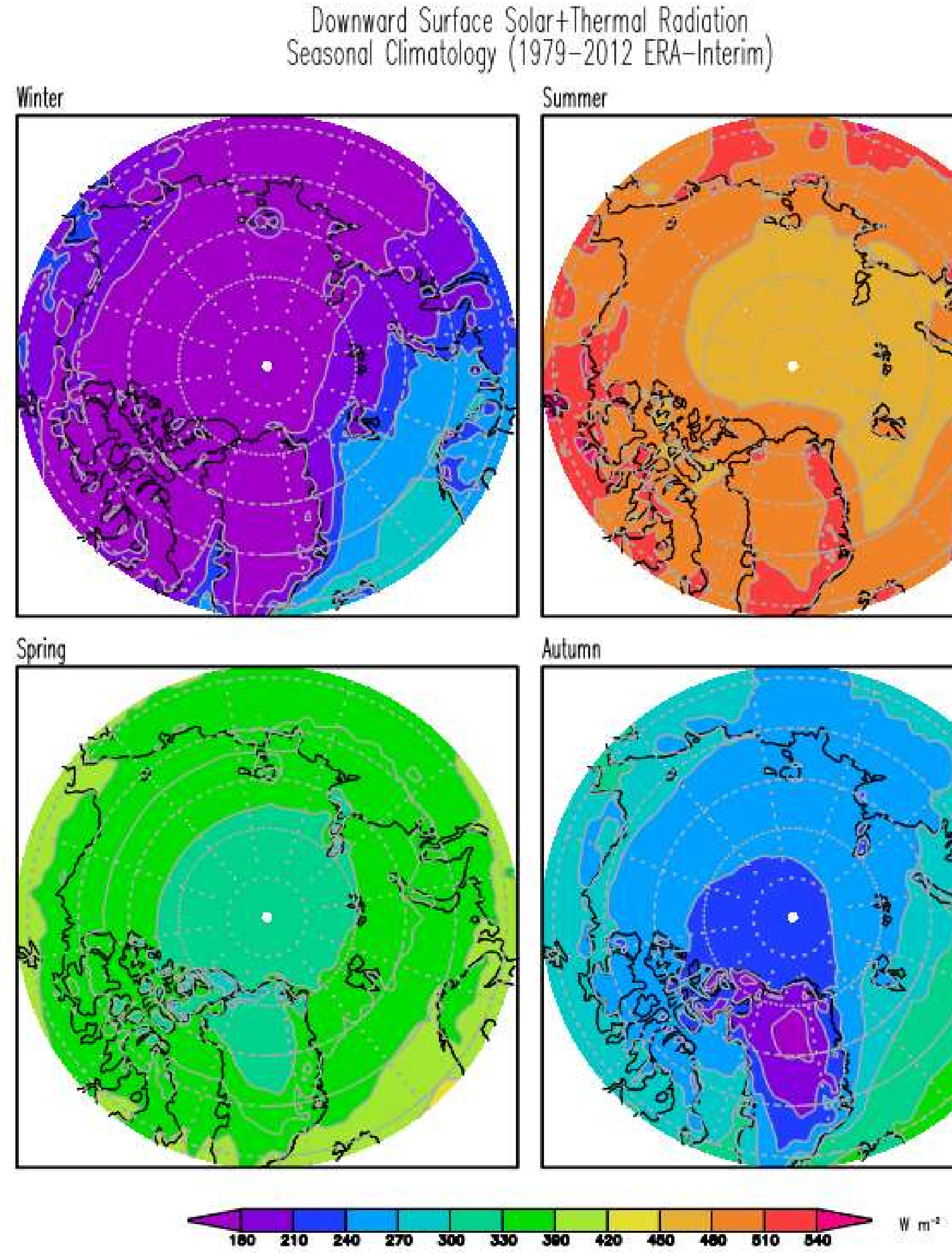

Figure 1.7. Seasonal climatology of total downward radiation (solar plus thermal). Contours are plotted every 30 W m^{-2}. Data from ERA-Interim reanalysis.

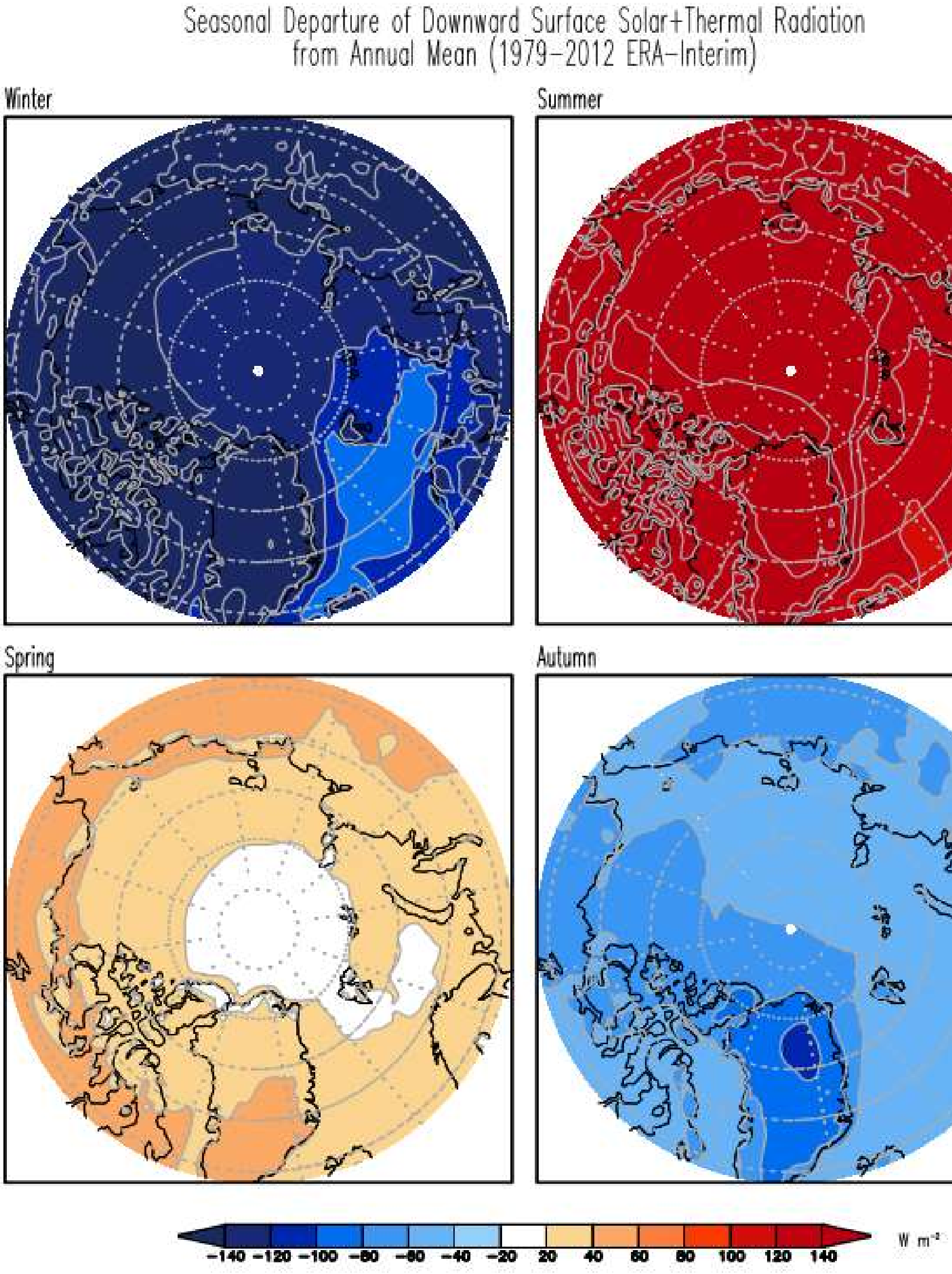

Figure 1.8. Seasonal departure (i.e., deviation from annual mean) of total downward radiation (solar plus thermal) at the surface. Contours are plotted every 20 W m^{-2}. Data from ERA-Interim reanalysis.

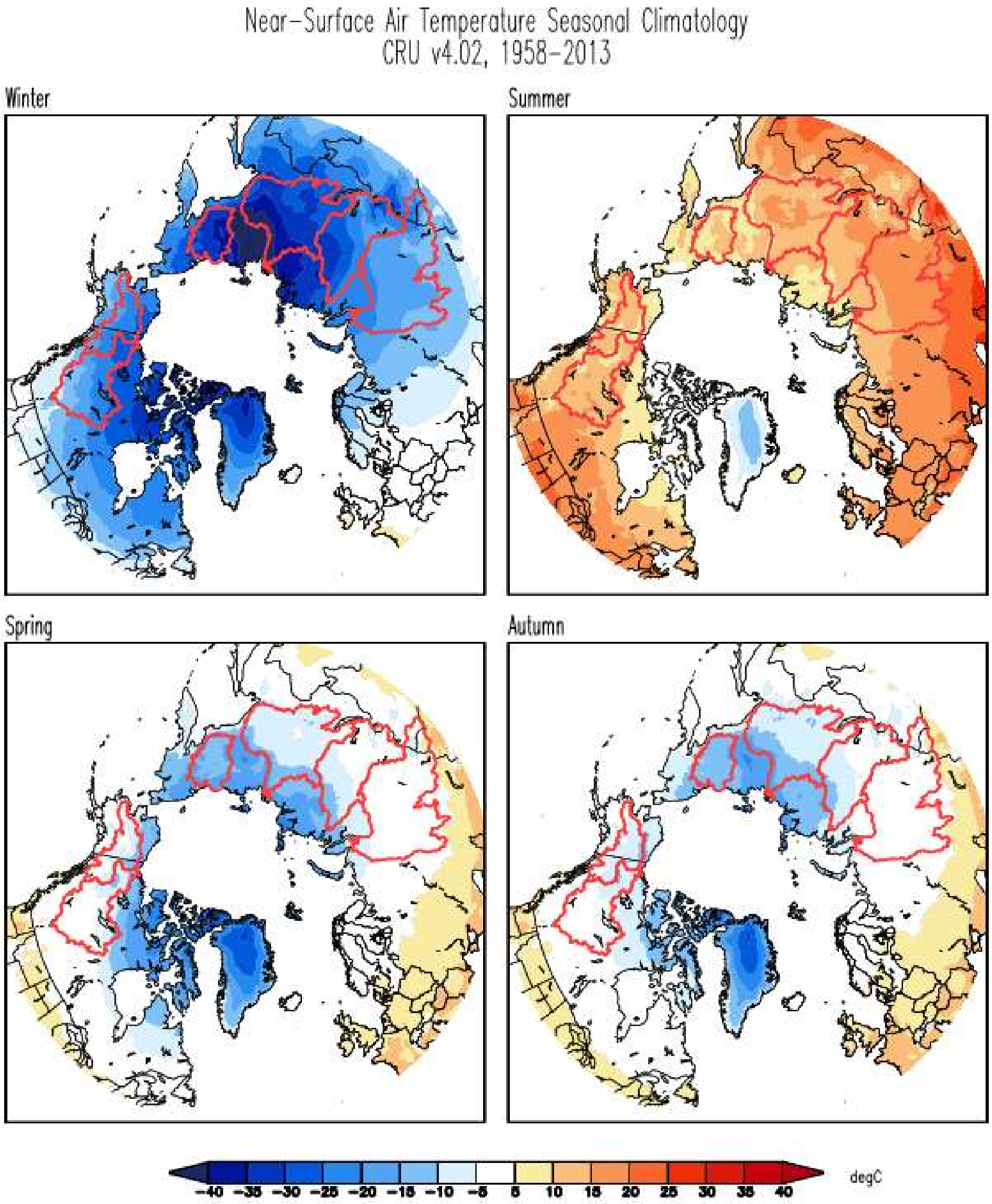

Figure 1.9. Seasonal near-surface air temperature climatology for 1958-2013. Data are from CRU TS v4.02 0.5° latitude-longitude resolution monthly data, which has been averaged into seasonal precipitation (DJF, MAM, JJA, SON). The contour interval is 5°C. The river basins are outlined in red.

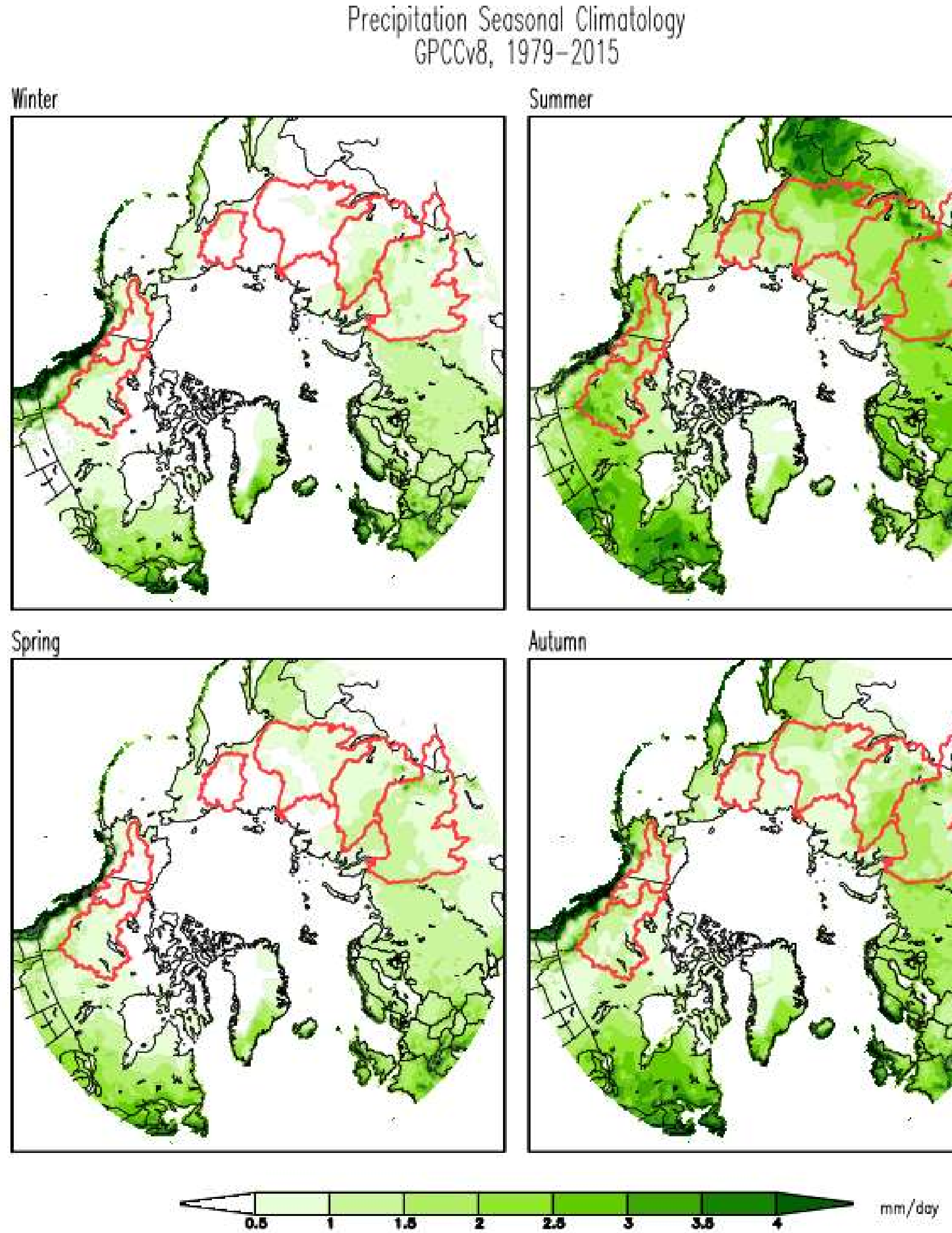

Figure 1.10. Seasonal precipitation climatology for 1979-2015. Data are from the GPCCv8 0.25° latitude-longitude resolution monthly data, which has been averaged into seasonal precipitation (DJF, MAM, JJA, SON). Green shading represents precipitation (mm day^{-1}); the contour interval is 0.5 mm day^{-1}. The river basins are outlined in red.

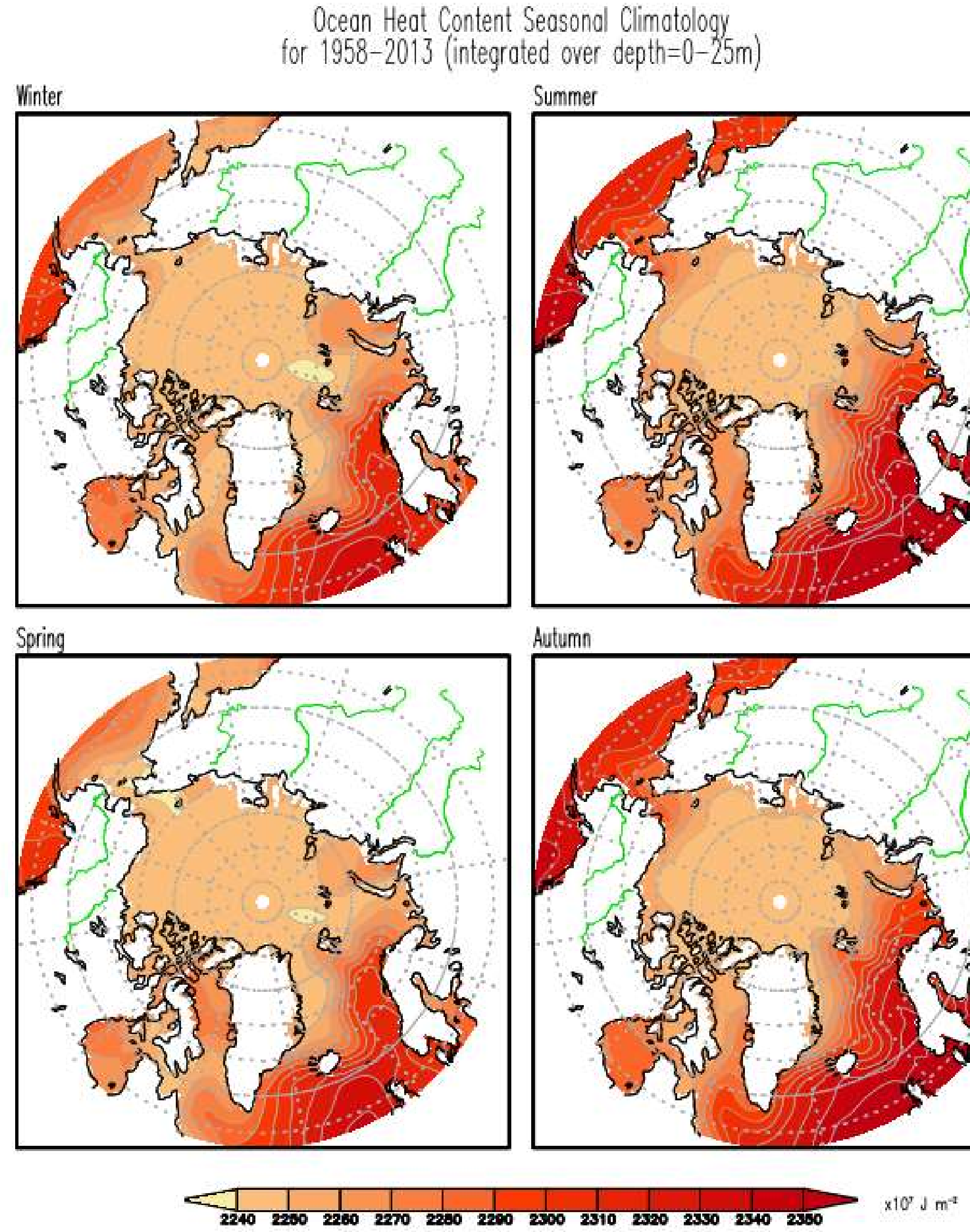

Figure 1.11. Seasonal climatology of ocean heat content in the uppermost 25 m of the ocean for 1958-2013. Ocean heat content is contoured every 10 x 10^7 J m^{-2}. Data are from EN4.2.1. Rivers are plotted in green.

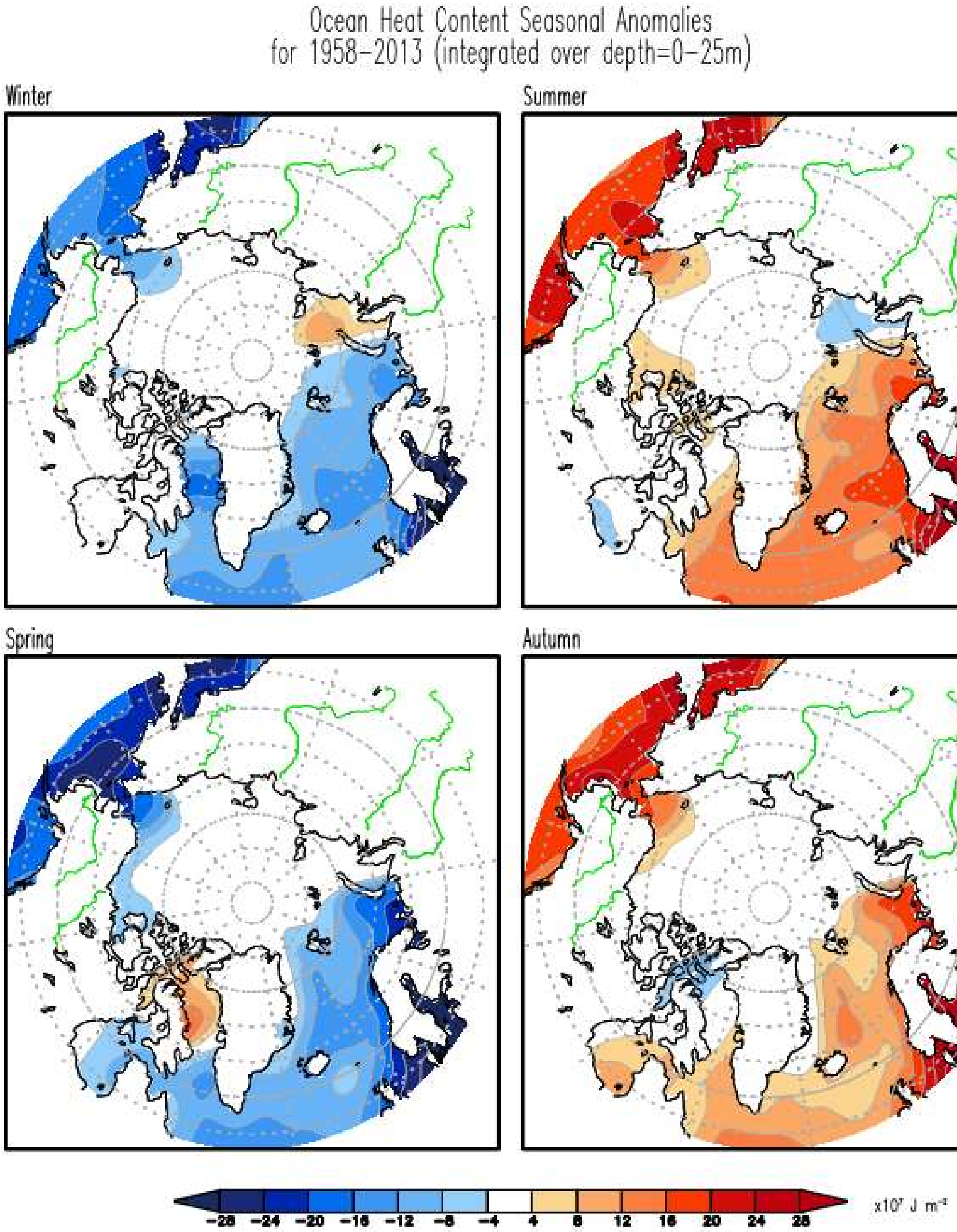

Figure 1.12. Seasonal departure (i.e., deviation from annual mean) of vertically-integrated ocean heat content (from 0-25 m) for 1958-2013. OHC is contoured every 4 x 10^7 J m^{-2}. Data from EN4.2.1. Rivers are plotted in green.

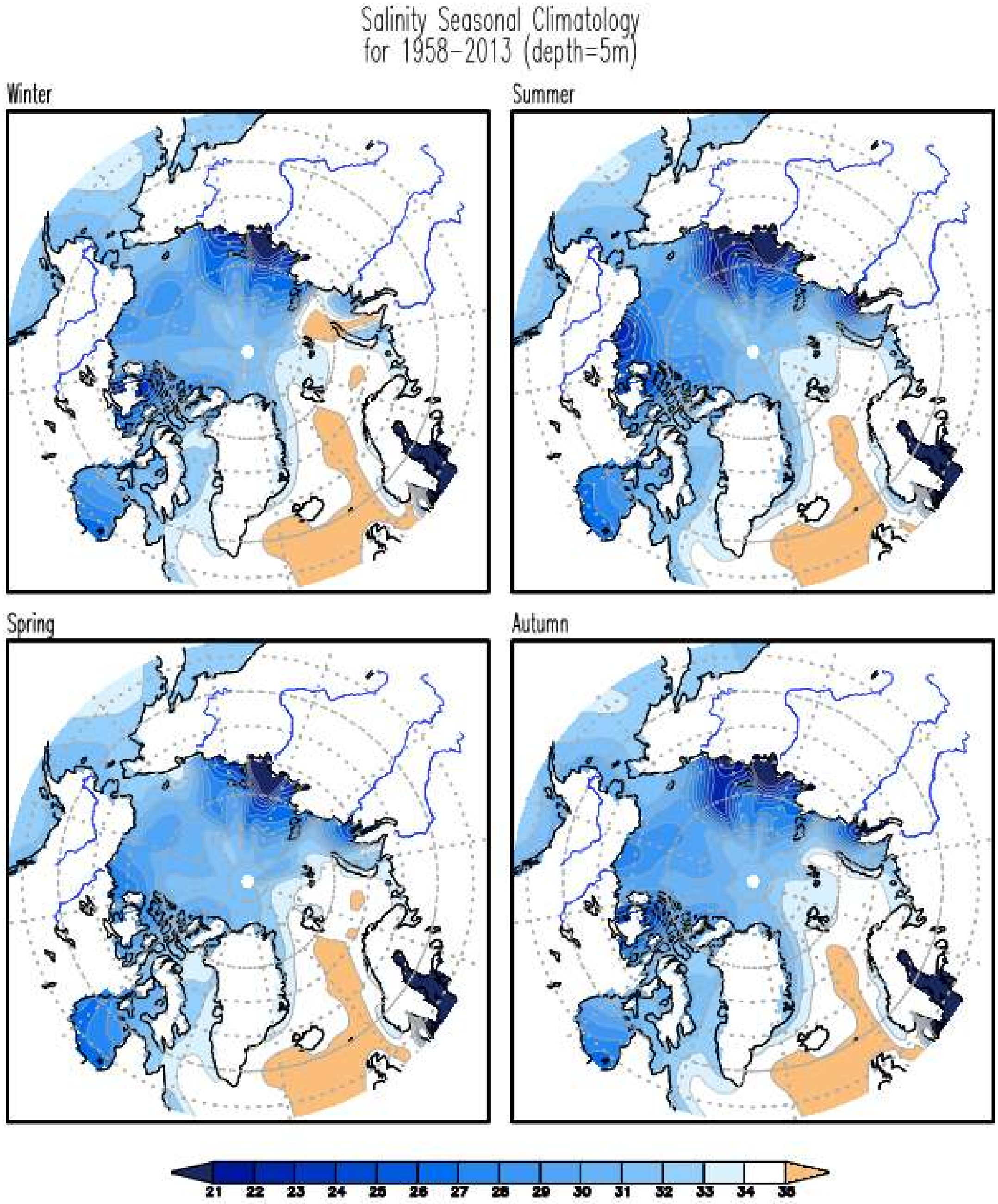

Figure 1.13. Seasonal climatology of near surface (5 m depth) salinity for 1958-2013. Salinity is contoured every 1. Data are from EN4.2.1. Rivers are plotted in blue. The reference salinity typically used in the Arctic is 34.8; blue colors therefore indicate fresher waters and orange colors indicate more saline waters than the reference salinity.

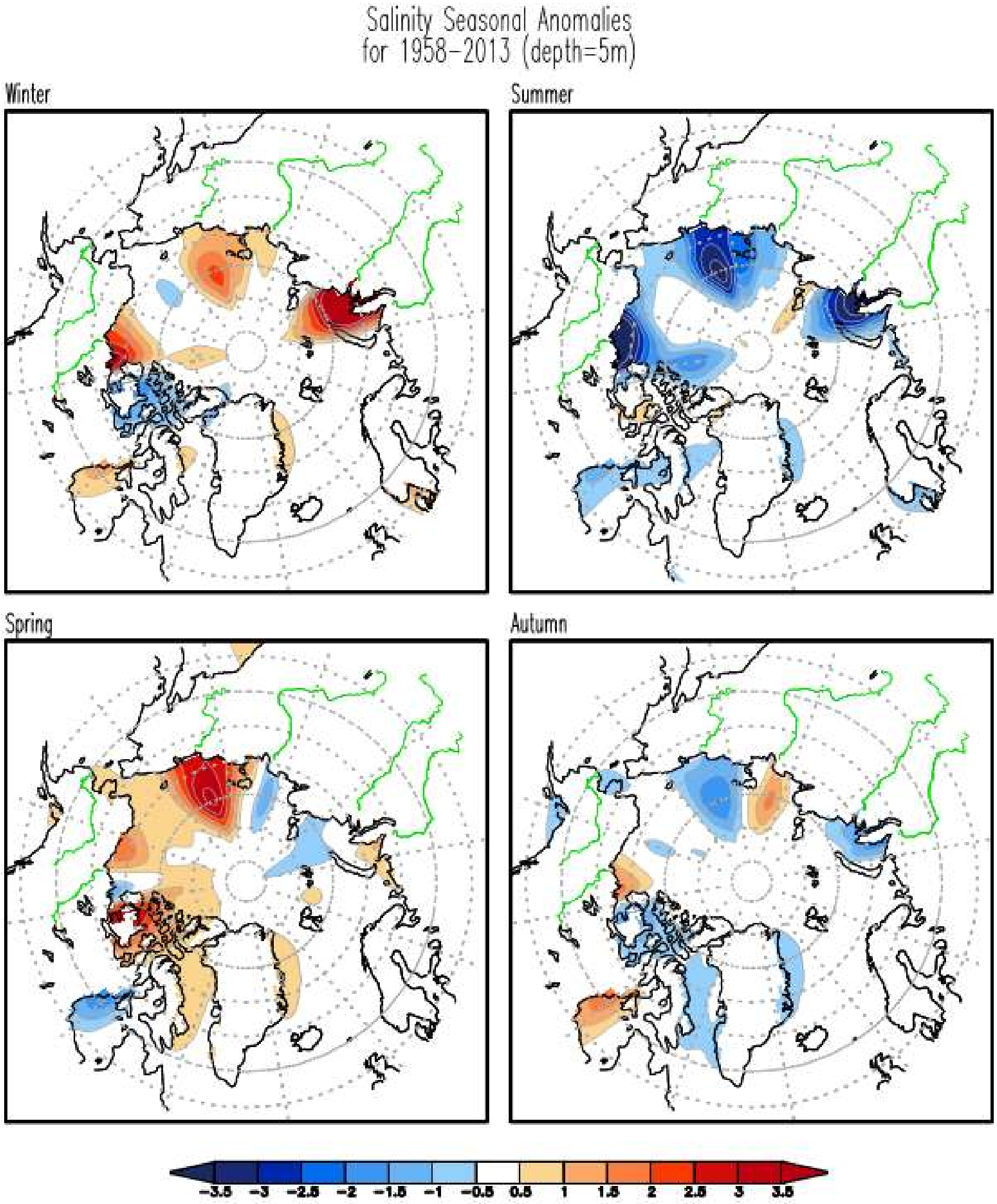

Figure 1.14. Seasonal departure (i.e., deviation from annual mean) of near-surface (at a depth of 5 m) seasonal salinity anomalies for 1958-2013. Salinity anomalies are contoured every 0.5. Data are from EN4.2.1. Rivers are plotted in green.

Chapter 2: Impact of Decadal and Multidecadal Climate Modes on Arctic Sea Ice

2.1 Background

As discussed in Chapter 1, sea ice in the Arctic is of great importance as both a key indicator and driver of climate change and climate variability. Arctic sea ice keeps the polar region cool and helps moderate global climate. While local processes modulate Arctic sea ice growth and melt, sea ice generally reaches its maximum extent sometime in late February or March, and melts through the summer, reaching a minimum at some point in September. This melting period is critical for the sea ice evolution. The less sea ice in the summer months, the more the ocean heats up and the Artic temperatures rise further that may in turn lead to greater warming over time. Year to year variability of this sea ice minimum is very sensitive to both climate variability and change from natural and anthropogenic origins. According to satellite measurements, both the sea ice thickness and sea ice extent in summer, especially in September, in the Arctic have shown a dramatic decline over the past thirty years, which has the potential to accelerate global warming trends and to change climate patterns. However, sea ice extremes can be associated with interannual variations while long-term trends (or lack of them) can be linked to decadal-to-multidecadal variability. Sea ice variations on interannual time scales are most likely associated with processes in the atmosphere originating in the tropics (e.g., Meehl et al. 2018; Zhang and Li 2017; Reusen et al. 2019), whereas decadal-to-multidecadal variations are associated with anomalies in ocean heat transport (e.g., Zhang 2015; Reusen et al. 2019).

Sea ice variations in the Arctic are not limited to the anthropogenically-driven declining trend as they also reflect natural variability. Variability in Arctic sea ice extent (SIE) has been associated with variability in the atmosphere, as identified by climate modes such as the Arctic Oscillation (AO), the North Atlantic Oscillation (NAO), and the Pacific-North American Pattern (PNA) as well as variability in the ocean as identified by climate modes such as the Atlantic Multidecadal Oscillation (AMO), Pacific Decadal Oscillation (PDO), and the North Pacific Gyre Oscillation (NPGO). A primary driver on interannual-to-decadal timescales was believed to be the NAO, with an upward trend in the NAO leading to thinning of the winter ice pack and preconditioning of the summer ice for melt; however, the NAO switched to a low phase in the early 1990s and yet Arctic SIE continued to decline (Comiso 2006; Deser and Teng 2008; Ding et al. 2017; Maslanik et al. 2007a; Overland and Wang 2005; Serreze et al. 2007; Serreze and Francis 2006) indicating that another source of variability in the system was also contributing to that decline in sea ice. Since that time, and particularly since the sea ice extent minima in 2007 and 2012 (Figure 1.3), a renewed focus has been on identifying and quantifying the contributions to Arctic sea ice variability caused by both anthropogenically-induced change and natural variability.

Multiple studies have identified decadal and multidecadal signals in observations of Arctic climate variables, including sea ice, ocean temperature, and air temperature. Decadal changes in sea ice in the Bering Sea in spring have been linked to the subsurface ocean response to the NPGO (Yang et al. 2020). Low frequency (50-80 year) variability in SIE in the Russian Arctic was identified by Polyakov et al.

(2003a). This variability was most pronounced in the Kara Sea, with the signal decaying eastward through the Laptev and East Siberian Seas, and believed to be related to the thermohaline circulation fluctuations in the North Atlantic (Delworth and Mann 2000). SIE in the Chukchi Sea was found to exhibit decadal instead of multidecadal variability (Polyakov et al. 2003a). Multidecadal variability was also found in the temperature of Intermediate Atlantic Water in the Arctic Ocean (Polyakov et al. 2004) with the largest variability in the Eurasian basin, decreasing toward the Beaufort Sea (Polyakov et al. 2003b). The multidecadal variability in the Barents Sea temperature was also found to be strongly correlated with the AMO index (Levitus et al. 2009b). More recently, Yu et al. (2017) performed EOF analysis on global (Arctic and Antarctic) seasonal sea ice concentration (SIC) and found the SIC principal component time series is positively correlated to the AMO index and negatively correlated to the PDO index. Ice export through the Fram Strait appears to also be linked to multidecadal natural variability (Smedsrud et al. 2017). Strong correlations have also been found between land-based Arctic surface temperatures and the AMO (Chylek et al. 2009). In a probabilistic analysis of Arctic sea ice, Zhang et al. (2020) found the anomalously strong anticyclonic circulation during the years of positive AO, NAO, and PNA promotes more sea ice export through the Fram Strait, resulting in excessive sea ice loss. However, if in addition to these conditions, positive AMO and PDO coincide, the sea ice decrease is amplified.

Paleoproxy records have been used to extend the observation time periods over several centuries. AMO-related variability has been found in an Icelandic sea-ice severity index for 1600-1870 (Miles et al. 2014). The sea-ice severity proxy was constructed by Moros et al. (2006) from marine core MD99-2269 north of Iceland and used the number of quartz particles in the core as a proxy for drift ice, as Iceland is composed of basalt and quartz particles are indicative of drift from elsewhere. AMO-related variability has also been found in a biomarker proxy record in the East Greenland Sea that uses sea ice diatoms to indicate the presence of seasonal sea ice cover (Kolling et al. 2017). Nicolle et al. (2017), using paleoproxy records from across the Arctic, found regional differences in the origin of the observed low-frequency variability in the proxy records: a 50-90-year cycle associated with the AMO over the North Atlantic region and a 16-30-year period associated with the PDO over the Alaskan region. Centuries-long proxy records in the Western Canadian Arctic show a statistically-significant negative correlation between the PDO and sediment deposits due to increased precipitation during negative-phase PDO (Lapointe et al. 2017).

While proxy measurements spanning multiple centuries exist, they are typically representative of a small region of the Arctic. Observations that cover the entire Arctic basin are generally limited to satellite measurements, which are available since 1979. This limited temporal length of pan-Arctic observations has led to the use of climate model data to address the connection between multidecadal oscillations and Arctic SIE. Using a 1000-year segment of a control simulation of GFDL-CM2.1, Mahajan et al. (2011) found both the Atlantic Meridional Overturning Circulation (AMOC) and AMO indices to be anticorrelated with Arctic SIE, with the AMO having a stronger correlation than the AMOC. Day et al. (2012), using control simulations from five CMIP3 models, found a decline of 0.5-3.1% decade^{-1} out of the total observed decline of 10.1% decade^{-1} for 1979-2010 to be related to the AMO (5-30% of satellite-era SIE decline). No link was found between the AO and SIE (Day et al. 2012). Zhang (2015), using a 3600-year segment from a GFDL-CM2.1 control simulation, found AMO, PDO, and winter NAO/AO have indirect causal effects on September SIE through their modifications of ocean heat transport. In another study, the PDO index time series was found to only be weakly correlated to pan-Arctic winter sea ice area (Screen and Francis 2016). A recent modeling study using sea surface temperatures (SST) characteristic of the positive and negative phases of the Atlantic Multidecadal Variability (AMV) found that the Arctic atmospheric circulation pattern can change under these conditions (SSTs were time independent) and can impact sea ice through dynamic forcing on ice drift and thermodynamic effects on winter sea ice formation (Castruccio et al. 2019). Additionally, they found that the maximum expression occurred in the Pacific sector. Their experiments showed that dynamic forcing was through sea level pressure (SLP) anomalies and associated wind anomalies which modified the wind-driven ice drift pattern in the Beaufort Gyre and the Transpolar Drift Stream, while the warm winter surface anomalies were associated with increased cloudiness and increased downwelling longwave radiation, which slowed winter sea ice growth. These two effects resulted in thinner and younger Arctic sea ice. Yu et al. (2019) performed a self-organizing map analysis on daily sea ice data and found two primary modes of variability: one in the Pacific sector and one in the Barents and Kara Sea. A phase reversal in these modes from positive to negative occurred in the late 1990s, at the same time as a shift in the PDO and AMO indices; however, their analysis did not establish the causal relationship between the PDO, AMO, and reduced Arctic sea ice (Yu et al. 2019). The observational, paleoproxy, and model studies discussed above have shown that the AMO impacts variability in the Atlantic sector of the Arctic and the PDO impacts variability in the Pacific sector, but less consideration has been given to how these cycles may have cross-basin impacts and how they might be offsetting or reinforcing each other.

This chapter aims to explain the observed sea ice decadal trends from the trends imposed by decadal-to-multidecadal modes of SST variability. The analysis presented in this chapter investigates the spatiotemporal multidecadal variability in Arctic sea ice concentration (SIC) through regression analysis, considering several Atlantic- and Pacific-focused natural low-frequency modes of climate variability as potential contributors. Section 2.2 will discuss the data and methods while Section 2.3 will present the results. Section 2.4 will provide a summary.

2.2 Data Sets and Analysis Techniques

2.2.1 Data Sets

Monthly mean SIC fields from the Met Office Hadley Centre's Sea Ice and Sea Surface Temperature data set version 2.2.0.0 (HadISST2.2) is available globally for 1850 to 2017 at 1° spatial resolution (Titchner and Rayner 2014). A second SIC data set, the Gridded Monthly Sea Ice Extent and Concentration, 1850 Onward (SIBT1850), providing quarter-degree-resolution for the SIC and SIE fields (Walsh et al. 2015) from 1850-2013, was also used to investigate the robustness of the results from the HadISST2.2 dataset. Additional details about these two data sets can be found in Section 1.2.2.

Two time periods were investigated in this analysis. The 1958-2013 time period was selected to coincide to start with the International Geophysical Year (July 1957-December 1958) and represents the time period where more sea ice observation data are available. The second time period analyzed is 1979-2013, coinciding with the era of satellite observations of sea ice.

2.2.2 Climate Modes from an SST-based Analysis

The low-frequency variability modes were obtained from a spatiotemporal (Rotated Extended Empirical Orthogonal Function) analysis of 118 years of observed seasonal SST data from Nigam et al. (2020) that allowed the objective identification of eleven SST modes of variability. The analysis presented in this chapter focuses on the spatiotemporal multidecadal variability of Arctic SIC and thus modes of interest from the Nigam et al. (2020) analysis include Pacific decadal variability (PDV) that has footprints in the midlatitudes of the North Pacific (PDV-NP) and footprints in the Pan-Pacific domain (PDV-PP), along with modes in the Atlantic Ocean, such as the AMO, a Low-frequency NAO (LF-NAO) mode, and a Sub-Arctic decadal variability (SADV) mode. The PDV-NP mode and Mantua’s PDO index are negatively correlated: the positive phase of the PDV-NP corresponds to the negative phase of the PDO (Nigam et al. 2020); similarly, the PDV-PP mode and NPGO index (Di Lorenzo et al. 2008) are negatively correlated, that is, the positive phase of the PDV-PP corresponds to the negative phase of the NPGO (Nigam et al. 2020). The footprints of the positive phase of these climate modes on the SST fields and the corresponding principal component (PC) time series are shown in Figure 2.1.

2.2.3 Regression Analysis Methodology

To investigate the influence of low-frequency climate variability on Arctic SIC and specifically on the SIC minima in September, regression analysis of the fall-season decadal and multidecadal PC time series with September SIC were performed. The PDV-PP, AMO, PDV-NP, LF-NAO, and SADV time series were normalized over the 1958-2013 time period. The linearly-detrended monthly SIC fields were then regressed on the normalized time series. The linear trends removed from the monthly SIC fields were calculated using the least-squares method. The influence of each mode was quantified through reconstructing the September SIC by multiplying the September SIC regressed anomalies for each mode by the PC of that mode.

2.3 Results

2.3.1 Sea Ice Climatology and Variability

The seasonal variability in SIC was presented previously in Figure 1.4. Winter and spring SIC are very similar, with ice along the coastlines surrounding the Arctic Ocean, with the exception of the Barents Sea. Beginning in the summer, sea ice in the Arctic recedes from the coasts and reaches a minimum in autumn. The timing and extent of the sea ice retreat northward varies around the Arctic. Figure 2.2 provides higher temporal resolution during the melt period by focusing on the monthly climatological SIC and its standard deviation from mid-summer to mid-fall (July through October). Each monthly SIC plot includes the 85% concentration contour, plotted in red. In July, the reduction in SIC is seen in the regions coinciding with Pacific inflow through Bering Strait and near river mouths, specifically the Mackenzie River in Canada and the Ob, Yenisey, and Lena Rivers in Siberia. Additionally, loss of sea ice in the northern Barents Sea and the Kara Sea are impacted by warm waters entering the Arctic with the North Atlantic Drift current. The minimum in SIE, and the lowest SIC in the marginal seas, occurs in September.

Year-to-year variability of SIC in the marginal seas surrounding the Arctic Ocean is evident in the standard deviation plots. In July, the regions of largest variability are adjacent to the coasts, reflecting the year-to-year differences in the timing of the retreat of the ice edge from the coast. In August and September, the regions of largest SIC variability are further north away from the coasts. This is indicative of year-to-year differences in the northward extent of ice melt and ice edge location which result in large variability, while the melt that occurs annually along the coasts results in low variability there. The monthly climatology of SIC calculated using the SIBT1850 dataset are very similar to those calculated using the HadISST2.2 dataset, as shown in Figure 2.3. The region of the Beaufort and Chukchi Seas has some of the largest variability and largest seasonal sea ice retreat; this area (72-78°N, 140-170°W) will be referred to as the Beaufort-Chukchi study area (BCSA), although it should be noted that this area does not encompass all of the Beaufort and Chukchi Seas. The boundaries of this region were selected as they include the region of maximum variability in the North American Arctic.

A BCSA sea ice index was calculated by first computing the anomalous September SIC field as a deviation from the mean 1958-2013 September SIC. The anomalies were then area-averaged over the 72-78°N, 140-170°W box. The BCSA index, shown in Figure 2.4, is thus the area-averaged September SIC anomaly within that box. The linear trends of the BCSA index over two time periods, 1958-2013 and 1979-2013, were calculated and are plotted as the blue (1958-2013) and red (1979-2013) lines in Figure 2.4. The area-averaged September SIC anomaly indicates the SIC was fairly consistent from 1958 to the early 1990s with a rapid decrease beginning in the 1990s. Over the full period starting in 1958, the SIC trend is -12.12% decade^{-1}, while it is -24.12% decade^{-1} over the satellite era from 1979-2013 (SIBT1850 data set has trends of -11.68% decade^{-1} and -24.99% decade^{-1} for the 1958-2013 and 1979-2013 periods, respectively). The increasingly anomalous SIC in the study area is presumably due to both natural variability and anthropogenic causes. In an effort to understand the geographic footprint of the SIC anomaly trend found in the study region and whether the sea ice loss in this region is accompanied by sea ice loss in other basins, the linearly-detrended monthly SIC of the antecedent July and August, simultaneous September, and subsequent October (bottom of Figure 2.4) were regressed on the BCSA sea ice index time series. The temporal phasing shows a northwestward expansion of the declining SIC into the East Siberian Sea from July to August. This is followed in September by a more pronounced decline of SIC in the Beaufort and Chukchi Seas and a northward expansion toward the central Arctic Ocean. Finally, by October, the SIC decline returns to August levels but is evident around the Arctic from the Beaufort Sea to the Kara Sea.

Of particular interest is to find out if the decreasing trends in SIC over the Beaufort and Chukchi Seas in particular, and over other Arctic regions in general, arise as a consequence of low-frequency natural variability. The five main SST-based modes of Pacific and Atlantic low-frequency variability discussed in Section 2.2.2 were used to investigate links between natural low-frequency variability and September SIC in the BCSA. Figure 2.5 (top panels) shows the principal component time series of Atlantic-focused modes (AMO, LF-NAO, SADV) and Pacific-focused modes (PDV-PP, PDV-NP) in autumn for 1958-2013. Linear trend lines for both 1958-2013 and 1979-2013 are included with the time series. Over the latter period, the AMO, SADV, and PDV-NP have both changed from negative to positive phases while the PDV-PP and LF-NAO have changed from a positive to a negative phase.

Anomalies in SIC associated with these modes reveal distinctive patterns. The linearly-detrended July through October monthly SIC fields were regressed on the autumn PC time series for each of the five modes (Figure 2.5, lower panels). Each mode displays a monthly progression, as the spatial extent of the signal grows in size through these months. Notably, all modes impact SIC across the Arctic, but each in slightly different regions. The AMO, LF-NAO, and PDV-PP have their largest impacts in the Beaufort and Chukchi Seas, with the influence of the AMO nearer to the coast while that of the PDV-PP is shifted north. The PDV-NP has its largest impact along the Russian coastline, stretching westward with time from the East Siberian Sea to the Kara Sea. The SADV mode’s impact on SIC is initially focused in the Barents Sea in July with impacts spreading to the marginal seas throughout the Arctic in subsequent months. Positive phases (and trends) of the AMO, SADV, and PDV-NP are both associated with SIC loss, while positive phase (and trend) of the PDV-PP and LF-NAO are associated with SIC gain. This result is in agreement with

Yu et al. (2017) who found the leading mode of global SIC variability to be positively correlated with AMV and negatively correlated with the PDO; as mentioned previously, the PDO and PDV-NP are negatively correlated. From 2007 until about 2014, the AMO and PDV-NP have been in positive phases and the PDV-PP has been in a negative phase, all of which are associated with loss of SIC.

2.3.2 Sea Ice Trends due to Natural Low-Frequency Variability

To investigate the contribution of each natural low-frequency variability mode to the SIC trend in the study area and in the Arctic in general, the September SIC was reconstructed by multiplying the SIC regressed anomalies for each individual variability mode by the principal component time series of that mode. In addition, the September SIC due to the secular mode, i.e., the first principal component from the Nigam et al. (2020) spatiotemporal analysis, was reconstructed. For only the reconstruction of the secular mode, the original (i.e., not linearly-detrended) SIC field was used. The linear trend of the reconstructed September SIC due to each low-frequency individual mode, was calculated over the 1958-2013 and 1979-2013 time periods and is shown in Figure 2.6. While the secular mode is the main contributor to the declining SIC over both time periods, the decadal and multidecadal modes of variability provide additional SIC loss, or gain in the case of the LF-NAO, over the study area. The contributions of the individual low-frequency modes to SIC loss over the longer 1958-2013 time period is muted for most of the modes because more of their full period, both the positive and negative phases, is included. The contribution of these modes to sea ice loss over the 1979-2013 time period is more pronounced, particularly for the AMO, PDV-PP, and PDV-NP as this time period aligns to phases that result in sea ice loss due to all three modes.

The SIC trend averaged over the BCSA is listed in Table 2.1 for each of the individual contributors. Over the 1979-2013 period, the AMO contributes to SIC decline in the BCSA of nearly 4% decade^{-1}, while the PDV-PP contributes to a decline of just over 3% decade^{-1}. The SADV and PDV-NP each contribute just over 1% decade^{-1} loss each. The LF-NAO contributes a gain of 0.1% decade^{-1}. Over the longer 1958-2013 period, the LF-NAO leads to an increased trend of about 2.5% decade^{-1} in the study region and the PDV-NP and SADV also have positive trends, although it is less than 1% decade^{-1} each. Over the 1958-2013 period, the low-frequency variability modes that contribute to increasing and decreasing SIC approximately balance.

Declining SIC is occurring in regions throughout the Arctic in general. The observed and reconstructed SIC trend in September averaged over the Arctic basin from 70-90°N was also calculated and listed in Table 2.2. The decline in September SIC is not as pronounced when averaged over the full Arctic, about -4% decade^{-1} from 1958-2013 and -7% decade^{-1} for 1979-2013. Sea ice concentrations in the central Arctic have not changed as dramatically as they have in the marginal seas. However, there has been extensive SIC loss in September along the Siberian shelves, mostly due to contributions from the secular trend and minor contributions from the AMO, PDV-PP, PDV-NP, and SADV. Reconstructed September SIC indicates an increasing trend of SIC in the Laptev Sea associated with the positive phases of the

AMO and PDV-NP and in the Kara Sea associated with the positive phase of the AMO.

To quantify the total impacts of low-frequency climate variability on the SIC in the Arctic, the September SIC was reconstructed by first regressing the linearly-detrended September SIC on each of the autumn AMO, LF-NAO, SADV, PDV-NP, and PDV-PP PC time series, multiplying the regressed SIC anomalies by its corresponding PC time series, and then summing the five individual reconstructions. Figure 2.7 compares the linear trend of the observed and reconstructed September SIC fields over both the 1958-2013 and 1979-2013 periods. The observed data has not been detrended, and thus includes SIC loss due to the secular trend and other sources of variability. Note that the secular trend (Figure 2.6) contributes the most to the observed declining September linear trend (Figure 2.7) along eastern Greenland that extends northeastward along the 80°N latitude circle to the northeastern portion of the Kara Sea. If the observed linear trend in September SIC was solely due to decadal and multidecadal variability, the linear trend of the reconstructed field would match that of the observed field. The linear trends of the reconstructed and observed SIC over 1979-2013 have similar geographic extents and the strongest negative trends in both fields are found in the Beaufort, Chukchi, and Laptev Seas. In the BCSA, the trend in the reconstructed SIC due to low-frequency climate variability is -9.75% decade^{-1} while the observed trend is -24.12% decade^{-1}. This suggests that low frequency variability accounts for about 40% of the September SIC loss since 1979. The linear trend in reconstructed September SIC using the SIBT1850 dataset is similar with a -10.13% decade^{-1} trend, of the total -25% decade^{-1} trend, due to low-frequency variability (Figure 2.8). The reconstruction over the 1958-2013 period shows a very small (<1%) positive trend over the Arctic. This, in combination with the visible trends over the shorter 1979-2013 period, suggests that 1958-2013 is one full cycle of the superposition of the AMO, LF-NAO, SADV, PDV-PP, and PDV-NP signals on the sea ice.

2.4 Summary

The focus of this analysis has been to document the relationship between natural low-frequency climate variability modes and SIC trends in the region of the Beaufort and Chukchi Seas specifically and in the Arctic in general. This study shows that both the Atlantic-focused and Pacific-focused modes contribute to SIC variability across the Arctic and their influence is not confined to only the Atlantic or only the Pacific sectors. Of the total declining trend of 24.12% decade^{-1} from 1979 to 2013, 9.75% decade^{-1} can be attributed to the five decadal and multidecadal modes considered here (AMO, LF-NAO, SADV, PDV-PP, PDV-NP), while 11.74% decade^{-1} can be attributed to the secular decline in SIC. Approximately an additional 2.6% decade^{-1} decline is not explained by either the secular decline or the five low-frequency climate modes included in this study.

The cumulative impact of these natural low-frequency variability modes on the observed declining trends in SIC is a complex interplay depending on the phase of each mode. To better understand the mechanisms that link the decadal and multidecadal modes to the geographically-varying trends in SIC, the following chapter considers the impact of these modes on the Arctic Ocean, the Arctic atmosphere, and the continental pathway linking sea ice variability with variability in the regional hydroclimate.

Table 2.1. Observed September SIC anomaly trend in the Beaufort-Chukchi Seas Area over 1958-2013 and 1979-2013. Reconstructed September SIC anomaly trends based on the secular mode and on low-frequency variability modes, both individually and cumulatively.

	Linear trend 1958-2013 (% decade^{-1})		**Linear trend 1979-2013 (% decade^{-1})**	
	HadISST2.2	**SIBT1850**	**HadISST2.2**	**SIBT1850**
Observed SIC	-12.12	-11.68	-24.12	-24.99
Reconstructed SIC (PC4+5+7+10+11)	+0.67	+0.81	-9.75	-10.13
Secular Trend (PC1)	-9.77	-9.66	-11.74	-11.61
PDV-PP (PC4)	-1.14	-1.30	-3.23	-3.69
AMO (PC5)	-1.54	-1.47	-3.84	-3.67
PDV-NP (PC7)	+0.57	+0.59	-1.56	-1.62
LF-NAO (PC10)	+2.52	+2.71	+0.13	+0.15
SADV (PC11)	+0.27	+0.29	-1.24	-1.30

Table 2.2. Observed September SIC anomaly trend in the Arctic (70-90N, 180W-180E) over 1958-2013 and 1979-2013. Reconstructed September SIC anomaly trends based on the secular mode and on low-frequency variability modes, both individually and cumulatively.

	Linear trend 1958-2013 (% decade^{-1})		**Linear trend 1979-2013 (% decade^{-1})**	
	HadISST2.2	**SIBT1850**	**HadISST2.2**	**SIBT1850**
Observed SIC	-4.02	-3.80	-7.26	-7.72
Reconstructed SIC (PC4+5+7+10+11)	+0.20	+0.22	-2.53	-2.91
Secular Trend (PC1)	-3.31	-3.27	-3.97	-3.93
PDV-PP (PC4)	-0.33	-0.39	-0.92	-1.10
AMO (PC5)	-0.25	-0.24	-0.61	-0.60
PDV-NP (PC7)	+0.18	+0.20	-0.49	-0.56
LF-NAO (PC10)	+0.48	+0.49	+0.03	+0.03
SADV (PC11)	+0.12	+0.15	-0.53	-0.68

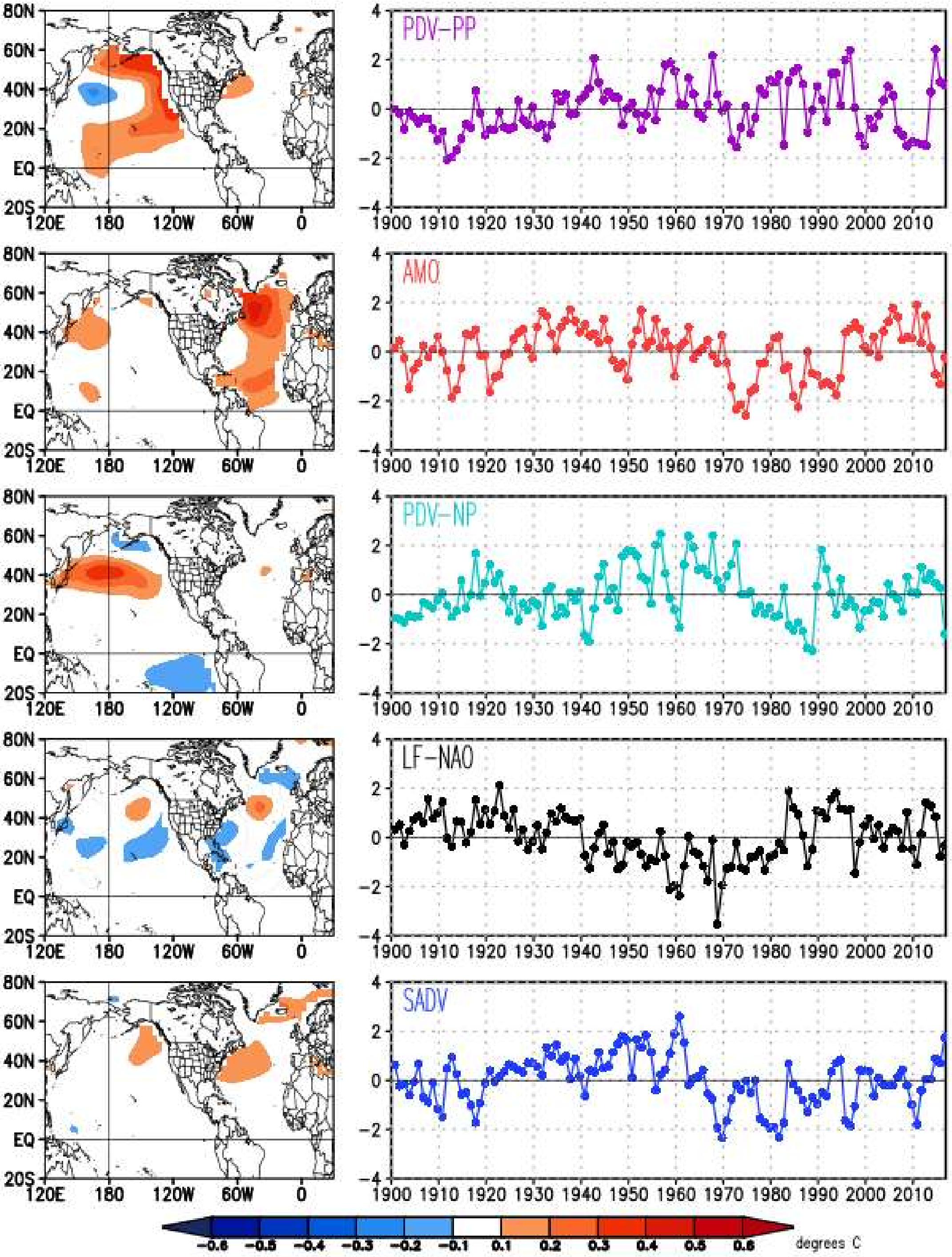

Figure 2.1. (Left) Simultaneous SST regressed anomalies and (right) principal component time series in autumn for PDV-PP, AMO, PDV-NP, LF-NAO, and SADV. Orange (blue) shading indicates positive (negative) SST anomalies.

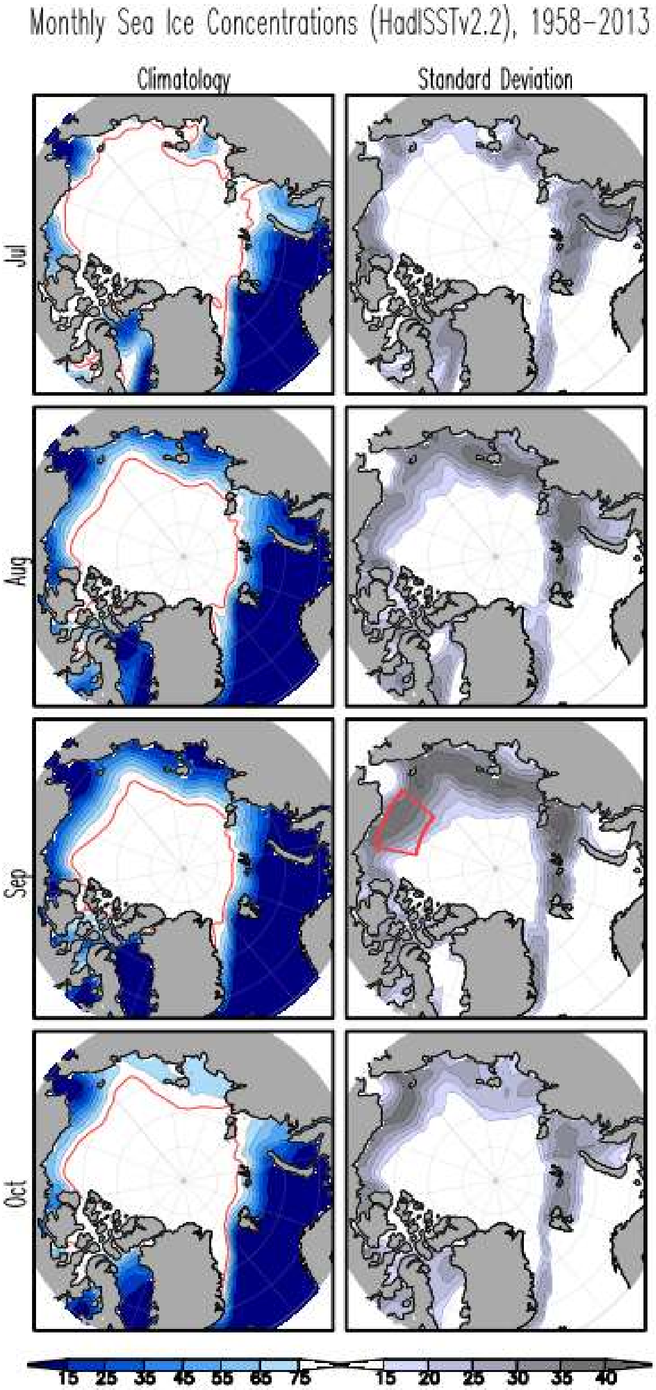

Figure 2.2. Monthly climatology (left) and standard deviation (right) of July through October Arctic SIC for 1958-2013. Data from HadISST2.2. SIC is contoured every 10% and the 85% contour is plotted in red; the standard deviation is contoured every 5%. Mean and standard deviation plots have been smoothed once using the GrADS function smth9. The red box in the September standard deviation plot outlines the Beaufort and Chukchi Seas area that is used to compute a sea ice anomaly index.

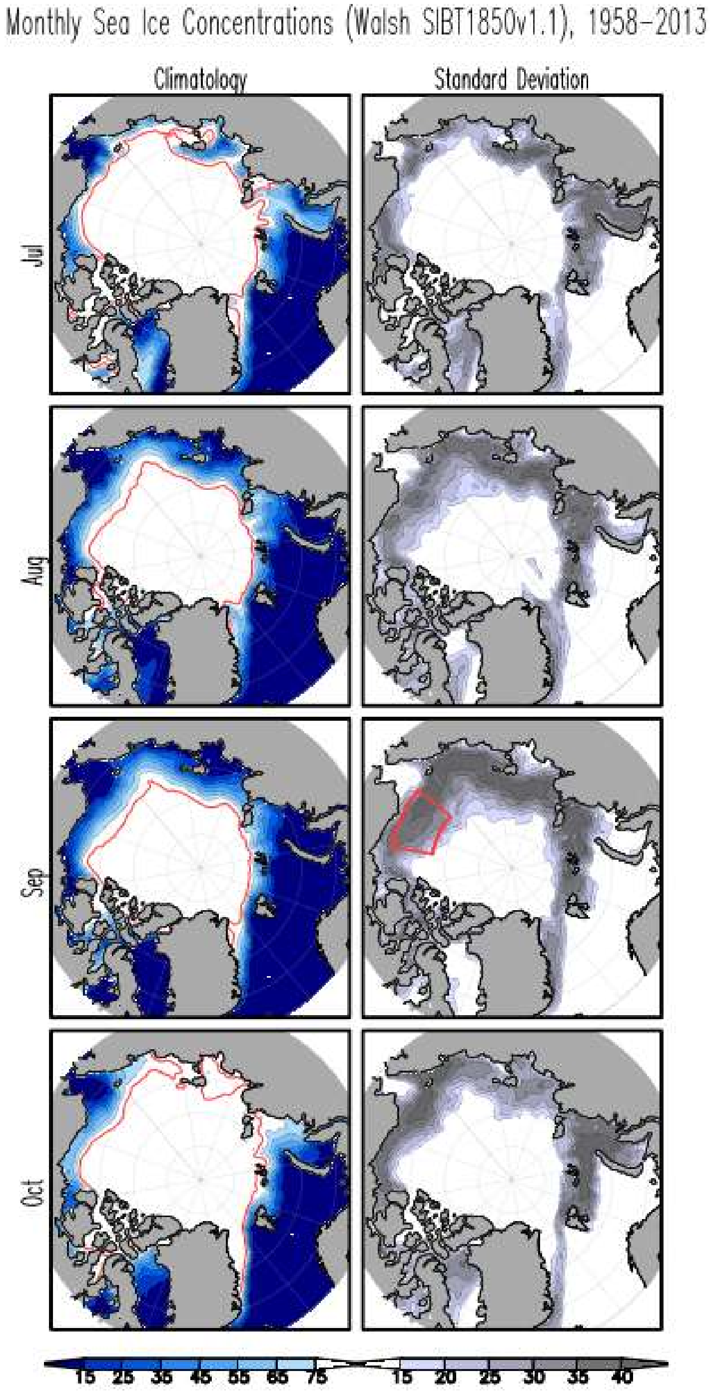

Figure 2.3. Same figure as Figure 2.2, but using SIC from SIBT1850.

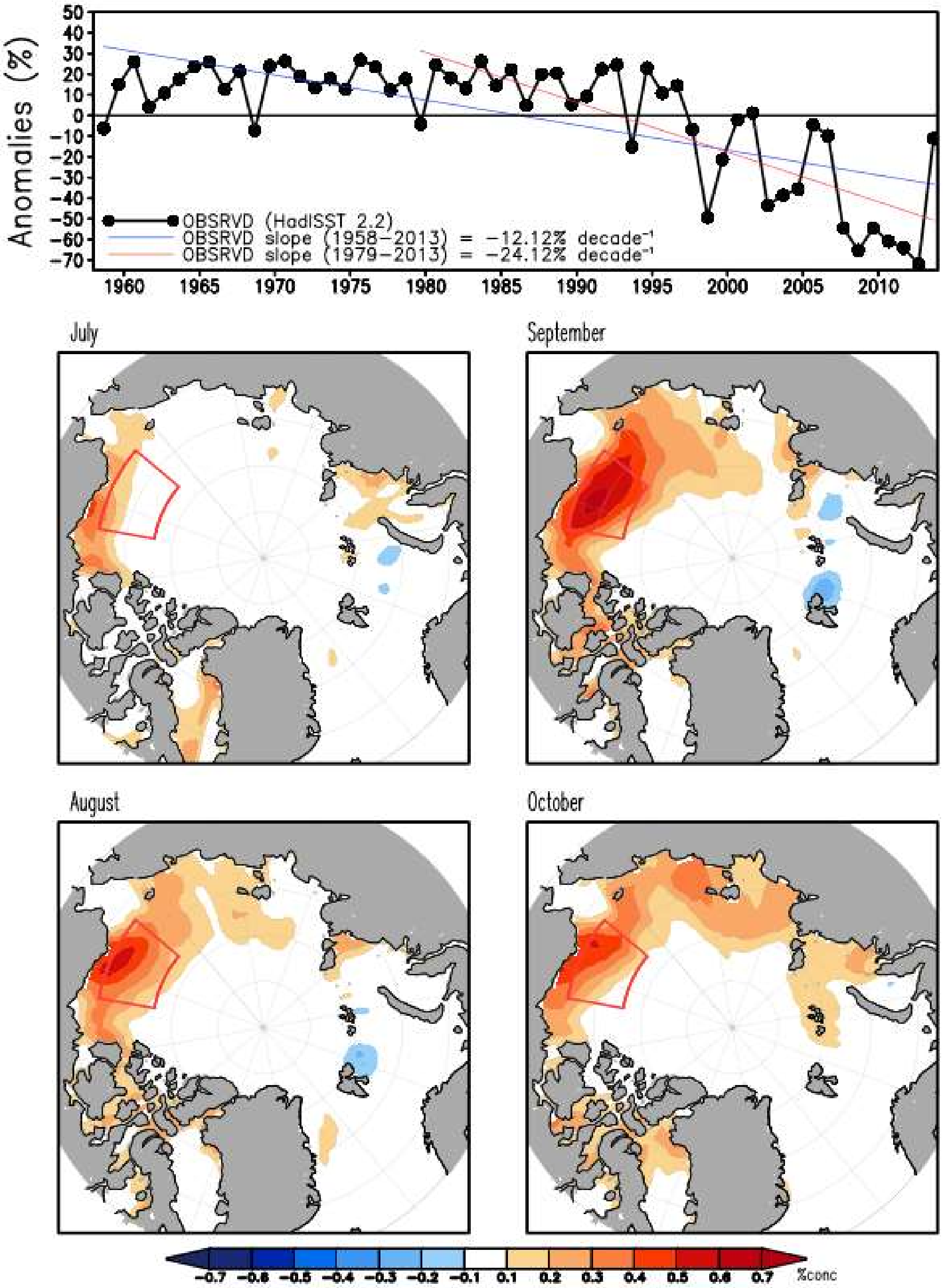

Figure 2.4. (Top) Time series of the area-averaged September SIC anomaly in the BCSA study region (72-78°N, 140-170°W), i.e., the "BCSA index", and corresponding linear trends for the periods 1958-2013 (blue line) and 1979-2013 (red line). (Bottom) Linearly-detrended SIC anomalies regressed on the BCSA index for the period 1958-2013; regressions comprise the previous July and August, contemporaneous September, and subsequent October. The regression plots have been smoothed using the GrADS function smth9. SIC data from HadISST2.2. The box in the maps shows the region of definition of the BCSA index. Orange/blue shading indicates positive/negative SIC anomalies in %.

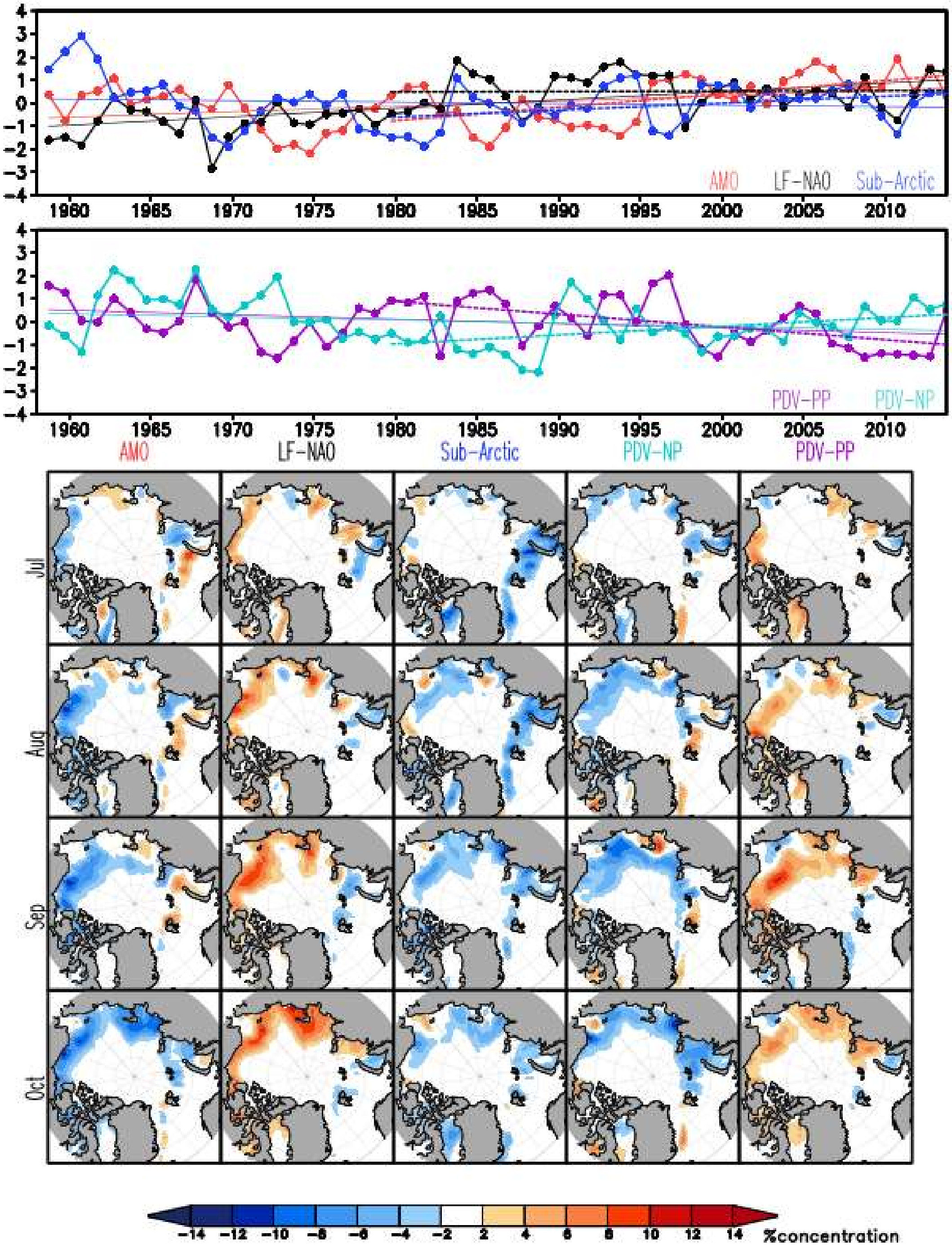

Figure 2.5. (Top) Principal component (PC) time series in fall of Atlantic (AMO, LF-NAO, SADV) and (middle) Pacific (PDV-PP, PDV-NP) modes for the 1958-2013 period. PCs are from Nigam et al. (2020). Linear trend lines for 1958-2013 (thin lines) and 1979-2013 (thick dashed lines) are overlaid on the PCs. (Bottom) Antecedent July and August, simultaneous September, and subsequent October linearly-detrended SIC anomalies for the 1958-2013 period are regressed on the autumn time series. Regression maps were smoothed using the GrADS function smth9. Orange/blue shading indicates positive/negative SIC anomalies in %.

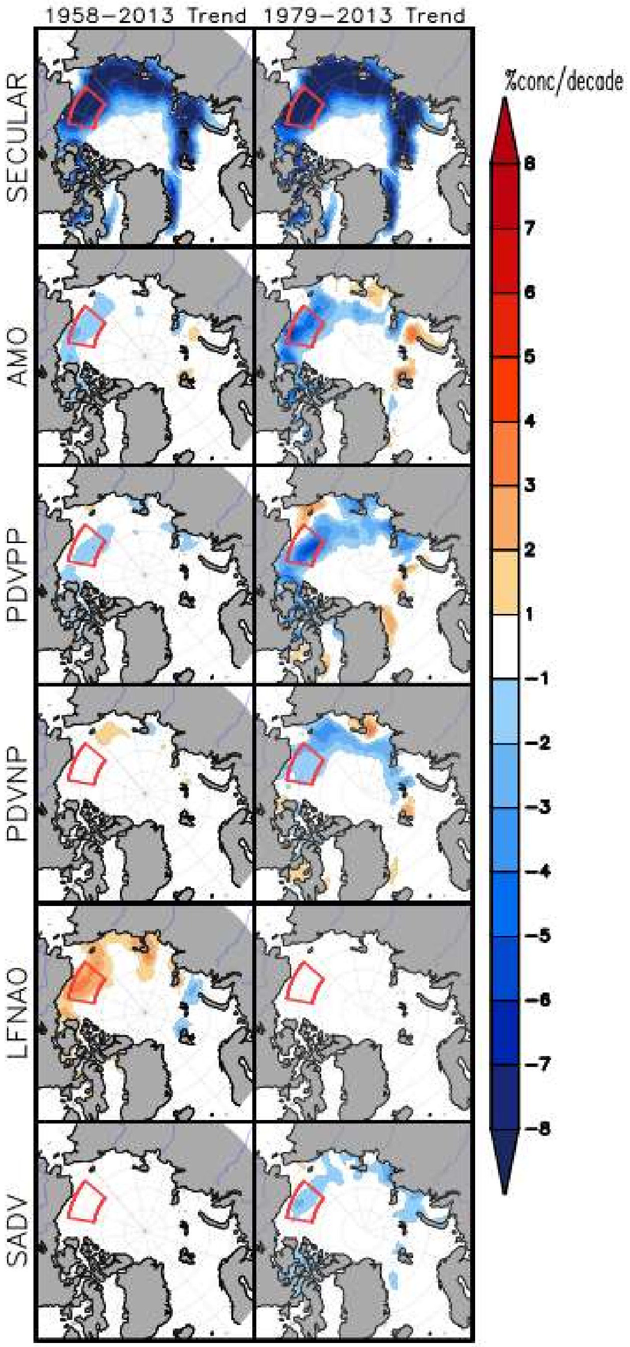

Figure 2.6. (Left) 1958-2013 and (right) 1979-2013 linear trend of reconstructed September SIC (units are % concentration per decade). Reconstructions are calculated for each individual mode (autumn AMO, PDV-NP, PDV-PP, LF-NAO, and SADV) by multiplying each mode's September SIC regressed anomalies by the mode's PC time series. The September SIC data has been linearly detrended prior to the regressions for all modes except for the regression with the secular trend. SIC data from HadISST2.2. Spatial plots have been smoothed using the GrADS function smth9.

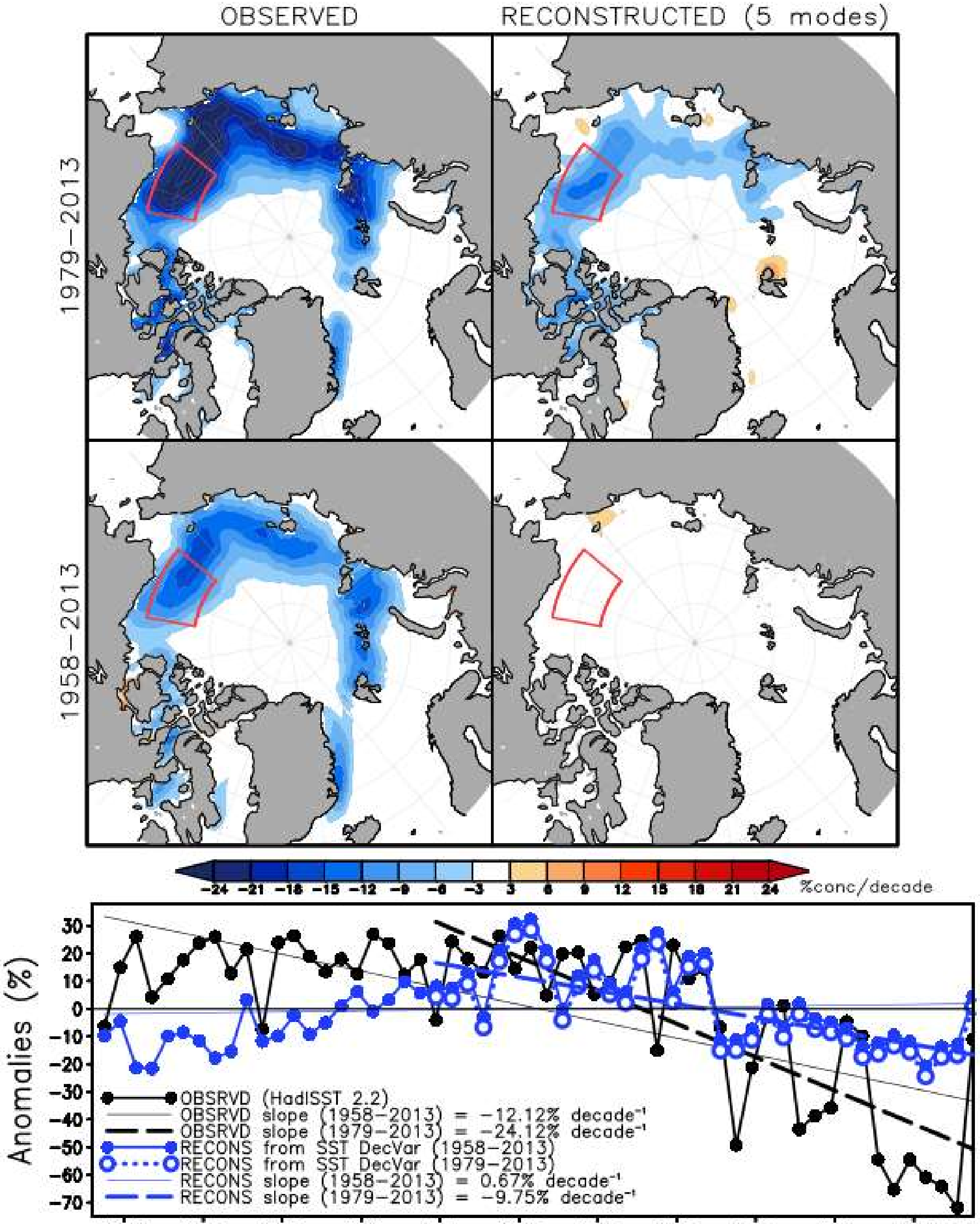

Figure 2.7. (Top) 1979-2013 and (middle) 1958-2013 linear trend of observed (left) and reconstructed (right) September SIC (units are % concentration per decade). The reconstruction is calculated by regressing the linearly-detrended (from 1958-2013) September SIC (HadISST2.2) on each of the autumn AMO, PDV-NP, PDV-PP, LF-NAO, and SADV time series, multiplying the regressed anomalies by the time series, and then summing the five individual reconstructions. Spatial plots have been smoothed using the GrADS function smth9. Orange/blue shading indicates positive/negative SIC linear trends in %/decade (Bottom) Timeseries of observed SIC anomalies (black) and reconstructed (blue) SIC anomalies in the study area.

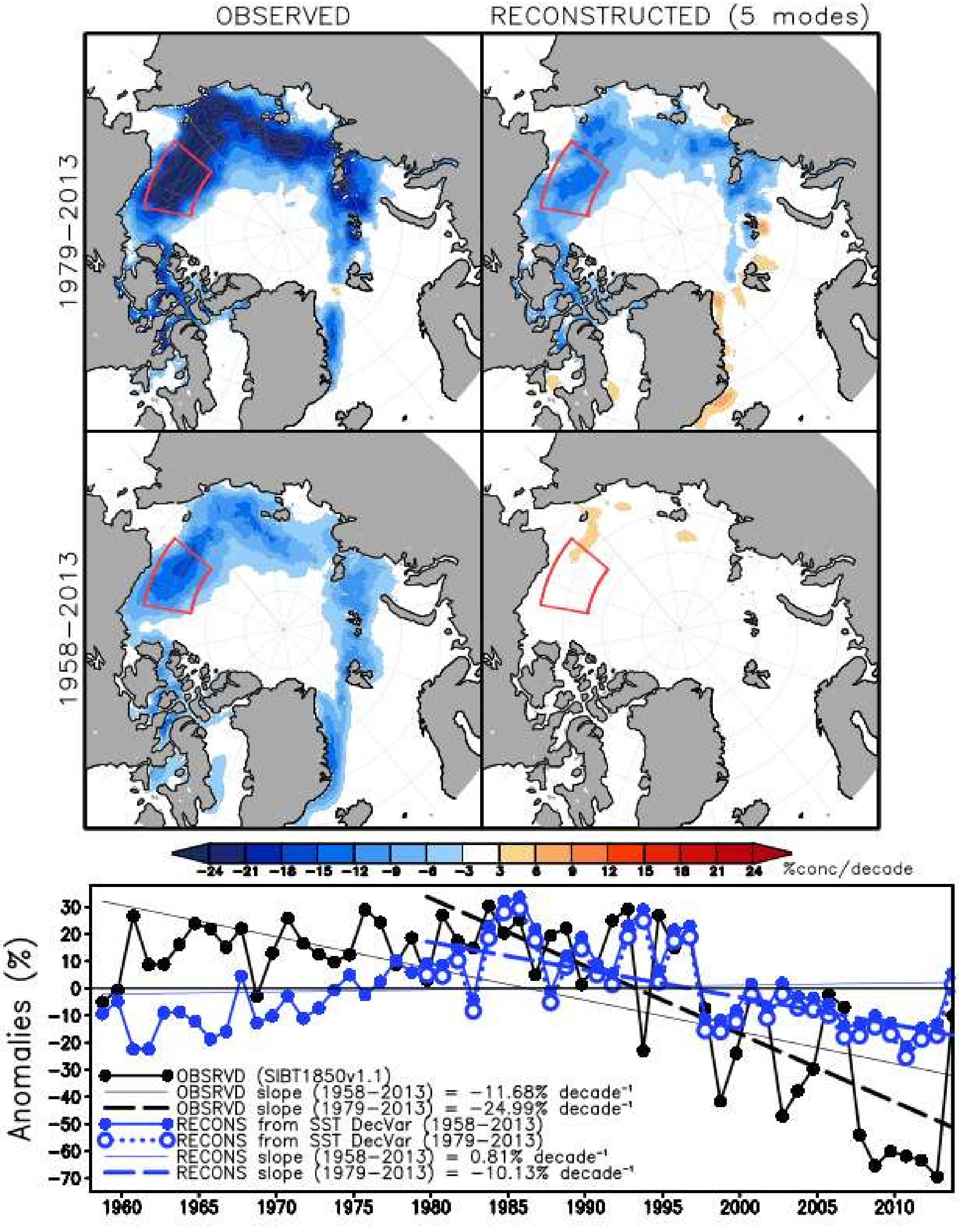

Figure 2.8. Same figure as Figure 2.6, but using SIC data from SIBT1850.

Chapter 3: Multi-decadal Sea Surface Temperature Variability Impacts on the Arctic Atmosphere and Ocean

3.1 Introduction

In Chapter 2, the impact of decadal and multidecadal modes of sea surface temperature (SST) variability on September Arctic sea ice concentration (SIC) was quantified. Five modes of decadal and multidecadal variability, the Atlantic Multidecadal Oscillation (AMO), Pacific Decadal Variability Pan Pacific (PDV-PP) and North Pacific (PDV-NP), a Low-frequency North Atlantic Oscillation (LF-NAO), and a Sub-Arctic decadal variability (SADV) mode, were responsible for about 40% of the total trend of 24.12% decade^{-1} in SIC loss in the Beaufort-Chukchi Seas study area over the 1979 to 2013 time period. The long-term secular trend contributes with a loss of 11.7% decade^{-1}. The AMO and the PDV-PP impose additional losses of 3.84% decade^{-1} and 3.23% decade^{-1}, respectively, while the PDV-NP contributes with a further decline of 1.56% decade^{-1}.

This chapter investigates the impact that the low frequency modes (AMO, PDV-PP, and PDV-NP) have on the ocean, atmosphere and regional hydroclimate in the Arctic in order to establish their pathways to regional sea ice loss or gain. Section 3.2 describes the data sets and analysis techniques used. Section 3.3 discusses the relationship between the continental hydrological cycle and ocean temperature, salinity, and SIC in the Beaufort and Laptev Seas. Section 3.4 describes the climatology of the Arctic atmosphere and ocean. Section 3.5 discusses the impact of the AMO on the Arctic atmosphere and ocean at seasonal and monthly time scales, focusing on the Beaufort Sea and the Laptev Sea. Similarly, Sections 3.6 and 3.7 discuss the impact of the PDV-PP and PDV-NP, respectively, on the Arctic atmosphere and ocean. Section 3.8 discusses the impact of Mackenzie River discharge on the Beaufort Sea at seasonal time scales. Section 3.9 provides a summary.

3.2 Data Sets and Methods

3.2.1 Data Sets

Monthly and seasonal mean sea level pressure (MSLP) fields from the NCEP-NCAR Reanalysis data set (Kalnay et al. 1996) and seasonal mean near-surface air temperature from the CRU TS4.02 data set (Harris et al. 2020) were used to investigate the influence of natural low-frequency variability on the Arctic near-surface atmosphere. Monthly and seasonal ocean temperature, salinity and ocean heat content (OHC) fields from EN 4.2.1 (Good et al. 2013), bias corrected with Levitus WOA09 (Levitus et al. 2009a) were used to investigate the influence on the Arctic Ocean and the marginal seas of the Arctic. Additional details about these atmospheric and oceanic data sets can be found in Section 1.2.1. Monthly and seasonal SIC fields used in this analysis were from the Met Office Hadley Centre's sea ice and sea surface temperature data set version 2.2.0.0 (HadISST2.2); see Section 1.2.2 for additional information about HadISST2.2. Seasonally-averaged fields were calculated as the averages of monthly data for winter (December, January, February), spring (March, April, May), summer (June, July, August), and autumn (September, October, November).

River discharge observations from R-ArcticNET (Lammers et al. 2001) and ArcticGRO (Shiklomanov et al. 2018) were used, along with runoff estimates from the GRUN data set (Ghiggi et al. 2019); additional information about the discharge and runoff data sets can be found in Section 1.2.4. The monthly river discharge data was integrated over a hydrological year from October through the following September to create total annual river discharge time series. Precipitation data from GPCCv8 (Schneider et al. 2018) and the UDEL Terrestrial Precipitation version 5.01 (Matsuura and Willmott 2018a) along with evapotranspiration (ET) data from the UDEL Water Budget Data Archive version 4.01 (Matsuura and Willmott 2018b) were also analyzed; additional details about the GPCCv8 and UDEL data sets can be found in Section 1.2.3.

As in Chapter 2, the 1958-2013 time period was the primary focus of this analysis, except when limited Mackenzie River discharge data necessitated the use of a shorter time period from 1973-2013. The 1958-2013 time period was selected to coincide with the International Geophysical Year (July 1958-December 1958) and represents the time period in which more sea ice observation data are available, but most importantly, this period highlights decadal-to-multidecadal variability.

3.2.2 Climate Modes from an SST-based Analysis

The low-frequency variability modes were obtained from a spatiotemporal (Rotated Extended Empirical Orthogonal Function) analysis of 118 years of observed seasonal SST data from Nigam et al. (2020). Additional information about these modes of variability can be found in Section 2.2.2. For the analysis in this chapter, single season principal component time series of the AMO, PDV-PP and PDV-NP modes were smoothed using a loess filter with an 8-year time window, or 7% of the 118-year SST dataset; the smoothing suppresses seasonal-to-interannual variations, thereby highlighting decadal-to-multidecadal variability.

3.2.3 Regression Analysis Methodology

To investigate the influence of low frequency climate variability on the Arctic, seasonal atmospheric and oceanic fields were regressed on the smoothed principal components. Lead/lag regressions are used to capture antecedent, simultaneous and subsequent anomalous structures in the atmosphere and ocean. The single-season principal component time series for the AMO, PDV-PP, and PDV-NP were smoothed as described above, then linearly-detrended seasonal MSLP and near-surface air temperature were regressed on them. Simultaneous season regressions were calculated for these fields due to the fast-acting nature of the atmosphere. For the more slowly changing ocean fields of seasonal 5-25 m integrated OHC, 5-25 m average salinity, and SIC, they were linearly detrended and then lead/lag regressed on the smoothed summer principal components. These lead/lag regressions were calculated to investigate anomalies leading into sea ice melt season in summer and continuing into the early autumn.

The influence of low frequency climate variability on the Arctic atmosphere and ocean at monthly time scales was also investigated to focus in on the sea ice melt season. For these regression analyses, the linearly-detrended monthly fields of SIC, MSLP, 5-25 m integrated OHC, and 5-25 m average salinity were regressed on the smoothed seasonal time series for the AMO, PDV-PP and PDV-NP. In this case, the monthly atmospheric and oceanic fields in June, July, and August were regressed simultaneously on the smoothed summer principal components while the September fields were regressed on the autumn principal components. Special interest was put into the subsurface temperature and salinity structures along 135°W through the Beaufort Sea (just off the mouth of the Mackenzie River) and from the mouth of the Lena River along 125°E through the Laptev Sea (just off the mouth of the Lena River).

Finally, to investigate links between the continental hydrological cycle and the Arctic Ocean basin, the linearly-detrended seasonal fields of 5-25 m integrated OHC, 5-25 m average salinity, and SIC were regressed on the smoothed annual Mackenzie River discharge anomaly time series. The discharge anomaly time series was smoothed using a loess filter with an 8-year time window to suppress seasonal-to-interannual variations to highlight decadal-to-multidecadal variability. Subsurface temperature and salinity were also regressed on the smoothed annual Mackenzie River discharge anomaly time series.

3.3 Arctic Hydrological Data

3.3.1 Hydrological Climatology

The annual cycles of hydrological fields in the Mackenzie and Lena River basins, calculated as long-term monthly means, are presented to provide a climatological context of the existing relationships of the regional hydroclimate in the Arctic. The annual cycles of monthly basin area-averaged precipitation, evapotranspiration (ET), and runoff for the Mackenzie and Lena River basins were calculated over the 1958-2013 period (Figure 3.1, top row). The area-averaged SIC climatologies for the Beaufort (69°-74°N, 150°-120°W) and Laptev (70°-76°N, 113°-138°E) Seas are shown in the middle and bottom rows of Figure 3.1, along with the 5 m salinity and 5 m ocean temperature climatologies; all were calculated over the 1958-2013 period. The annual cycle of river discharge at the mouths of the six major Arctic rivers, calculated over the 1980-2016 period, is shown in Figure 3.2.

Maximum precipitation in both the Mackenzie and Lena River basins occurs in July and August. The annual cycle of ET follows the cycle of increasing incoming solar radiation in the far north and reaches a peak in June and July as warmer temperatures lead to increased ET. The simultaneous peaks in ET and precipitation reduce the amount of water available for runoff, and the runoff decreases through the summer even though precipitation reaches its annual peak in summer. Maximum runoff in the Mackenzie and Lena River basins occurs in May and June, followed by the peak river discharge near the mouths of the rivers in June (Figure 3.2), followed by decreases in river discharge through the rest of the summer with a return to the low wintertime base flow in November. The different timing of peaks in runoff and precipitation suggest that the runoff, and also discharge, is fed primarily by melt of snow and land ice from the previous winter and spring. During the spring, river ice melt and snow melt from the surrounding terrain floods over sea ice in the western Arctic, and this relatively warm and fresh river discharge initiates sea ice melt and creates open water offshore in the delta region before melting occurs elsewhere along the coast (Dean et al. 1994, Matthews and Stringer 1984). The salinity minimum in the Beaufort and Laptev Seas occurs in June and seems to be in response to the May/June peak runoff and the June peak river discharge, although freshwater from sea ice melt likely also contributes to the summertime reduction in salinity beginning in June when sea ice first begins to melt. Heating of the ocean surface begins in June and reaches a peak in August, suggesting that both warm river water and the summertime reduction in SIC, and subsequent warming of the open water by absorption of solar radiation contribute to surface ocean warming.

While Arctic river discharge across all six major rivers reaches a maximum in June, there is year-to-year variability in river discharge. Figure *3.3* shows the total annual river discharge from the six major rivers using observations from the R-ArcticNET and ArcticGRO data sets. The annual time series have been smoothed with a loess filter with an 8-year time window to suppress seasonal-to-interannual variations to highlight decadal-to-multidecadal variability. While data are available from the Ob, Yenisey, and Lena Rivers starting in the 1930s, data from the Kolyma, Yukon, and Mackenzie Rivers begin in the 1970s.

3.3.2 Arctic River Heat Flux

Searcy et al. (1996) found that the heat supplied by the Mackenzie River to the delta region accounts for half of the energy required to melt the ice and that ice is removed 1-2 weeks ahead of neighboring coastal areas without river discharge. Mulligan and Perrie (2019) looked at the Mackenzie River plume in August 2007 and their analysis found that the advection of river water is the primary source of heat in the coastal region. Yang et al. (2014) found the seasonal (May-October) heat flux from the Mackenzie River to be 10,430 PJ over the 1950-2010 period. Liu et al.

(2005) found the annual heat flux from the Lena River to be 14,281 PJ over the 1950-1992 period.

To estimate the heat flux over the 1958-2016 time period, river temperatures first needed to be estimated. As described in Section 1.2.5, river water temperatures are available for the period from the mid-1930s to 2003 from the ART-Russia data set for the four Russian rivers, from 1960 to 2010 from the Yang data set for the Mackenzie River, and from 2003 to 2018 from ArcticGRO for all of the rivers. While the ART-Russia data set provides average river temperature every 10 days during the warm season, the Yang and ArcticGRO data sets are more sparse, sometimes with just three measurements per year, owing to the difficulty in making field measurements in the Arctic. River water temperature was thus estimated from a linear regression analysis using near-surface air temperature at the grid point in CRU TS version 4.01 nearest to the river temperature measurement location for each river, following the technique by Webb and Walling (1993) and Webb and Nobilis (1997). There are two distinct phases to the relationship between air temperature and river temperature during the warm season: the air temperatures are generally warmer than river temperatures during the rising phase from May through June or July, while the river temperatures are warmer than air temperatures during the falling phase from August to October. This hysteresis was noted by van Vliet et al. (2011) for river sites affected by seasonal snow- and ice-melt runoff or reservoir operations, which causes the inflow of cold snowmelt or deep reservoir water during spring and summer, resulting in a lag in stream temperature response to air temperature (Webb and Nobilis 1994). The study by van Vliet et al. (2011) split the data into two periods from January to June and July to December and calculated regression relations for the two halves separately. For the analysis presented here, the monthly data was likewise split into two groups: June and July in Group 1 and August and September in Group 2 for the Russian rivers and May-July in Group 1 and August-October in Group 2 for the Mackenzie River. During the winter months, measurements of river temperature typically were not made because the rivers were frozen. Modeled river temperatures outside of the months listed above were set equal to 0°C, following the method of Lammers et al. (2007b) in their heat flux calculation.

Monthly heat flux was calculated for each of the rivers from the river discharge and the modeled river temperature data following Lammers et al. (2007b) and Yang et al. (2014) using the equation

$$H_{flux} = 86400 \cdot C_p \cdot \rho \cdot T_{°C} \cdot Q \cdot n$$

Where H_{flux} is the total heat flux in a given month, C_p is the specific heat of river water (4.184 J/ °C g), ρ is the density of river water (1×10^6 g/m^3), $T_{°C}$ is the monthly mean river temperature (°C), Q is the monthly mean discharge (m^3/s), and n is the number of days in the month. As calculated this way, the heat flux is the total accumulated heat flux during the month. The monthly mean and total annual heat flux for the Ob, Yenisey, Lena, Kolyma, and Mackenzie Rivers are listed in Table 3.1. The total annual heat fluxes for the Lena and Mackenzie Rivers compare fairly well with those found, for different time periods, by Yang et al. (2014) and Liu et al. (2005).

The amount of sea ice that could be melted by the annual heat flux from the Lena and Mackenzie Rivers was estimated by assuming all of the energy is applied to the heat of fusion for melting the ice using the equation

$$Q_{rh} = L_f \rho_i A h_i$$

where Q_{rh} is the annual heat flux (J), ρ_i is the sea ice density (kg/m^3), A is the ice area, h_i is the melted ice thickness (m), and L_f is the latent heat of fusion of fresh ice (333.7x10^3 J/kg). The sea ice density was assumed to be 917 kg/m^3, following Park et al. (2020). The total annual heat flux from the Mackenzie River of 10,463 PJ (Table 3.1) could melt a water equivalent of 34 km^3. Assuming an ice thickness of 1 m, this would be equivalent to 3.4x10^4 km^2. The total annual heat flux from the Lena River of 17,271 PJ could melt a water equivalent of 56 km^3. The estimated volume of ice melt due to the Lena River agrees with that estimated by Bauch et al. (2013), who calculated that an average heat flux of about 15,100 PJ would melt 45 km^3.

3.4 Atmospheric and Oceanic Climatology

The anomalous modulation of the surface pressure centers stirs the Arctic waters and sea ice. As mentioned in Chapter 1, climatologically, three main atmospheric features in the Arctic help drive and modulate oceanic features: (1) a broad region of high MSLP that persists from autumn through spring and stretches from North American to Siberia across the frozen Arctic, (2) the Icelandic Low near Iceland and the southern tip of Greenland, and (3) the Aleutian Low in the North Pacific (Figure 1.5). In years with a strong Icelandic Low, and thus strong westerly winds along the Eurasian coast, inflow of Barents Sea water into the Kara Sea increases and water masses are transported from the south to the north in the Laptev Sea along the eastern edge of the Low. This increases the temperature and salinity of the Kara Sea. In years with a stronger Arctic high, and thus anomalous easterly winds along the Eurasian coast, the inflow of Barents Sea water into the Kara Sea decreases and river outflows into the Kara Sea increase (Nikiforov and Shpaikher 1980; Shpaikher et al. 1972).

On the Pacific side of the Arctic, about two-thirds of the Bering Strait throughflow is controlled by the Pacific-Arctic pressure-head (Woodgate et al. 2012), which is in turn influenced by the location and strength of the Aleutian Low, which steers storm paths and changing sea surface height anomalies (Danielson et al. 2014). As shown in the conceptual diagrams in Danielson et al. (2014), a strong Aleutian Low centered over the Bering Sea (i.e., a westward shift) causes the sea surface height to decrease, which lowers the Pacific-Arctic sea surface height gradient and decreases the Bering Strait throughflow at inter-annual timescales. However, the westward shift in the Aleutian Low also creates southeasterly or southerly winds over the Bering Shelf, driving coastal convergence along western Alaska and increased northward currents through Bering Strait on synoptic timescales. Under an Aleutian Low shifted eastward into the Gulf of Alaska, sea surface heights in the Aleutian Basin increase, which increases flow through the Bering Strait (Danielson et al. 2014). Sea surface height in the southwestern Chukchi Sea and the East Siberian Sea is also strongly correlated with Bering Strait Throughflow (Kawai et al. 2018). Anomalous easterlies in the East Siberian and Laptev Seas cause offshore Ekman transport and decreased sea surface height.

Variability of sea ice along the marginal seas in the Arctic Ocean is large during the warm season. In the winter and spring, most of the Arctic Ocean and its marginal seas are ice covered, with the sea ice extent extending south of Bering Strait and roughly to Svalbard in the North Atlantic (Figure 1.4). In the summer and autumn, however, the climatological SIC is reduced near the coasts. Such regions, that correspond to the marginal seas of the Arctic, are in fact sensitive to year-to-year variability as the standard deviation of the monthly SIC shows; coincidentally, those regions correspond to the marginal seas that surround the Arctic Ocean.

Several studies have looked at the surface current systems in the Arctic to better understand freshwater transport. Climatologically, the freshest water in the Arctic is located near the mouth of the rivers, and it is the most pronounced at the mouth of the Lena and Kolyma Rivers (Figure 1.13). The anticyclonic Beaufort Gyre, driven by the Beaufort High, and a cyclonic circulation (actually an eastward extension of the Low that the Icelandic Low is part of) in the Siberian Arctic converge and form the Transpolar Drift Stream (TDS). The TDS moves ice and fresh, surface water across the Arctic toward the Fram Strait (Rudels et al. 2012), as seen in the plume of freshwater extending north of the Kolyma River mouth in Figure 1.13. River freshwater entering the Arctic is either concentrated near the coasts downstream of rivers as plumes extending across the shelves or as narrow (1-20 km), shallow (10-20 m), surface-trapped buoyancy boundary currents, termed the Riverine Coastal Domain by Carmack et al. (2015). The local response of river water forming into plumes or boundary currents is determined by volume discharge, bathymetry, shelf width and slope, and winds (Weingartner et al. 1999; Bacon et al. 2002, 2014;

Carmack et al. 2016). Typically, the Riverine Coastal Domain pathway is expected to move water from the west to the east along the Arctic coastline (Carmack et al. 2015).

The Arctic Ocean subsurface climatology at and north of the mouths of the Mackenzie River, in the Beaufort Sea, and the Lena River, in the Laptev Sea, are shown in Figure 3.4 and Figure 3.5, respectively. Monthly climatological vertical profiles of ocean temperature and salinity along 135°W extending north from the Mackenzie River are shown in Figure 3.4. During the summer months, a thin layer of above freezing, fresh water extends north from the Mackenzie delta. This layer, about 15 m deep, has water temperatures up to 3°C and salinities of 22. The timing of this relatively warm, fresh water layer coincides with the months when the Mackenzie River is not iced over and river discharge is high. Climatologically speaking, the Mackenzie River has peak discharge in June with decreasing amounts of discharge through October, before returning to the relatively constant low wintertime flow (Figure 3.2, black line). It also coincides with the time period when sea ice has climatologically melted near the coast and retreated from the coastline, which allows for solar warming of the near-surface waters and provides additional freshwater from sea ice melt to the near-surface layer. The open waters also increase wind-driven vertical mixing, which help to mix the warm waters to deeper depths, as shown in Figure 3.4 with the depth of the 0°C waters increasing from June through September, and also leads to dissipation of the freshwater through the ocean column. It should be noted that the cold waters seen at ~30 m depths in winter and early spring propagated from the north in the early summer. On the other hand, the warm and fresh waters in the southern part (70°-78°N) between the surface and ~30 m depth seen in winter and early spring, are remnants of the summer dumping of warm and fresh waters from the Mackenzie River.

Monthly climatological vertical profiles of ocean temperature and salinity along 125°E extending north from the Lena River are shown in Figure 3.5. In the Laptev Sea, a thin layer of above freezing, fresh water extends north from the Lena delta throughout the year. Like the Beaufort Sea, this layer is about 15 m deep. The warmest water temperatures, up to 2°C, occur in the summer and autumn. Salinities in the top layer are about 21. The timing of the warmest water temperatures coincides with peak Lena River discharge and the time period when sea ice has climatologically melted near the coast and retreated from the coastline, allowing for solar heating of the near-surface waters.

During anticyclonic regimes such as during the low Arctic Oscillation (AO) pattern, the Beaufort High expands westward across the Chukchi Sea and the TDS source also shifts west toward the Laptev Sea. Freshwater from the Chukchi and East Siberian shelves flows westward to meet eastward flowing freshwater from the Kara and Laptev Seas, which are then transported into the central Arctic by the TDS and out of the Arctic through Fram Strait (Maslowski et al. 2001; Morison et al. 2012). During cyclonic surface ocean circulation regimes, such as during the high AO index pattern which includes cyclonic motion on the Siberian shelf and a southeastward retreat of the Beaufort High into the Canada Basin, Eurasian river runoff is diverted along the coast toward the Laptev and East Siberian Seas into the Canada Basin and into the Beaufort Gyre (e.g., Maslowski et al. 2000, 2001; Morison et al. 2012). Along the coasts, Osadchiev et al. (2020) documented, through satellite imagery and oceanographic surveys, the spread of river plumes between the Kara, Laptev, and East Siberian Seas and the influence of wind forcing on the eastward spread of these plumes.

The seasonal climatology of near-surface air temperature over land was shown in Figure 1.9. Seasonal average temperatures in northern North America are about -20°C in winter, warming to 5-10°C in summer, with temperatures in the ±5°C range in spring and autumn. Average temperatures in eastern Siberia are much cooler than in western Siberia, for all seasons. In the winter, climatological temperatures range from -15°C in western Siberia to -40°C in parts of eastern Siberia. Average summer temperatures range from 15°C in western Siberia to 5-10°C in eastern Siberia. In spring and autumn, temperatures are ±5°C in western Siberia, and -5 to -10°C in eastern Siberia.

Based on the previous analysis of the climatological conditions and the knowledge that anomalous variations of the regional pressure systems have an impact on water mass movement in the Arctic, we now turn to investigating how low-frequency modes of natural variability, through their impact on the atmospheric circulation patterns, influence the distribution of heat, freshwater, and sea ice in the Arctic.

3.5 Arctic Atmospheric and Oceanic Anomalies due to the AMO

3.5.1 Seasonal-Scale Beaufort and Chukchi Seas Anomalies

During a positive phase AMO, an anomalous high also forms over the North Pacific in spring, shifting the Aleutian Low to the west (Figure 3.6). This anomalous circulation pattern would generate southwesterly winds in the Bering Sea and southerly winds in the Bering Strait, increasing the Pacific water inflow through the Bering Strait (Figure 3.8). In summer, the AMO leads to anomalous low MSLP that extends from western Canada to Asia. This anomalous circulation, coupled with the increased high pressure over the central Arctic, would cause anomalous easterly winds over the Beaufort and Chukchi Seas region in summer and autumn, and lead to Ekman transport of surface water away from the coast and increased inflow through Bering Strait. Indication of increased warmer water inflow through the Bering Strait is found in the positive OHC anomalies in the Beaufort Sea.

Along with the anomalous high MSLP in spring, the positive phase AMO leads to anomalously cold temperatures over western Canada, delaying the melt of snow and ice over land (Figure 3.7). In summer, and even more pronounced in autumn, the AMO leads to warmer near-surface air temperatures. This could lead to the advection of anomalously warm air temperatures over the Beaufort Sea, reinforcing fog and low-level cloud formation which increases longwave radiation to the surface. Increased warming of the surface leads to increased sea ice melt and delays sea ice freeze-up in autumn. The increased freshwater due to sea ice melt water may be one source of the negative near-surface salinity anomaly in the region of the Beaufort Gyre (Figure 3.9) during the positive phase of the AMO. This feature exists in all seasons. An additional cause of the freshwater anomaly may be increased river runoff from the Mackenzie River that is slowly moved westward by the anomalous easterly winds over the Beaufort Sea instead of its typical pathway eastward through the Canadian Arctic Archipelago.

The anomalous easterlies over the Beaufort Sea in summer and autumn due to the increased gradient between the high MSLP anomaly in the central Arctic and the low MSLP anomaly over western North America also lead to ice in the Beaufort and Chukchi Seas moving to the north and away from the coast due to Ekman transport to the right of the winds. This ice drift away from the Beaufort and Chukchi, combined with the positive OHC anomaly and increased near-surface air temperatures, sets the stage for increase sea ice melt, delayed sea ice refreeze, and the reduction of SIC in the Beaufort and Chukchi Seas (Figure 3.10). This was also discussed in Chapter 2, where it was discovered that the positive phase of the AMO results in a region of negative SIC anomalies in the Beaufort and Chukchi Seas in summer, which increases in extent in autumn to impact all of the marginal seas.

3.5.2 Monthly-Scale Beaufort Sea Anomalies

Focusing in on the sea ice melt season from June to September, Figure 3.11 shows the regressed anomalies of the AMO on monthly SIC and MSLP. During the positive phase AMO in the Beaufort Sea, a small region of negative SIC appears in June just north of the Mackenzie River delta. A high MSLP anomaly extends from North America into the central Arctic. The anticyclonic circulation around the high, with Ekman transport to the right of the mean flow, acts to move ice away from the North American coast. In July, anomalous low pressure forms, centered over the coast and southern Beaufort Sea. This causes anomalous easterly winds in the Beaufort Sea and northerly ice drift due to Ekman transport. This ice motion northward away from the coast is enhanced in August as the anomalous high over the central Arctic strengthens. The anomalous high shifts southward in September toward the Beaufort Sea, enhancing the Beaufort Gyre and continuing to move ice away from the coast.

Regressed anomalies of 5-25 m integrated OHC are shown in Figure 3.12. During the positive phase of the AMO, there is a positive OHC anomaly in the Bering Sea in June, which spreads into the Chukchi and Beaufort Seas in July and August before losing strength in September. This warm OHC anomaly coincides with an area of reduced SIC. The center of the OHC anomaly remains west of the Mackenzie River delta, possibly due to the anomalous easterly winds in the Beaufort Sea moving relatively warm Mackenzie River outflow to the west, where it converges with Pacific inflow and is entrained into the Beaufort Gyre. The 5-25 m layer averaged salinity regressed anomalies are shown in Figure 3.13. A freshwater anomaly persists through the melt season and is the most extensive and strongest in July. This anomaly is slightly centered north of the mouth of the Mackenzie River. The position of the anomaly and its peak in July suggests a link to the fresh water outflow from the Mackenzie, which exhibits peak discharge in June (Figure 3.2, black line), rather than being driven by sea ice melt water, which would presumably peak in September, coinciding with the annual sea ice minimum and open water maximum.

To investigate the structure of the anomalies in the subsurface Beaufort Sea, the vertical profiles of the monthly mean ocean temperature and salinity were regressed on the AMO PC time series (Figure 3.14). During the positive phase AMO, there is a region of anomalously warm, fresh ocean waters at depth of about 10 to 90 m. The progression of this warm, fresh water anomaly begins in June, with a warm water anomaly near the coast at 15 m depth over the Beaufort shelf and a second anomaly centered at about 75°N and 50 m depth over the Canada Basin. The coastally-linked warm anomaly continues through September. In November, the region of peak anomalous warming has detached from the coast. This warm anomaly then descends through the winter and spring, forming the persistent warm anomaly at 50 m depth. This warm anomaly contains waters about 0.12°C warmer than the climatological -1.6°C waters, or about 10% warmer. The salinity anomaly also exhibits an annual progression as it mixes to deeper depths in the summer. The climatological salinity is about 29 to 30 and the freshwater anomaly reduces the salinity by about 0.2 to 0.5. This persistent warm, freshwater anomaly, circulating in the Beaufort Gyre, allows for easier sea ice melt in the spring.

In addition to the layer of anomalously warm waters, the top 10 m of the ocean in July and August are anomalously cool during the positive phase of the AMO, which could indicate a reduction in warm Mackenzie River discharge and/or increased cooling of the surface ocean waters through loss of heat to the atmosphere due to the anomalous reduction in SIC (Figure 3.11 and Figure 3.14). This anomalous cool upper-ocean layer is also present in November and January. Anomalies at the surface should be considered with caution, however. While the EN4.2.1 data set provides temperature and salinity data at 5 m depth, many of the observed profiles that were used to build the data set had their uppermost measurement at 10 m depth. For example, SBE-16 Seacat CTD used on the Polar Ocean Profile Buoy had sensors at 10, 40, 70, 120, 200, and 300m; and the Japan Marine Science and Technology Center (JAMSTEC) Compact Arctic Drifters (J-CAD) deployed in the Arctic since 2000 have conductivity and temperature sensors typically attached at 25, 50, 80, and 180 m (Boyer et al. 2013). While there may be plausible physical interpretations of the anomalies, they might also be a consequence of a representation of the top layer of the ocean that may not be as well-sampled as greater depths.

3.5.3 Seasonal-Scale Siberian Seas Anomalies

In the winter, the AMO generates an anomalous high over the North Atlantic and Barents Sea, reducing the strength of the Icelandic Low (Figure 3.6). This anomalous high persists through the other seasons over Greenland and the central Arctic Ocean, deepening the climatological high over the central Arctic. The anticyclonic flow associated with the anomalous high pressure over the central Arctic causes anomalous easterly winds along the Siberian coast that impede the typical west to east movement of water masses. This anomalous anticyclonic circulation pattern also limits inflow from the Barents Sea, as evidenced by the negative OHC anomaly in the Barents and Kara Sea (Figure 3.8) due to the reduction of relatively warm Atlantic waters that typically flow into the region. While the AMO leads to increased OHC in the North Atlantic from south of Greenland and Iceland northward to the Greenland Sea, this anomaly does not continue into the Barents Sea and instead there are cold OHC anomalies in the Barents and Kara Seas. This reduction in the transport of warm North Atlantic waters may be leading to the positive SIC anomaly along the ice edge in the Barents Sea in winter to summer (Figure 3.10). The region of anomalous freshwater in the Kara Sea that extends northward from the coast may be a consequence of the anomalous high: anomalous easterly winds associated with the anomalous high may be leading to a disruption of the eastward current through the

Vilkitsky Strait, which would normally transport fresh Ob-Yenisey plume water from the Kara Sea into the Laptev Sea. Instead, the anomalous high and anomalous easterly winds steer the river plume from the Ob and Yenisey Rivers to the north into the core of the Kara Sea and toward the central Arctic (Nikiforov and Shpaikher 1980; Shpaikher et al. 1972). This increases the freshwater in the Kara Sea, while also inducing a positive salinity anomaly in the western Laptev Sea due to the reduction of freshwater transport into that region.

Anomalously cooler near-surface air temperatures in Scandinavia and western Russia in winter and spring (Figure 3.7) coincide with a low MSLP anomaly, suggesting the cold anomaly is due to cold air advection in the deeper trough over that region. However, in the region of the major Siberian rivers, the imprint of the AMO on near-surface air temperatures is weak in winter. In spring, the AMO leads to warmer temperatures in the southern Ob and Yenisey River basins, cooler temperatures in the Lena River basin, and warmer temperatures in the Kolyma River basin. In summer, there are warmer temperatures in the southern Ob and Yenisey River basins and slightly warmer temperatures in the Lena and Kolyma River basins. In autumn, the AMO leads to anomalously warm temperatures over western Eurasia, west of the Ob River, and along the northern Siberian coast. These warm air temperature anomalies could lead to the advection of anomalous warm air over the marginal seas, reinforcing fog and low-level cloud formation and increasing longwave radiation to the surface, melting sea ice and leading to surface ocean warming by solar radiation. They may also lead to warmer river water temperatures, potentially increasing the heat flux into the Kara, Laptev, and East Siberian Seas.

In addition to redistributing the near-surface OHC and salinity, the anomalous high pressure over the Arctic also leads to sea ice moving away from the coast and sea ice convergence in the central Arctic due to Ekman drift of the surface waters to the right of the mean wind flow. The SIC anomalies reflect this, with general reduction in SIC in the Kara Sea and portions of the Laptev Sea in summer followed by circumpolar SIC reductions in autumn. The positive SIC anomaly in the Barents Sea may be due to the reduction of warm North Atlantic water which delays or slows melt of ice along the edge adjacent to the North Atlantic inflow.

3.5.4 Monthly-Scale Laptev Sea Anomalies

Focusing in on the sea ice melt season from June to September, Figure 3.11 shows the regressed anomalies of the AMO on monthly SIC and MSLP. A positive SIC anomaly forms north of the mouth of the Lena River in July during the positive phase AMO and persists through September. The broad negative SIC anomaly that rings the Arctic is further to the north. Climatologically, ocean surface temperatures are at or above freezing throughout the year and the salinity is low (Figure 3.5). During the positive phase AMO, a positive OHC anomaly forms in the Laptev Sea in June, reaches maximum values in August, and disappears in November (Figure 3.12 and Figure 3.17). A positive salinity anomaly in the Laptev Sea of about 0.5 persists throughout the year (Figure 3.13 and Figure 3.17). This positive anomaly could come from a combination of sources, including the anomalous high pressure in August over the central Arctic generating anomalous easterly winds along the Siberian coast that oppose the flow of freshwater entering the Laptev Sea from the Kara Sea and a reduction in the available river discharge from the Lena River.

3.6 Arctic Atmospheric and Oceanic Anomalies due to the PDV-PP

3.6.1 Seasonal-Scale Beaufort and Chukchi Seas Anomalies

The positive phase of the PDV-PP in winter and spring deepens the climatological Aleutian Low in the North Pacific while also causing a persistent positive MSLP anomaly across North America (Figure 3.6), leading to stronger easterly or southeasterly winds in the Bering Sea, which lead to coastal convergence and downwelling. Ekman transport to the right increases northward flow through the Bering Strait, as evidenced by the positive OHC anomalies in the Bering Sea and extending through the Bering Strait into the Chukchi Sea in winter and spring (Figure 3.8). The increased Pacific inflow is also seen as a negative salinity anomaly in the far western Chukchi Sea and far eastern East Siberian Sea (Figure 3.9). While the PDV-PP leads to positive near-surface air temperature anomalies of about 0.3°C over the Mackenzie River basin, the air temperature is still well below freezing (Figure 3.7). The springtime basin-averaged 1958-2013 near-surface air temperature over the Mackenzie River basin is -3.3°C; a temperature anomaly of +0.3°C would result in temperatures of about -3°C. A negative SIC anomaly appears in the Bering Strait and Chukchi Sea in spring (Figure 3.10), suggesting a connection between the positive OHC anomaly and early sea ice melt.

In the summer and autumn, the negative SIC anomaly spreads through the southern Chukchi Sea, as the continued positive OHC anomaly in the southern Chukchi Sea seems to contribute to the reduced SIC. While the southern Chukchi Sea has reduced SIC, the Beaufort Sea and northern Chukchi Sea experience a positive SIC anomaly. During the summer, the positive MSLP anomaly remains over

Alaska and northwest Canada, with a low MSLP anomaly over the central Arctic, generating anomalous westerly winds in the Beaufort Sea and Ekman transport toward the coast. This would cause onshore convergence that would push ice toward the coast and toward the Canadian Arctic Archipelago, and indeed in summer, the far eastern Beaufort Sea has the highest SIC anomaly. This increased ice cover also helps explain the negative OHC anomaly in the Beaufort Sea, as increased ice cover would reduce the amount of near-surface ocean warming by incoming radiation. There is also a positive salinity anomaly in the Beaufort Sea in spring and summer, which drifts north away from the coast in autumn and winter. This may be indicative of the buildup of salinity due to salt rejection during sea ice formation.

In many ways, the summer positive phase of the PDV-PP results in the opposite impacts on the Beaufort Sea as did the positive phase of the AMO: a weakening of the Beaufort High, increased SIC, and cold and more saline ocean water anomalies. This suggests that when both the AMO and PDV-PP are both in the positive phase, or both in the negative phase, their influence on SIC in the Beaufort Sea might balance each other out. However, as discussed in Chapter 2, the AMO has been trending toward the positive phase in the 2000s while the PDV-PP has been trending toward the negative phase. The negative phase PDV-PP would have the opposite impacts on OHC, salinity, and SIC than those shown in the figures here. The positive phase AMO and negative PDV-PP would work in concert to cause large decreases to SIC in the Beaufort and Chukchi Seas.

3.6.2 Monthly-Scale Beaufort Sea Anomalies

Focusing on the summer sea ice melt season, anomalous low pressure forms over the Beaufort Sea in June and persists through September, which leads to ice divergence and drives anomalous westerly winds that would lead to piling of ice against the Alaskan coastline (Figure 3.11). There is a positive SIC anomaly around the periphery of the anomalous low that eventually stretches from the Canadian Arctic Archipelago to the northern Chukchi Sea in September.

Corresponding to the region of increased sea ice cover, the near-surface (5-25 m) ocean temperature is anomalously cool in the southern Beaufort Sea. This anomaly starts near the mouth of the Mackenzie River in June before spreading westward through the summer months (Figure 3.12), much like the westward progression of the positive SIC anomaly, suggesting the cold anomaly is caused by a combination of reduced warm Mackenzie River discharge and the reduction of open water and reduced solar heating of the near-surface ocean due to the increased ice cover. There is also a positive salinity anomaly located in the Beaufort Sea with the strongest anomalies at and directly north of the Mackenzie River delta (Figure 3.13) from June through August, before drifting northwest in September. These more saline waters could be attributed to increased salt rejection due to increased ice formation in the Beaufort Sea. Because the salinity anomaly remains longitudinally stationary while the OHC anomaly moves to the west, another possible cause of the anomaly may be a reduction of freshwater discharge from the Mackenzie River.

To further investigate the link between the Mackenzie River discharge and the temperature and salinity structure of the Beaufort Sea, regressions of the temperature and salinity vertical profiles on the PDV-PP time series in the Beaufort Sea north of the Mackenzie River delta are shown in Figure 3.15. During the summer months, anomalously cold and more saline waters extend from the coast northward. The cold temperature anomaly is adjacent to the coast from July through September, while the positive salinity anomaly is adjacent to the coast in June and July. This timing corresponds to the climatological peak of Mackenzie River discharge in June (Figure 3.2, black line). The regression anomaly plots suggest that the positive phase PDV-PP reduces the discharge of warm, freshwater from the Mackenzie River. While the surface-based salinity anomaly drifts north starting in August, the temperature anomaly remains adjacent to the coast throughout the year. In a typical summer, the southern Beaufort Sea is not ice-covered, and the near-surface ocean warms. However, the increased ice cover associated with the positive phase PDV-PP limits the typical warming of the southern Beaufort Sea and results in the strongly negative ocean temperature anomaly in that region.

3.6.3 Seasonal-Scale Siberian Seas Anomalies

On the Eurasian side of the Arctic in winter, the positive phase PDV-PP leads to increased MSLP in the central Arctic and near Iceland and reduced MSLP along the Asian coast (Figure 3.6), along with warmer winter temperatures in Siberia (Figure 3.7). The weakening of the Icelandic Low results in weaker inflow of North Atlantic waters into the Arctic, seen as a negative OHC anomaly in the far North Atlantic and the Barents Sea in Figure 3.8. In the summer, the PDV-PP causes a positive MSLP anomaly along the Eurasian coastline and negative MSLP anomalies over Greenland and the central Arctic. This pattern would generate anomalous westerly winds in the northern Barents, Kara, and Laptev Seas, and Ekman transport to the right would cause ice drift to the south toward the coasts and result in the positive SIC anomalies in much of the Siberian seas in summer and autumn (Figure 3.10). At the same time, this anomalous circulation pattern also acts to oppose ice export in the Transpolar Drift Stream, potentially causing the decrease in sea ice concentration south of Fram Strait in the Greenland Sea.

3.6.4 Monthly-Scale Laptev Sea Anomalies

There is anomalously high MSLP over the Laptev Sea during the summer months along with increased SIC (Figure 3.11). There are weak positive OHC and salinity anomalies focused in the western Laptev Sea (Figure 3.12 and Figure 3.13), peaking in September. The monthly climatology of ocean temperature and salinity at the mouth of the Lena River, indicate that the Laptev Sea typically has near-surface temperatures near the coast reaching 3°C from July through September, with freshwater near the surface throughout the year (Figure 3.5). Regressions of the temperature and salinity vertical profiles on the PDV-PP time series (Figure 3.18) show the positive OHC anomaly begins to form at the surface in July and spreads northward and strengthens through September. During the winter, this warm anomaly is capped with a strong negative OHC anomaly at the surface. Likewise, the positive salinity anomaly begins in July, strengthens through September, and slowly decays through the winter. Lena River discharge peaks in June (Figure 3.2, blue line) just prior to the appearance of the temperature and salinity anomalies in the upper layers of the Laptev Sea in July; this timing suggests a connection between river discharge and the anomalies. The positive salinity anomaly during the positive phase

PDV-PP suggests that there is less freshwater entering the Laptev Sea from the Lena River, which results in the positive anomaly when compared to climatology. The positive temperature anomalies suggest that the river water that does enter the Laptev Sea is much warmer than normal.

3.7 Arctic Atmospheric and Oceanic Anomalies due to the PDV-NP

3.7.1 Seasonal-Scale Beaufort and Chukchi Seas Anomalies

The positive phase PDV-NP leads to a weakening of the Aleutian Low in winter and spring (Figure 3.6), with the Aleutian Low shifting far to the west in spring. It also leads to cooler autumn, winter, and spring temperatures over North America (Figure 3.7). During the spring, a region of anomalous low MSLP forms over the East Siberian Sea weakening the climatological high MSLP that extends from North America into Siberia. The springtime circulation would cause anomalous southwesterly winds over the Bering Sea, potentially explaining the positive OHC anomaly in the Bering Sea and Chukchi Sea in spring and summer (Figure 3.8).

This anomalous low persists, although weaker, into the summer and autumn. This may act to slightly weaken the Beaufort Gyre. The MSLP anomaly is accompanied by a positive near-surface air temperature anomaly in summer over the Mackenzie River basin (Figure 3.7). These warm air temperature anomalies could lead to the advection of anomalous warm air over the Beaufort Sea, reinforcing fog and low-level cloud formation and increasing longwave radiation to the surface. This increases ice melt and leads to absorption of solar radiation by the open water. Warm air temperature anomalies over the Mackenzie River basin may also lead to warmer river water temperatures, potentially increasing the heat flux into the Beaufort Sea and the positive OHC anomaly in the Beaufort Sea in summer and autumn. There is also a negative salinity anomaly just west of the Mackenzie River delta throughout the year that peaks in the summer. The Beaufort and Chukchi Seas also experience a negative SIC anomaly during a positive phase PDV-NP (Figure 3.10). The anomaly is weak in the Beaufort Sea, but peaks in the East Siberian and Chukchi Seas. The warm OHC anomaly in the Beaufort Sea could be contributing to this anomalous sea ice loss, which in turn provides increased freshwater from sea ice melt to form the negative salinity anomaly.

3.7.2 Monthly-Scale Beaufort Sea Anomalies

Regressions of the monthly MSLP and SIC on the PDV-NP in summer show a strongly negative MSLP anomaly in July over the central Arctic (Figure 3.11). The negative SIC anomaly begins along the Beaufort Sea coast in July, coinciding with a region of positive OHC and negative salinity anomalies in June (Figure 3.12 and Figure 3.13). This warm OHC anomaly originates at the mouth of the Mackenzie River, suggesting a link between warm outflow from the river and the anomalous SIC loss at the coast early in the summer. The OHC and salinity anomalies in the Beaufort Sea extend north from the Mackenzie River delta in July and drift to the north through August and September, possibly in response to the retreat of the low MSLP anomalies from the central Arctic toward land, which would cause anomalous easterly winds over the Beaufort Sea. In September, the central Arctic is dominated by a positive MSLP anomaly, leading to sea ice convergence toward the central

Arctic, reducing the SIC in the marginal seas and leading to the maximum spatial extent of the negative SIC anomaly.

Looking specifically at the region north of the Mackenzie River delta, surface-based positive ocean temperature and negative salinity anomalies form adjacent to the coast in June (Figure 3.16), coinciding with the June peak discharge from the Mackenzie River. The June temperature profile regression anomaly plot also shows a second peak, centered at about 75°N at a depth of about 50 m. This may be showing the buildup of the positive temperature anomalies from previous years, which have descended and drifted to the north in July and August and are entrained into the Beaufort Gyre.

3.7.3 Seasonal-Scale Siberian Seas Anomalies

The positive phase of the PDV-NP leads to a weakening of the Icelandic Low over the North Atlantic in winter, followed by negative MSLP anomalies in the spring and summer along the Siberian coast (Figure 3.6). Spring and summer both have warm near-surface air temperature anomalies across most of the Siberian river basins (Figure 3.7). There is a positive OHC anomaly in the Barents Sea in spring (Figure 3.8), coinciding with a region of anomalously low SIC (Figure 3.10). As the springtime circulation pattern is not conducive to increased inflow of Atlantic waters, the positive OHC anomaly in the Barents may be a consequence of ocean warming in the region of anomalous reduction of SIC. There are negative OHC and salinity anomalies in the Kara Sea that are strongest in winter and weaken through the spring to a minimum in summer and autumn. The positive phase of the PDV-NP also leads to a positive salinity anomaly in the Laptev Sea. The positive phase of the PDV-NP primarily leads to negative SIC anomalies extending eastward from the northern Kara Sea to the East Siberian Sea (**Error! Reference source not found.**). While the anomalous circulation pattern does not provide a clear answer for the pan-Arctic negative SIC anomaly, the anomalous warm near-surface air temperatures (Figure 3.7) may be leading to increased warmth being advected over the Siberian Seas, increasing low-level cloudiness and radiational heating of the surface and helping to enhance the sea ice loss. While there is a broad region of negative SIC anomalies in the summer and autumn, to the east of the Gulf of Ob and the Lena River delta, there are small regions of positive SIC anomalies. Looking more closely at the monthly anomalies helps uncover the processes happening here.

3.7.4 Monthly-Scale Laptev Sea Anomalies

The southern Laptev Sea, adjacent to the Lena River delta, is a region with positive SIC anomalies during the positive phase PDV-NP, while the western Laptev Sea and the East Siberian Sea have negative SIC anomalies. The positive SIC anomaly is most evident in August and September (Figure 3.11). This coincides with a region of negative OHC anomalies during the summer months, centered just to the east of the Lena River delta (Figure 3.12), which may be the cause of the reduced sea ice melt. The Laptev Sea also has a positive salinity anomaly during the summer months that extends far into the central Arctic (Figure 3.13).

Regressions of the monthly ocean temperature and salinity profiles on the PDV-NP time series at the mouth of the Lena River indicate the positive near-surface salinity anomaly persists throughout the year (Figure 3.19). From July through September, there is a negative ocean temperature anomaly at the surface, replaced by a positive anomaly during the rest of the year. The increased salinity and reduced temperatures during the summer would be consistent with a reduction in Lena River discharge.

3.8 Regressions of Arctic OHC, Salinity, and SIC on River Discharge Anomalies

To investigate the impact of freshwater discharge from the Mackenzie River, the summer and autumn 5-25 m integrated OHC, 5-25 m average salinity, and SIC were regressed on the time series of the annual Mackenzie River discharge anomaly (Figure 3.20); regressions were confined to the period 1973-2013 due to the short record for the river discharge. Similarly, ocean temperature and salinity were regressed on the annual river discharge time series and displayed as latitude-depth profiles along the 135°W meridian through the Beaufort Sea (Figure 3.21). The total annual discharge time series was shown in Figure *3.3*.

Positive Mackenzie River discharge anomalies are associated with increased OHC near the coast in the Beaufort Sea and north of Alaska and with broad negative salinity anomalies throughout the Beaufort Sea (Figure 3.20). The regressions of the subsurface salinity profiles on the Mackenzie discharge time series indicate a positive salinity anomaly at the surface from 70°N to about 73°N, possibly due to salt rejection from many freeze/thaw cycles, but a broad negative salinity anomaly from the 70°N northward through the Beaufort Gyre, indicating a buildup of freshwater in the upper Beaufort Gyre (Figure 3.21). Increased Mackenzie River discharge also leads to warmer ocean temperatures in summer and autumn near the coast capped with a negative temperature anomaly at the surface in summer. As discussed previously about interpretation of anomalies at the top of the ocean column due to the observations from CTDs and drifters typically being at 10 m and deeper, the same caution should be exercised with the interpretation of these surface-based negative temperature and positive salinity anomalies.

Positive Mackenzie River discharge anomalies also lead to increased sea ice concentration adjacent to the Beaufort Sea coast in summer and autumn (Figure 3.20). The positive SIC anomaly at the mouth of the Mackenzie River in summer is in contrast to the study by Nghiem et al. (2014) which found that warm river waters contribute directly to sea ice melt. The positive SIC anomaly in autumn, however, may be linked to the negative salinity anomaly: when surface waters cool in the autumn, the anomalous freshwater at the ocean surface with its higher freezing point allows sea ice to form more easily. The large-scale features (positive OHC and negative salinity anomalies) agree with the expected effects of the Mackenzie River; however, the features just off the mouth of the river, including the positive SIC anomaly cannot be linked to the sole effect of the discharge of the Mackenzie River.

3.9 Summary

The focus of this analysis has been to unravel how natural low-frequency climate variability impacts Arctic sea ice. This analysis shows the interconnectedness of the atmosphere, ocean, cryosphere, and land surface. The climatology of the hydrological parameters shows melting of winter and spring solid precipitation over the Mackenzie and Lena River basins leads to river runoff peaks in May and June, with peak river discharge near the mouths of the rivers in June. Seasonally speaking, the precipitation maximum occurs at the same time as the ET maximum, leading to a reduction of the amount of water that becomes runoff in the summer. The fresh river discharge peak drives the Beaufort and Laptev Sea salinity June minima. Warming of the ocean surface, though, is primarily driven by the reduction in SIC, which allows for absorption of solar radiation by the open water, heating, and a peak in ocean temperature during the months with the lowest SIC.

Modification of the atmospheric circulation on decadal and multidecadal time scales impacts warm inflow from the North Atlantic and North Pacific into the Arctic basin, and also leads to redistribution of sea ice in the Arctic. The positive phase AMO leads to a positive MSLP anomaly over Greenland, in the central Arctic, and in the North Pacific. These anomalous circulation patterns lead to increased inflow of relatively warm North Pacific waters through Bering Strait and a warm OHC anomaly in the Chukchi Sea. The anomalous high in the central Arctic and anomalous lows over land, especially in summer, drive anomalous easterlies along the coastlines on both the North American and Siberian coasts, leading to ice drift to the north away from the coasts. This in turn results in the negative SIC anomalies throughout the Arctic marginal seas during positive phase AMO. The reduction in SIC also leads to increased open waters and heating by downward solar radiation, and a positive OHC anomaly in the Beaufort and Chukchi Seas in summer and autumn. The Beaufort Sea also has a negative salinity anomaly throughout the year, which could be due to a combination of increased sea ice melt, increased relatively fresh Pacific inflow, and increased river discharge from the Mackenzie River. With the Mackenzie River and the Beaufort Sea, a link to river discharge and continental hydrology is clear, with positive phases of the AMO leading to increased ocean temperatures and decreased ocean salinity in the Beaufort Sea adjacent to the coast corresponding in time to the annual peak in river discharge, which then progresses further north and begins to descend in the Beaufort Gyre region.

On the Siberian side, the anomalous high over Greenland and Iceland reduces warm North Atlantic inflow in the Arctic, resulting in a negative OHC anomaly in the Barents and Kara Seas but normal OHC in the Laptev Sea. There are negative salinity anomalies in the Kara Sea and positive salinity anomalies in the Laptev Sea. The positive salinity anomaly in the Laptev Sea could be caused by a combination of the anomalous high pressure anomaly over the central Arctic and its accompanying anomalous easterly winds along the Siberian coast opposing the flow of freshwater that typically enters the Laptev Sea from the Kara Sea and the possible reduction in the available river discharge from the Lena River. At the shorter monthly scale, the positive phase AMO leads to positive salinity and SIC anomalies extending north from the mouth of the Lena River.

The positive phase PDV-PP leads to opposite anomalies than the positive phase AMO, with decreased OHC and increased ocean salinity in the Beaufort Sea and increased SIC throughout the Arctic marginal seas. In the summer, negative MSLP anomalies over the central Arctic and positive MSLP anomalies over land generate anomalous westerlies over the Arctic's marginal seas. This results in sea ice divergence and ice drift to the south due to Ekman transport and the positive SIC anomalies in the Arctic during positive phase PDV-PP.

The mechanisms linking the PDV-NP to negative SIC anomalies is less clear: the anomalous circulation pattern during most of the summer would cause ice drift toward the coast; however, broad regions of negative SIC anomalies are seen instead.

At the shorter monthly time scale, the central Arctic is dominated by a positive MSLP anomaly in September, leading to sea ice convergence toward the central Arctic and the maximum spatial extent of the negative SIC anomaly. Like the positive phase AMO, the positive phase PDV-NP is linked to positive OHC and negative salinity anomalies in the Beaufort Sea adjacent to the coast corresponding in time to the annual peak in river discharge. In the southern Laptev Sea, a positive SIC anomaly at the Lena River mouth corresponds to a region of negative OHC and positive salinity anomalies suggesting a reduction in Lena River discharge.

The regressed anomalies of Beaufort Sea OHC, salinity, and SIC on the Mackenzie River discharge time series found increased discharge from the Mackenzie River is associated with positive OHC and negative salinity anomalies in the Beaufort Sea in the upper 25 m and throughout the water column on the continental shelf and to deeper waters north of the shelf break, as would be expected by the addition of relatively warm, fresh waters. However, the regressed SIC anomalies show a positive SIC anomaly at the mouth of the Mackenzie River in summer, which is counterintuitive given the increased river discharge and presumably increased heat flux into the Beaufort Sea. This highlights the challenge of understanding the impact of the Mackenzie River on the Beaufort Sea, as the surface forcing due to atmospheric circulation anomalies is important for sea ice variability while the deeper footprint of the river discharge must also be understood.

Table 3.1. Monthly mean and total annual heat flux (PJ) for the four Russian rivers and the Mackenzie River. The heat flux for the Ob, Yenisey, Lena, and Kolyma Rivers is 0 PJ in May and October because the limited number of river temperature observations during those months due to frozen rivers results in the river temperature being set equal to 0°C for purposes of heat flux calculations.

	Ob River	**Yenisey River**	**Lena River**	**Kolyma River**	**Mackenzie River**
	1958-2016	**1958-2016**	**1958-2016**	**1978-2016**	**1972-2016**
May	0	0	0	0	635
June	3445	6694	5393	1492	2920
July	5087	4270	6158	1108	3023
August	3428	2908	4043	833	2333
September	1307	1819	1678	410	1282
October	0	0	0	0	264
Total Annual Heat Flux (PJ)	13267	15691	17271	3843	10463

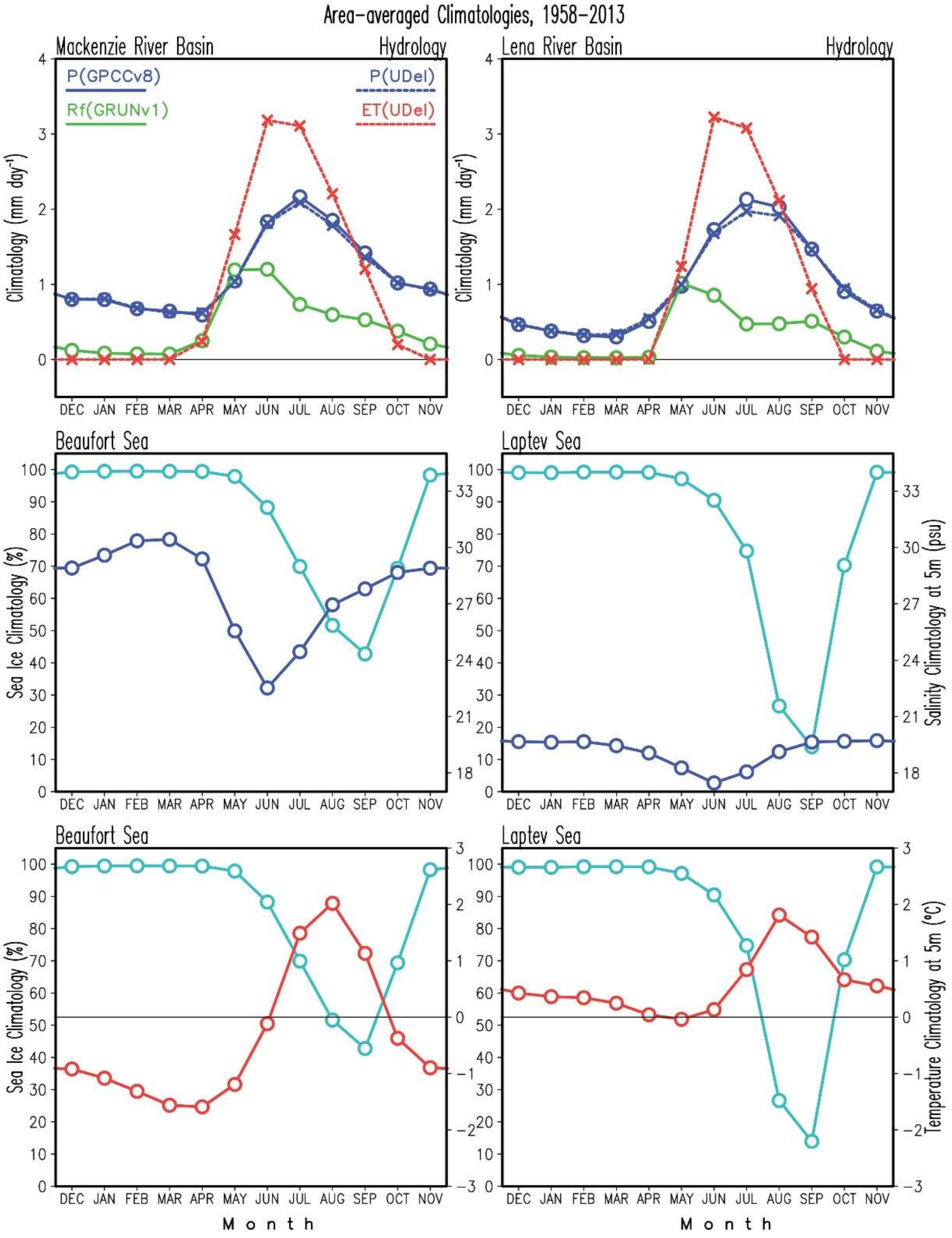

Figure 3.1. Annual cycle of area-averaged monthly hydrological variables (precipitation, ET, runoff), SIC, 5 m salinity, and 5 m OHC for the Beaufort and Laptev Seas near the mouths of the Mackenzie and Lena Rivers, respectively, averaged over the 1958-2013 period. Precipitation data are from GPCCv8 and UDEL, ET from UDEL, runoff from GRUN, SIC data are from HadISST2.2, and salinity and OHC data are from EN4.2.1.

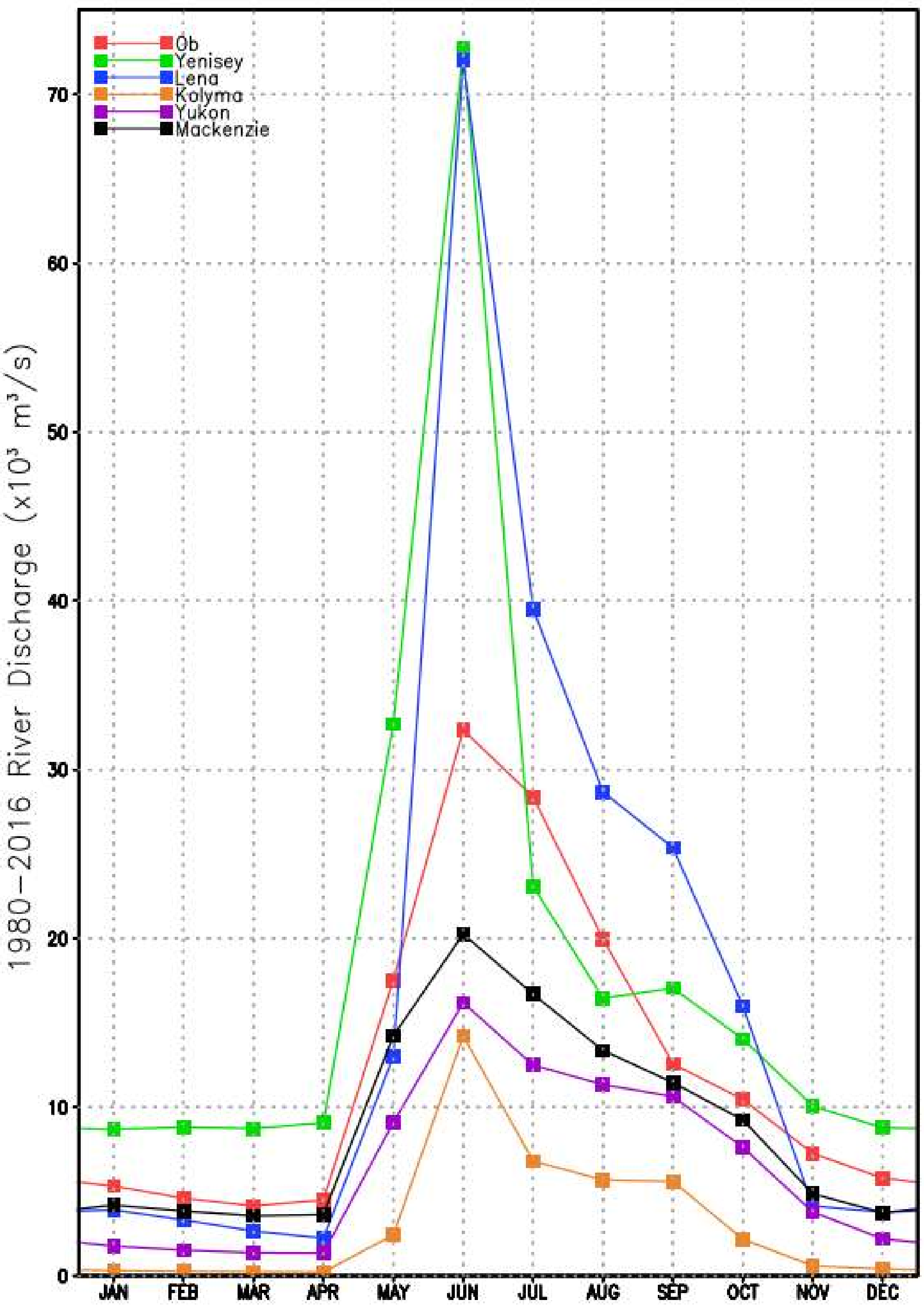

Figure 3.2. Climatological monthly river discharge from the six major Arctic rivers at the gauge station nearest the mouth of each river. The climatologies were calculated over the 1980-2016 time period from monthly mean discharge from the R-ArcticNET and ArcticGRO data sets.

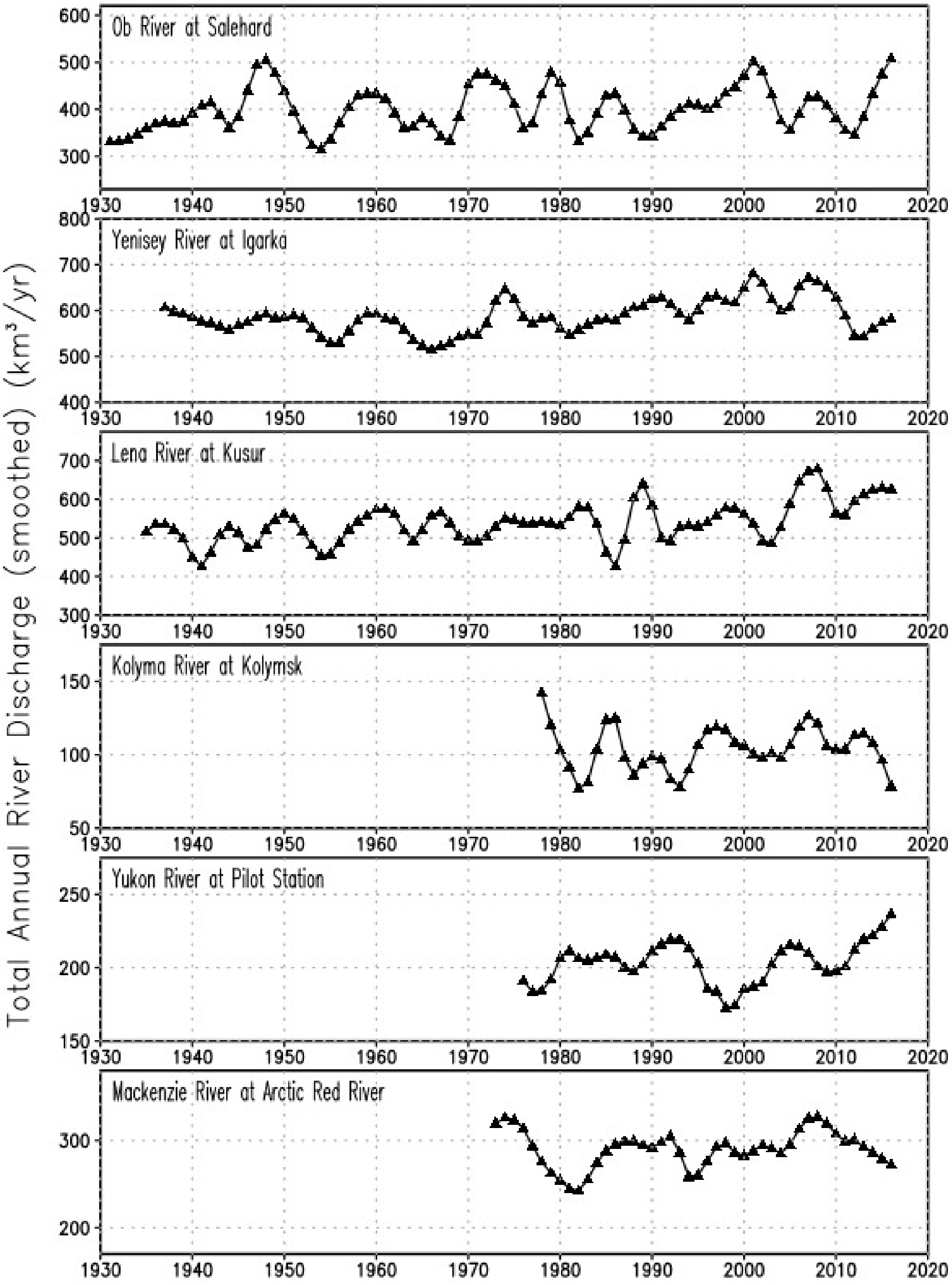

Figure 3.3. Time series of annual river discharge. Annual values are calculated over the hydrological year from October through the following September. The time series have been smoothed using the loess filter with an 8-year time window. Discharge data are from R-ArcticNET and ArcticGRO.

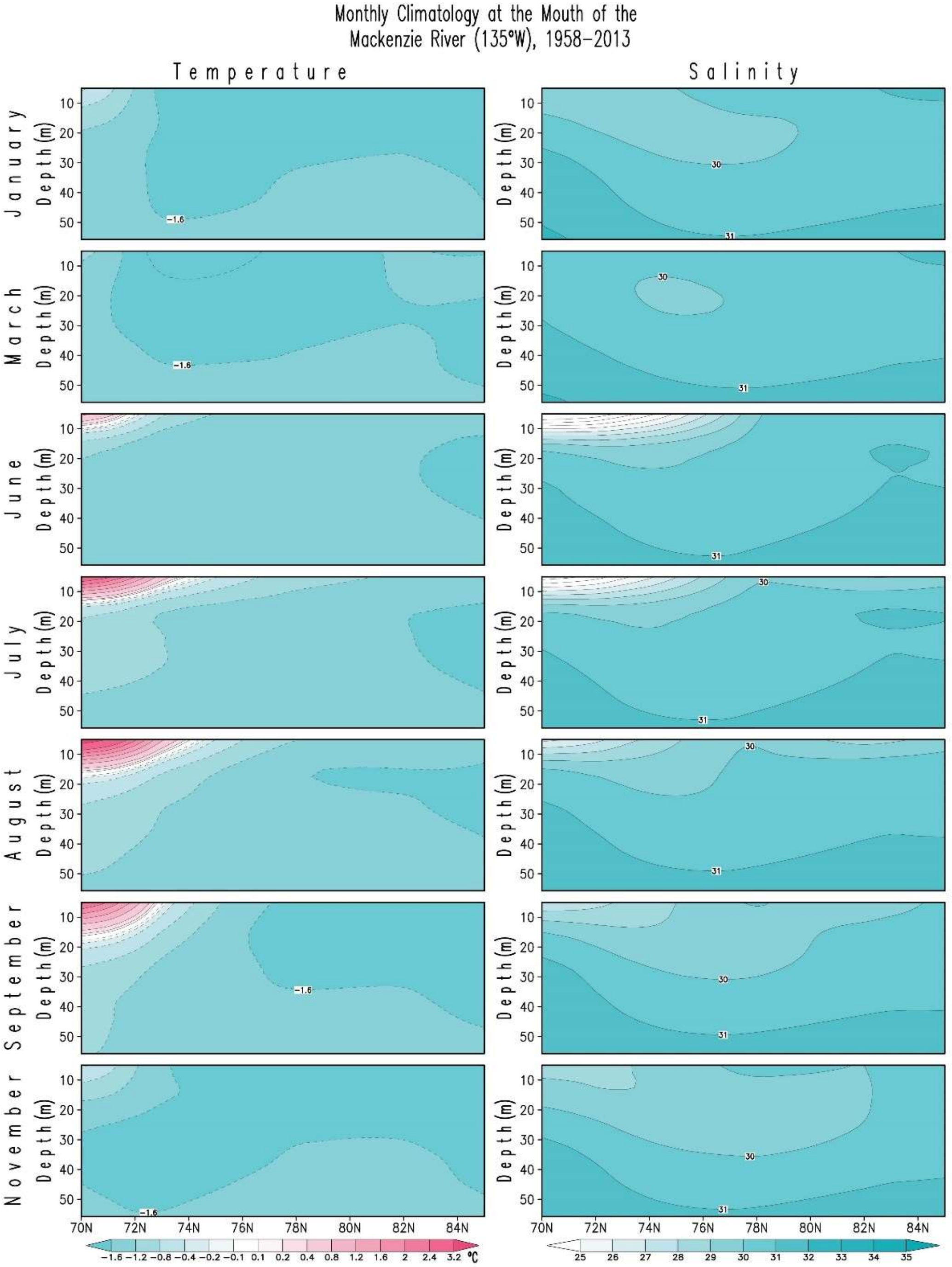

Figure 3.4. Monthly climatology of (left) ocean temperature and (right) salinity profiles from 5 to 55 m depth along 135°W from the mouth of the Mackenzie River to 85°N. Temperature is contoured using a telescoping contour interval as indicated on the colorbar. Salinity is contoured every 1. Temperature and salinity are from EN4.2.1.

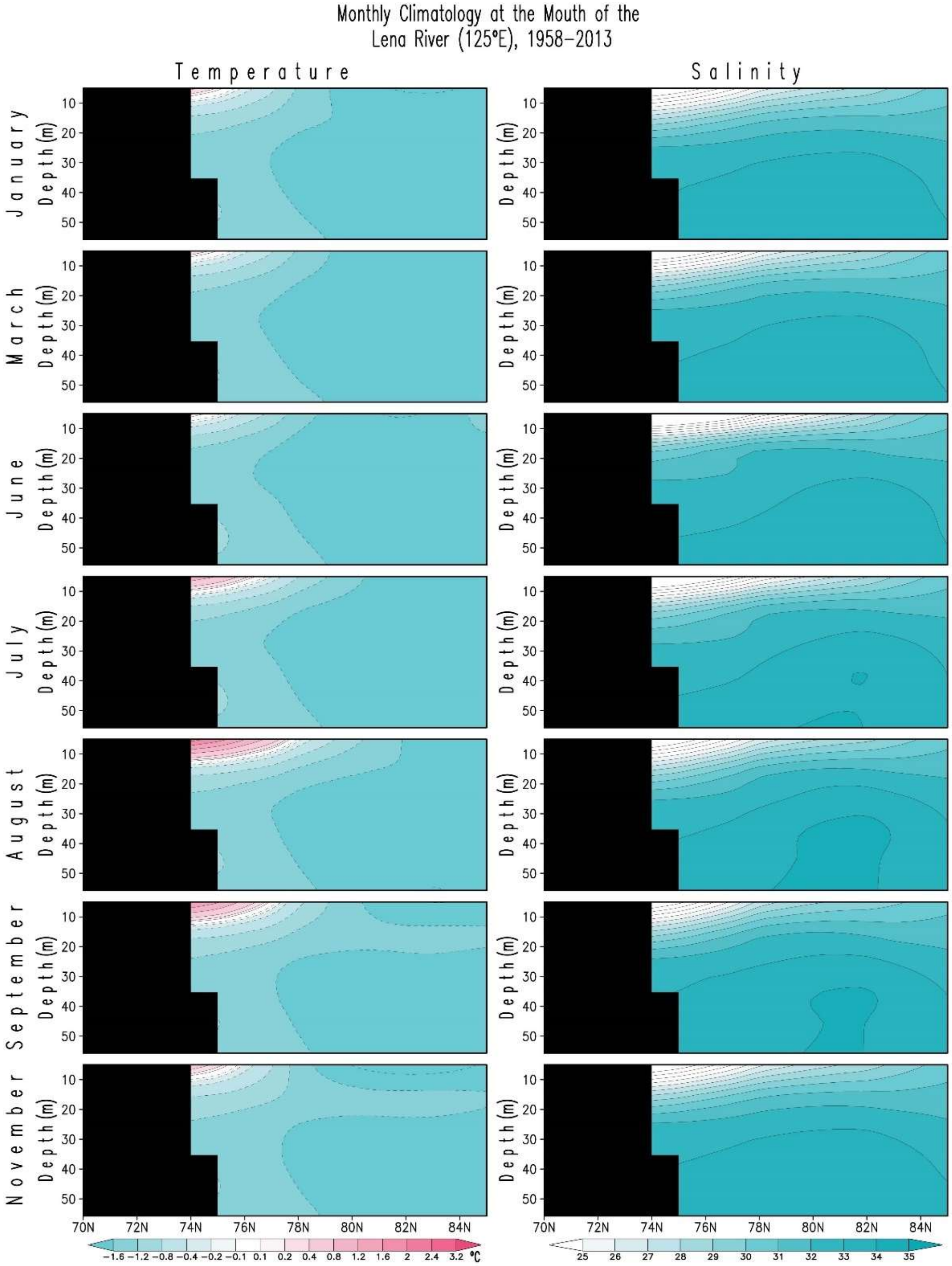

Figure 3.5. Monthly climatology of (left) ocean temperature and (right) salinity profiles from 5 to 55 m depth along 125°E from the mouth of the Lena River to 85°N. Temperature is contoured using a telescoping contour interval as indicated on the colorbar. Salinity is contoured every 1. Temperature and salinity are from EN v4.2.1.

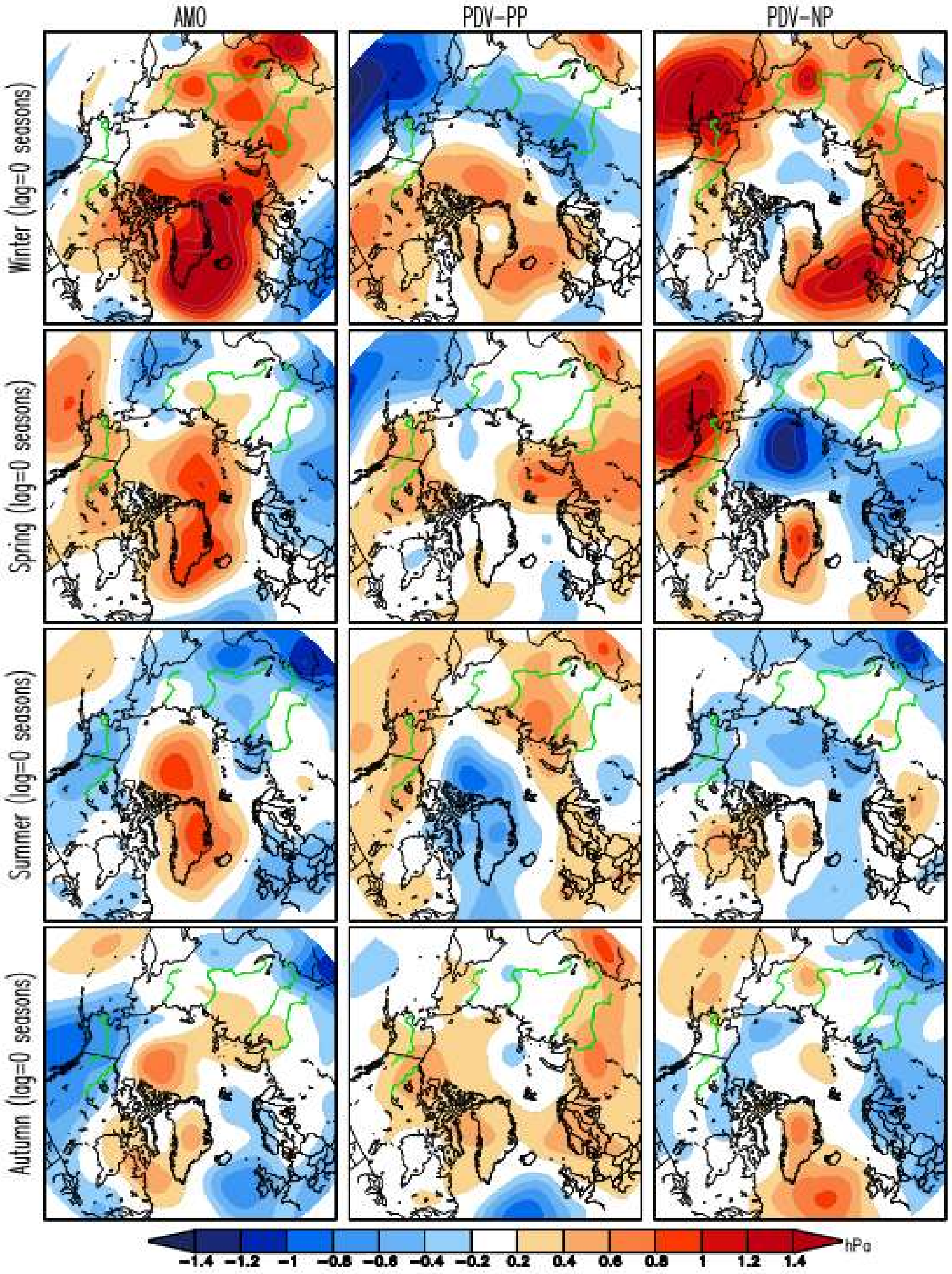

Figure 3.6. Seasonal regressed MSLP anomalies for the period 1958-2013. Linearly-detrended mean sea level pressure is regressed on smoothed AMO (left), PDV-PP (middle), and PDV-NP (right) time series. The single-season PC time series were smoothed using a loess filter with an 8-year time window. The MSLP is from the NCEP-NCAR Reanalysis. Contours are plotted every 0.2 hPa. Rivers are plotted in green.

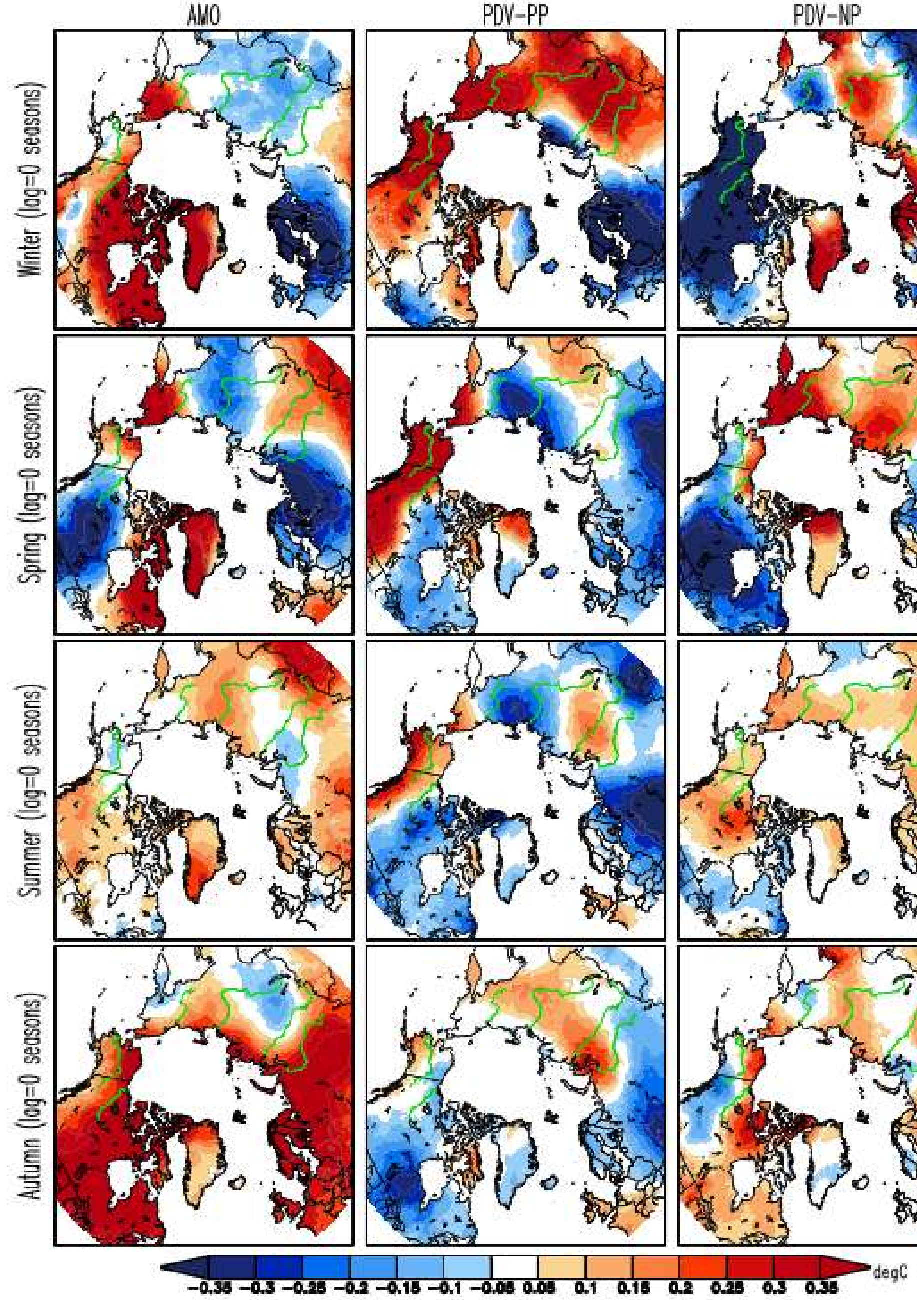

Figure 3.7. Seasonal regressed near-surface air temperature anomalies for the period 1958-2013. Linearly-detrended near-surface air temperature is regressed on smoothed AMO (left), PDV-PP (middle), and PDV-NP (right) time series. The single-season PC time series were smoothed using a loess filter with an 8-year time window. The air temperature is from CRU v4.02. Contours are plotted every 0.05°C. Rivers are plotted in green.

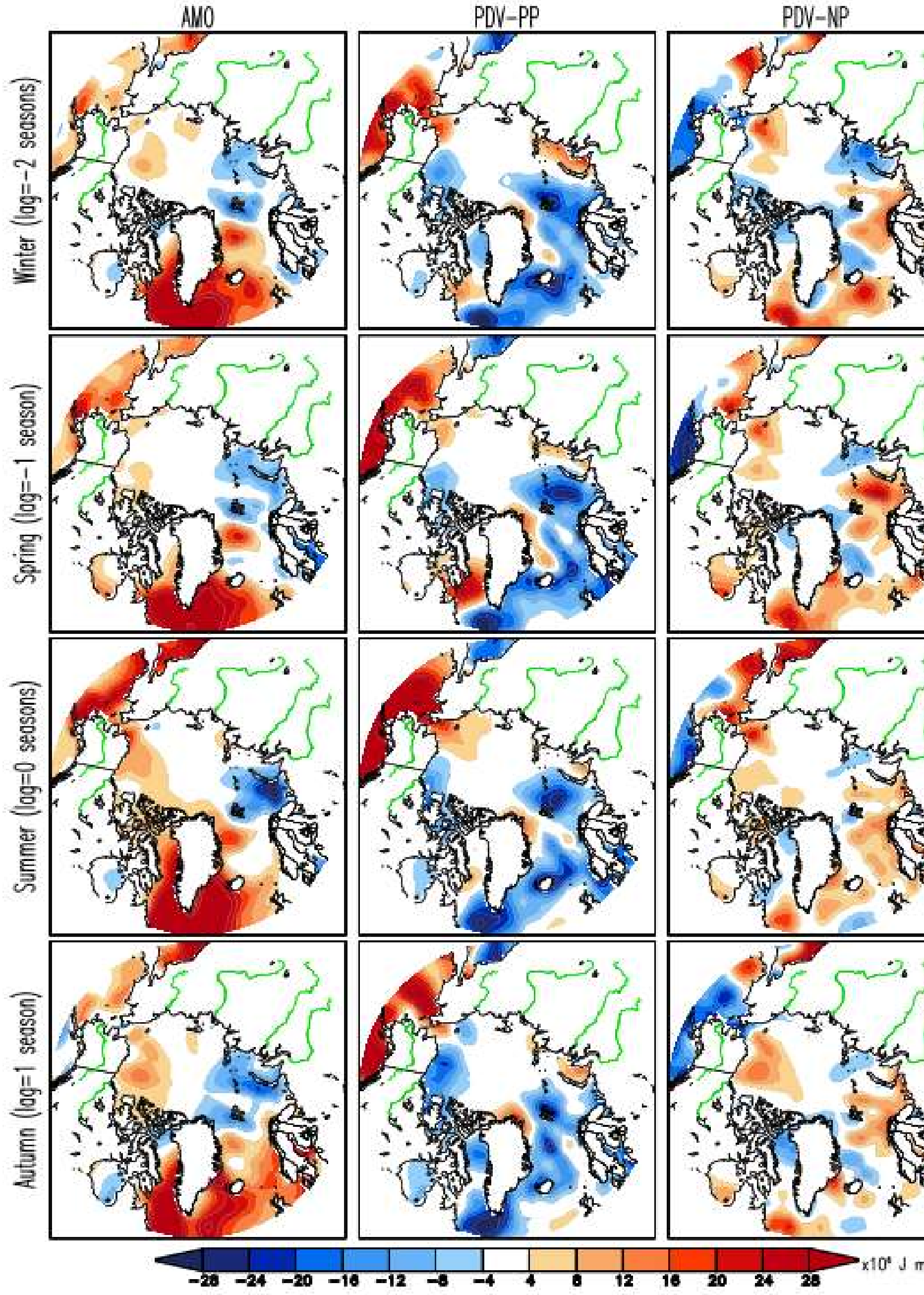

Figure 3.8. Seasonal regressed OHC anomalies for the 1958-2013 time period. Linearly-detrended OHC, integrated over the 5-25 m depth layer, is regressed on smoothed AMO (left), PDV-PP (middle), and PDV-NP (right) time series. Regression anomaly plots show the regression of the summer PC time series on the antecedent winter and spring, simultaneous summer, and subsequent autumn OHC. The single-season PC time series were smoothed using a loess filter with an 8-year time window. OHC is from EN4.2.1. Contours are plotted every 4×10^6 J m^{-2}. Rivers are plotted in green.

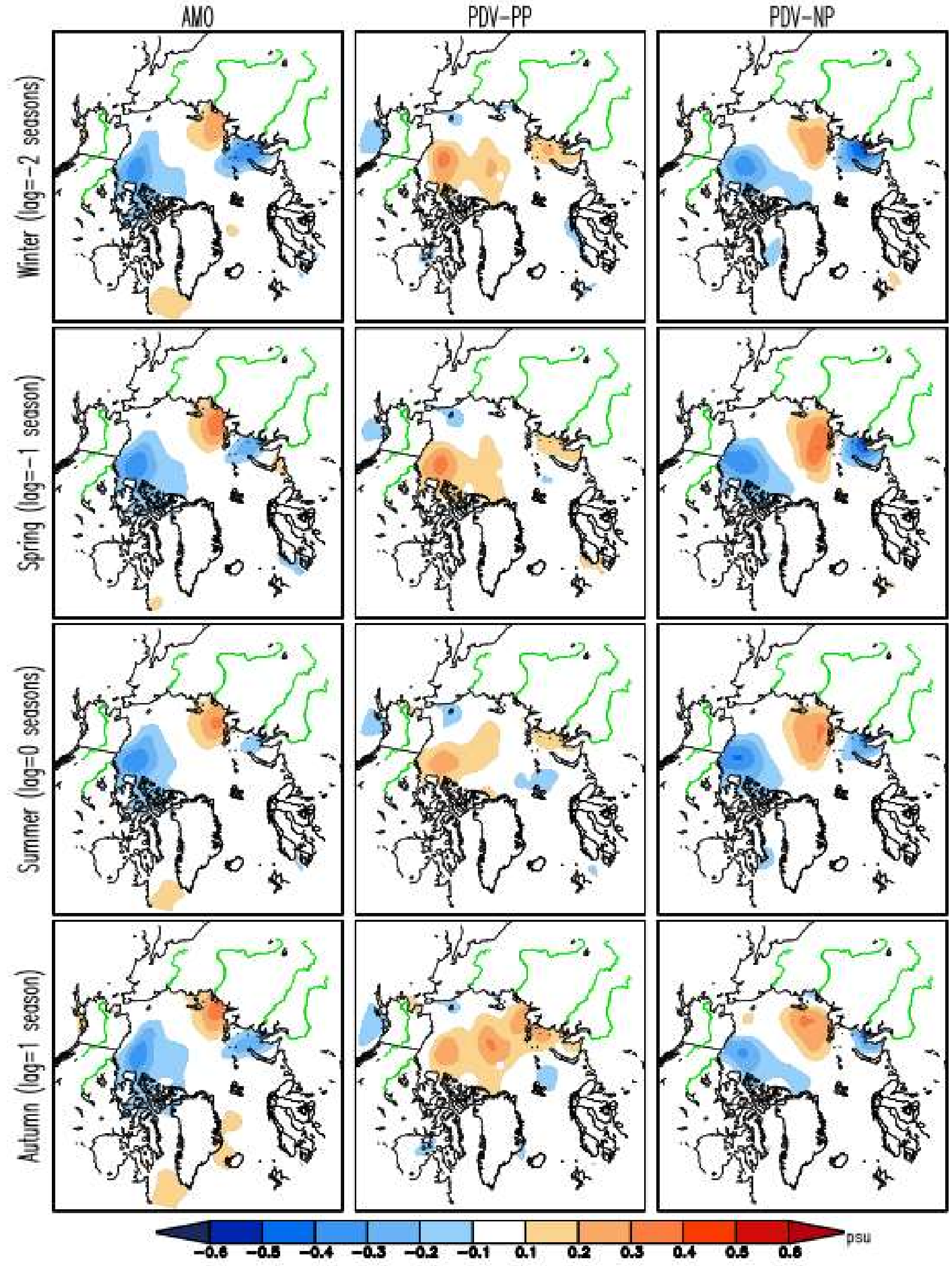

Figure 3.9. Seasonal regressed salinity anomalies for the period 1958-2013. Linearly-detrended salinity averaged over the 5-25 m depth layer is regressed on smoothed AMO (left), PDV-PP (middle), and PDV-NP (right) time series. Regression anomaly plots show the regression of the summer PC time series on the antecedent winter and spring, simultaneous summer, and subsequent autumn salinity. The single-season PC time series were smoothed using a loess filter with an 8-year time window. Salinity is from EN4.2.1. Contours are plotted every 0.1. Rivers are plotted in green.

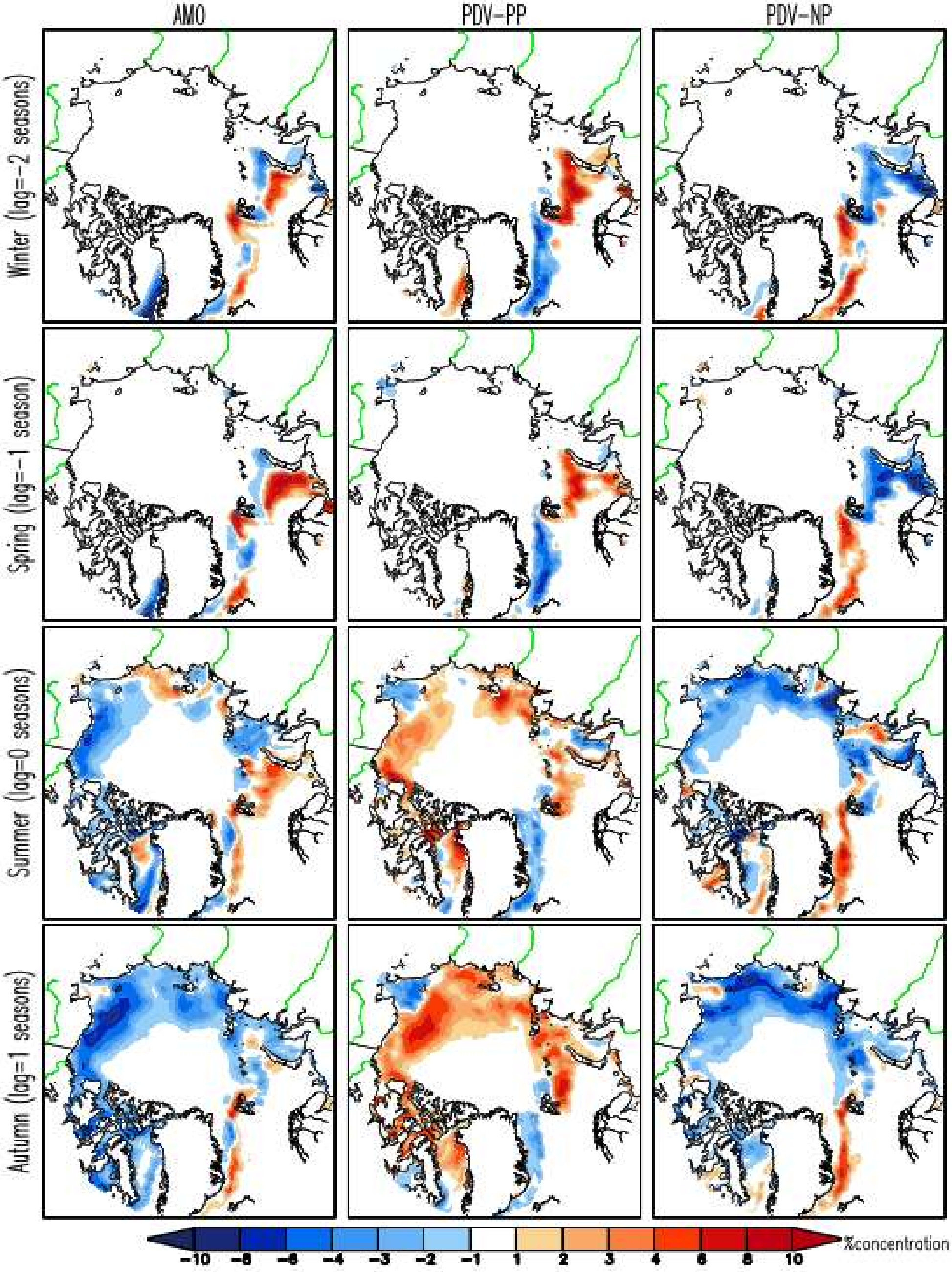

Figure 3.10. Seasonal regressed SIC anomalies for the 1958-2013 period. Linearly-detrended SIC is regressed on smoothed AMO (left), PDV-PP (middle), and PDV-NP (right) time series. Regressions were calculated for the summer PC time series on the antecedent winter and spring, simultaneous summer, and the subsequent autumn SIC. The single-season PC time series were smoothed using a loess filter with an 8-year time window. The SIC is from HadISST2.2. Regressed SIC anomalies are contoured using a telescoping interval from 1 to 2%. Rivers are plotted in green.

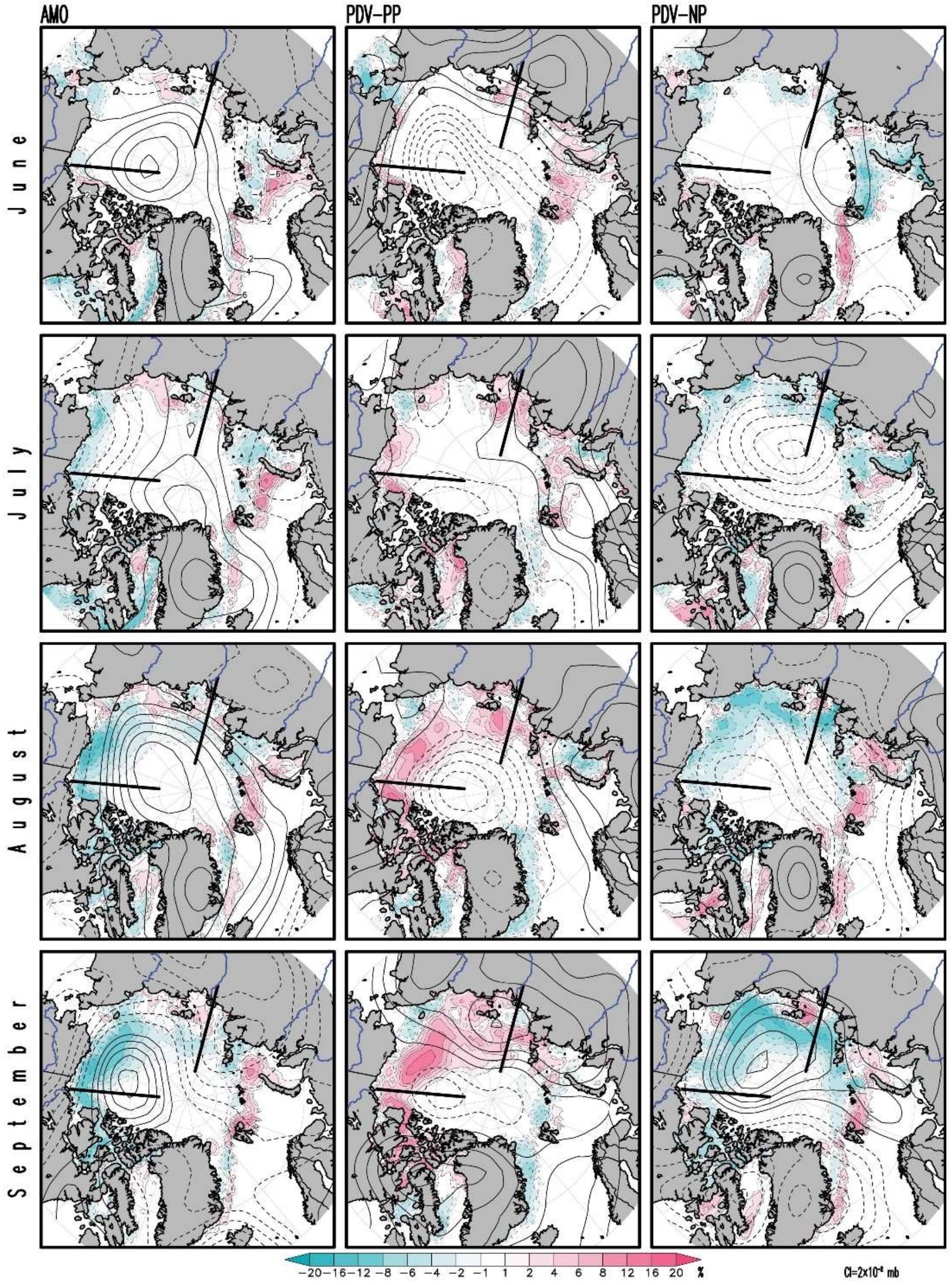

Figure 3.11. Monthly regressed MSLP and SIC anomalies for the 1958-2013 period. Linearly-detrended MSLP and SIC are regressed on smoothed seasonal AMO (left), PDV-PP (middle), and PDV-NP (right) time series. The PCs were smoothed with a loess filter with an 8-year time window. June, July, and August SIC and MSLP were regressed on summer time series; September SIC and MSLP were regressed on autumn time series. Regressed SIC anomalies are contoured using a telescoping interval from 1 to 4%; MSLP is contoured every 0.02 hPa; pinks indicate increased SIC and teals indicate reduced SIC. SIC is from HadISST2.2 and MSLP is from the NCEP-NCAR Reanalysis.

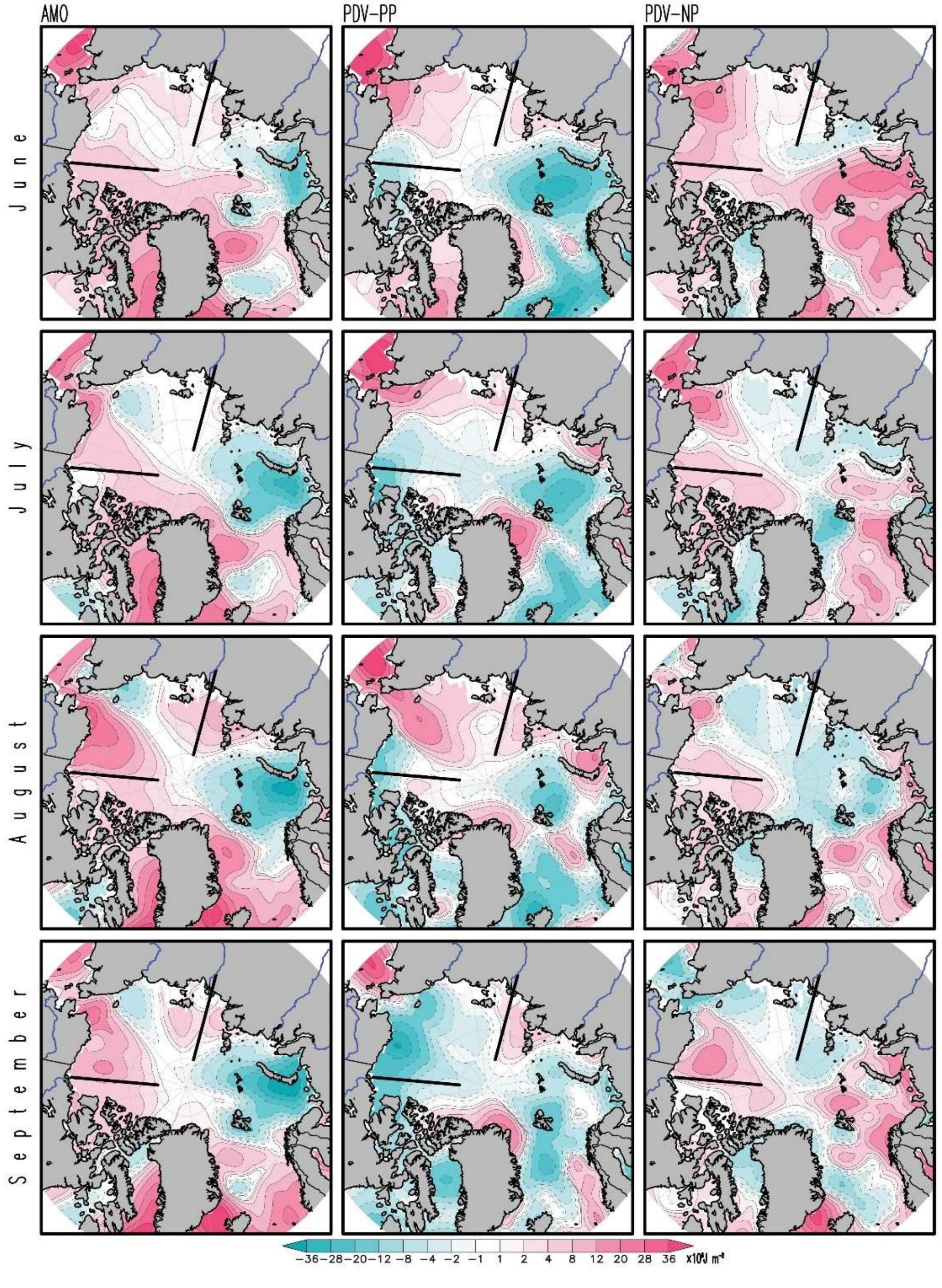

Figure 3.12. Monthly regressed OHC anomalies for the 1958-2013 period. Linearly-detrended OHC anomalies are regressed on smoothed seasonal AMO (left), PDV-PP (middle), and PDV-NP (right) time series. The PCs were smoothed with a loess filter with an 8-year time window. June, July, and August OHC were regressed on summer time series; September OHC was regressed on autumn time series. Regressed anomalies are contoured using a telescoping interval from $1\text{x}10^6$ to $8\text{x}10^6$ J m^{-2}; pinks indicate increased OHC and teals indicate reduced OHC. OHC is from EN4.2.1.

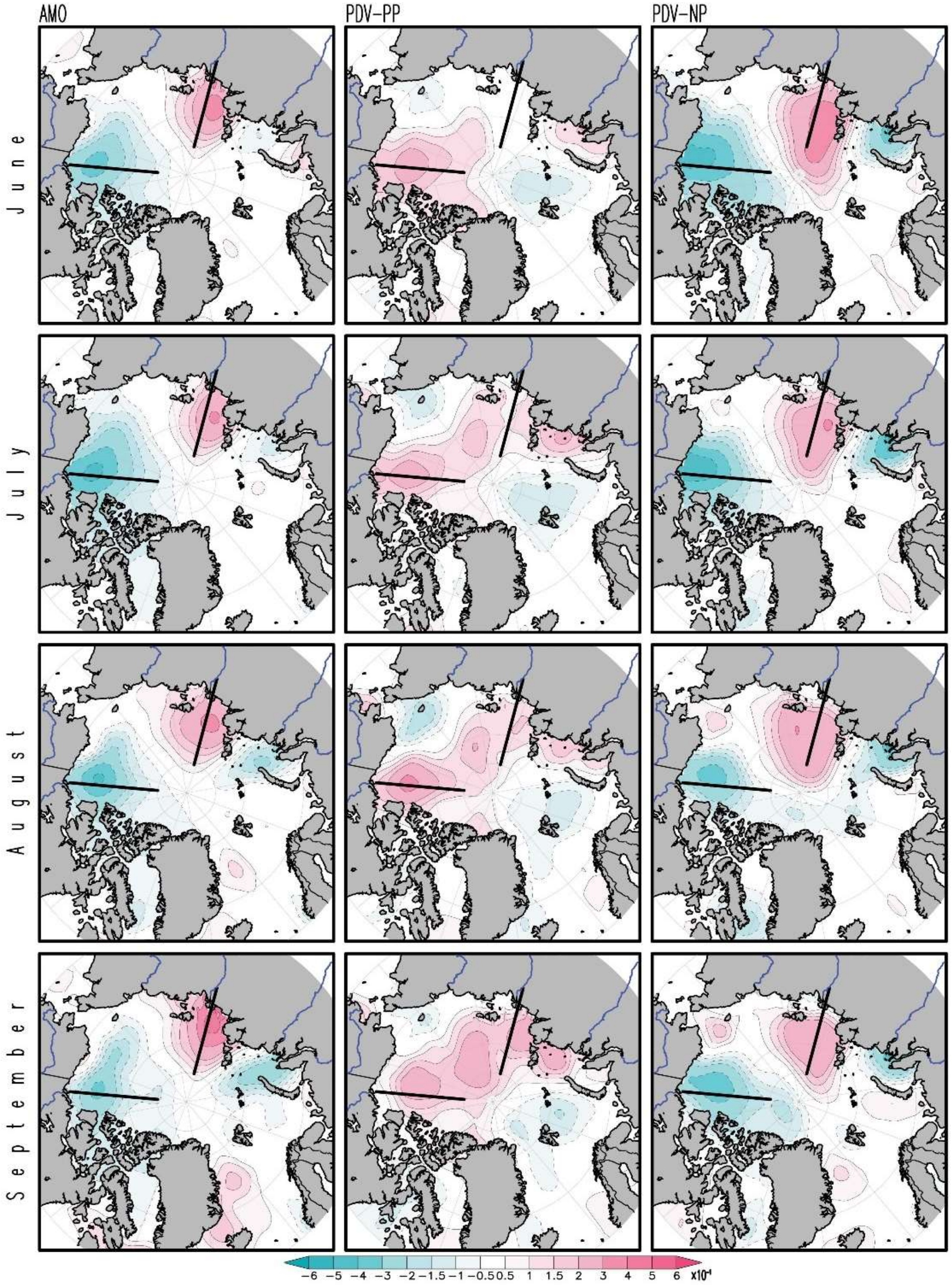

Figure 3.13. Monthly regressed salinity anomalies for the 1958-2013 period. Linearly-detrended salinity is regressed on smoothed seasonal AMO (left), PDV-PP (middle), and PDV-NP (right) time series. The PCs were smoothed with a loess filter with an 8-year time window. June, July, and August salinity were regressed on summer time series; September salinity was regressed on autumn time series. Regressed anomalies are contoured using a telescoping interval from 0.05 to 0.1; pinks indicate increased salinity and teals indicate reduced salinity. Salinity is from EN4.2.1.

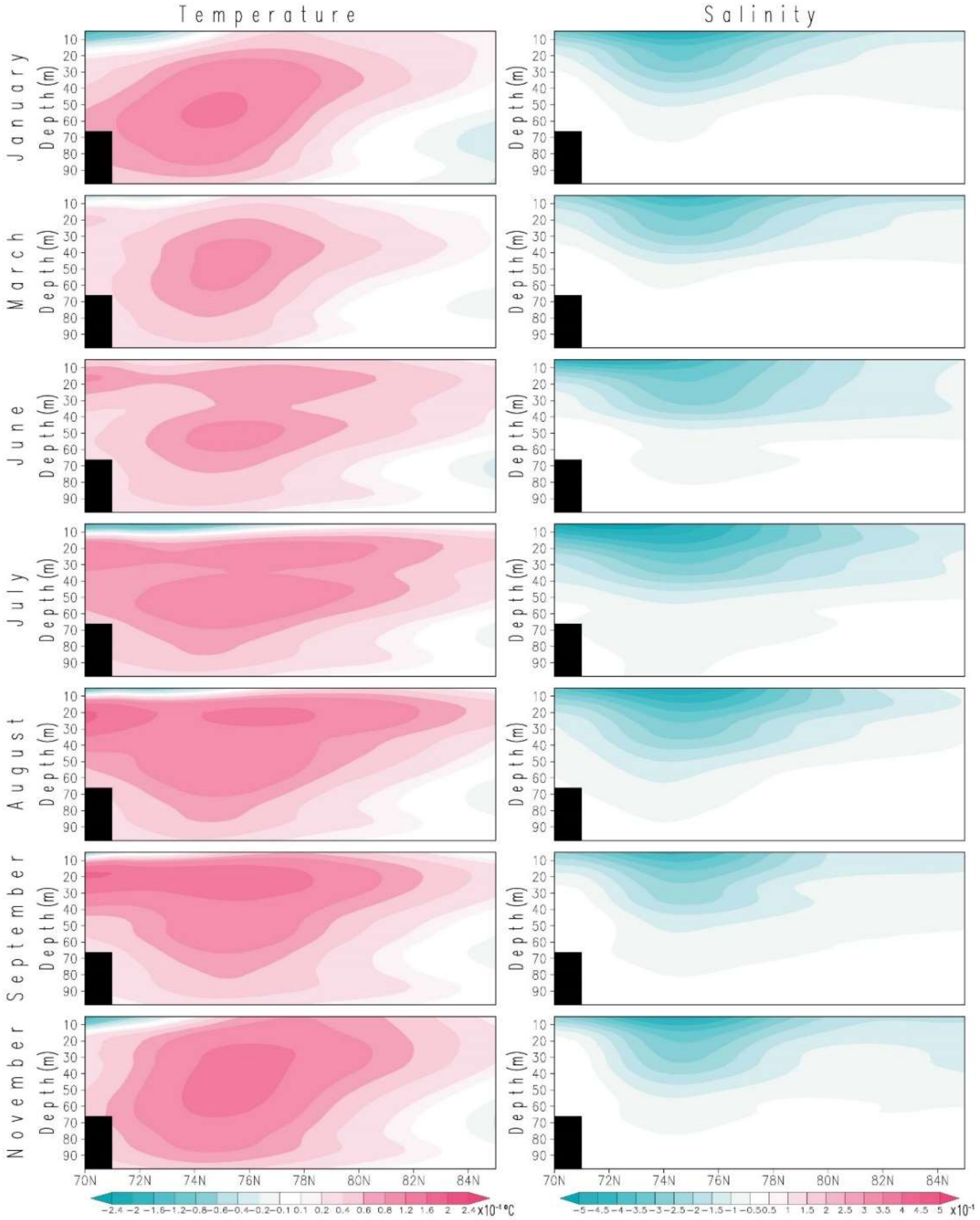

Figure 3.14. Monthly regressed ocean water temperature (left) and ocean salinity (right) anomalies for the 1958-2013 period along 135°W from the mouth of the Mackenzie River to 85°N. Linearly-detrended ocean temperature and salinity are regressed on the smoothed seasonal AMO time series. The AMO time series was smoothed using a loess filter with an 8-year time window. January temperature and salinity were regressed on winter AMO; March temperature and salinity were regressed on spring AMO; June, July, and August temperature and salinity were regressed on summer AMO; and September and November temperature and salinity were regressed on autumn AMO. The ocean temperature and salinity are from EN4.2.1. Temperature is contoured using a telescoping contour interval as indicated on the colorbar. Salinity is contoured every 0.05.

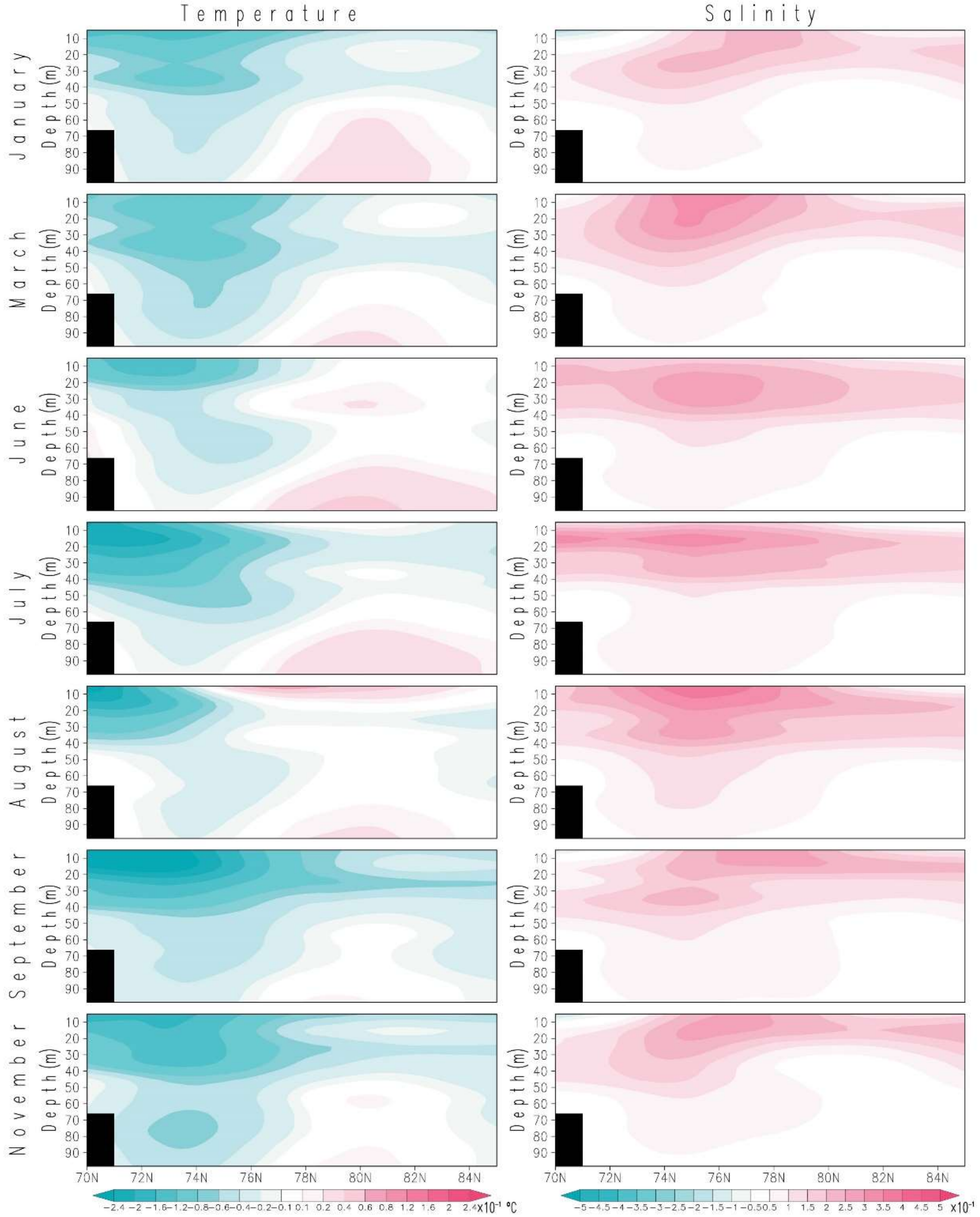

Figure 3.15. Monthly regressed ocean water temperature (left) and ocean salinity (right) anomalies from the mouth of the Mackenzie River to 85°N on the PDV-PP PC time series. The rest is the same as in Figure 3.14.

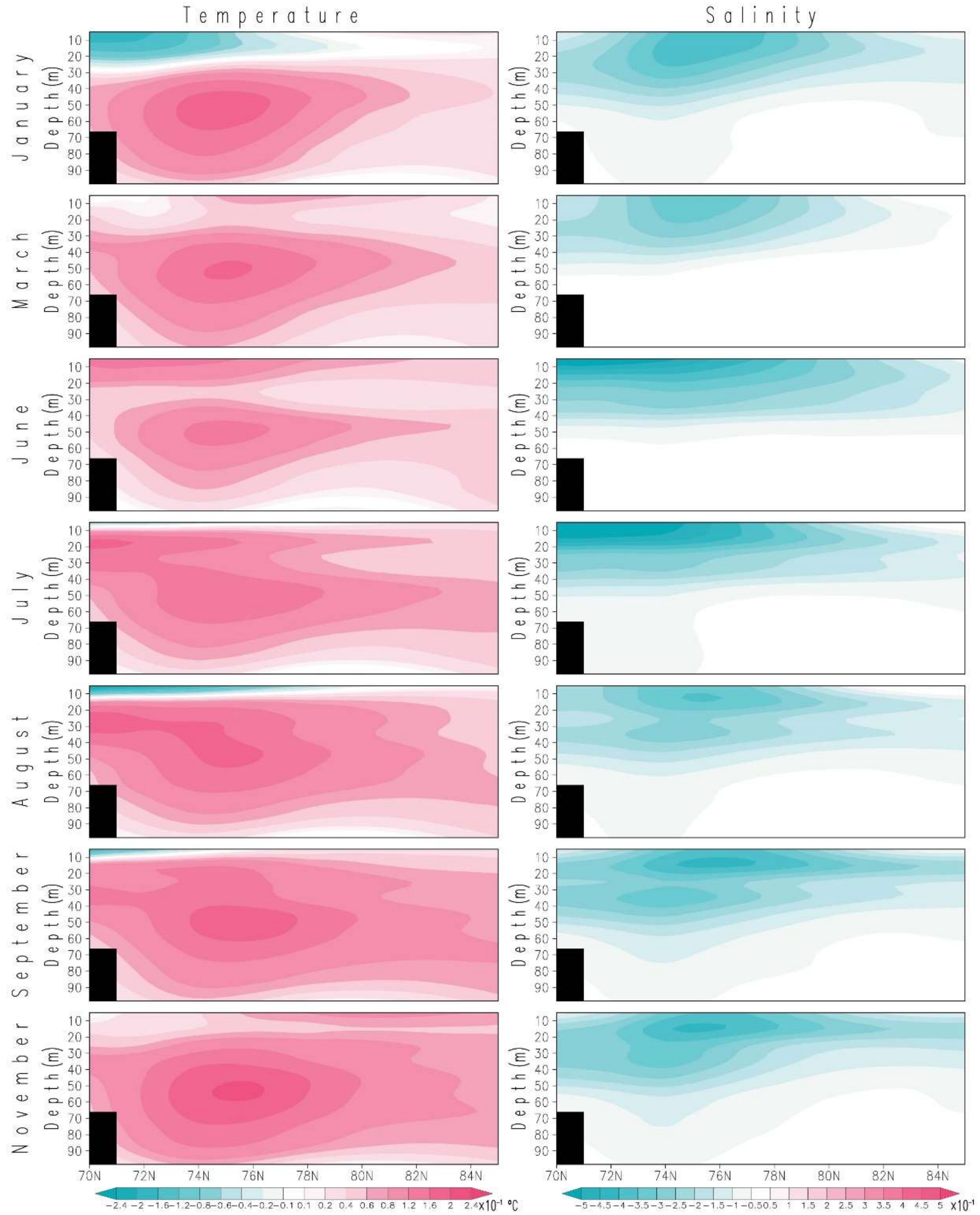

Figure 3.16. Monthly regressed ocean water temperature (left) and ocean salinity (right) anomalies from the mouth of the Mackenzie River to 85°N on the PDV-NP PC time series. The rest is the same as in Figure 3.14.

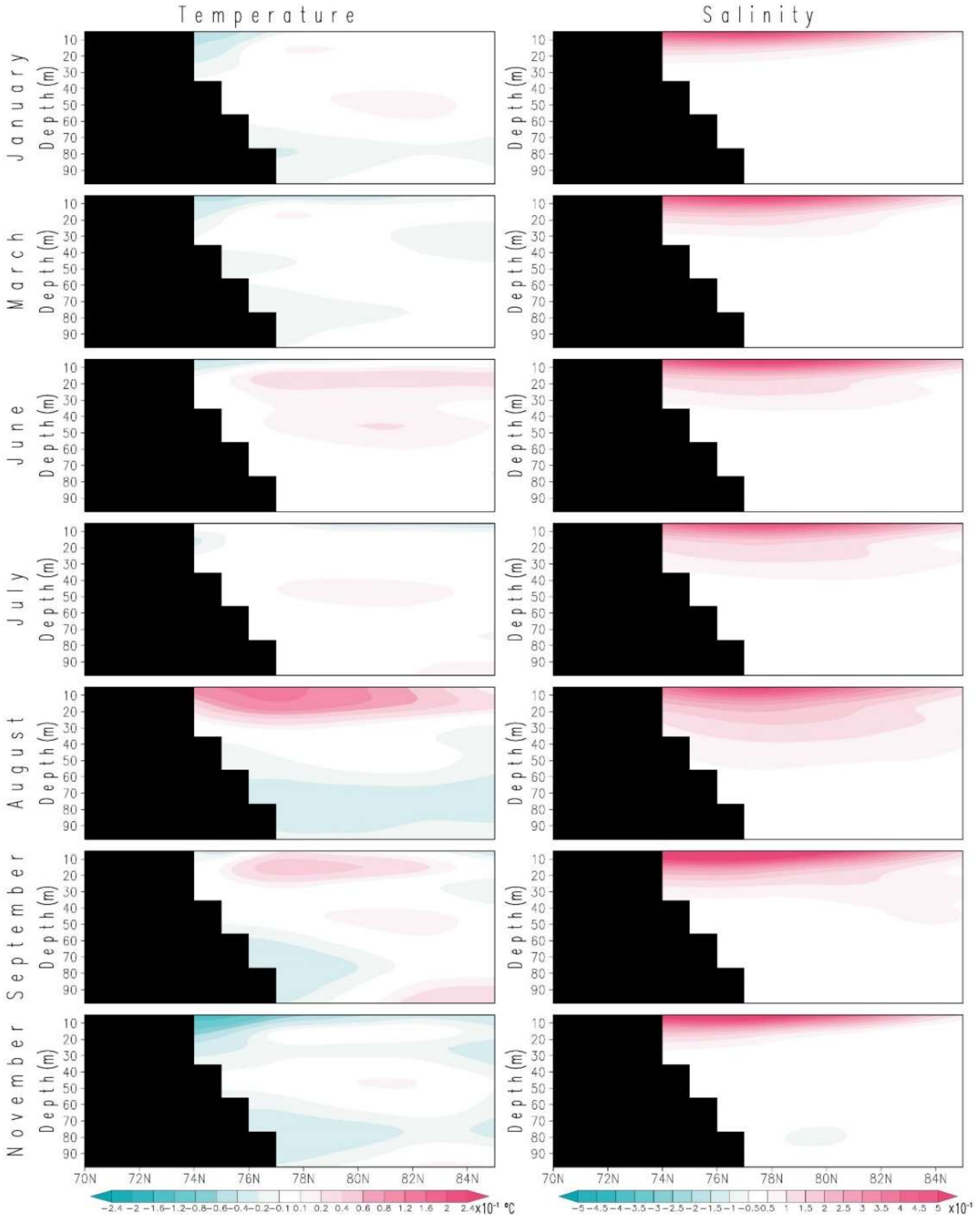

Figure 3.17. Monthly regressed ocean water temperature (left) and ocean salinity (right) anomalies for the 1958-2013 period along 125°E from the mouth of the Lena River to 85°N. Linearly-detrended ocean temperature and salinity were regressed on the smoothed seasonal AMO time series. The AMO time series was smoothed using a loess filter with an 8-year time window. January temperature and salinity were regressed on winter AMO; March temperature and salinity were regressed on spring AMO; June, July, and August temperature and salinity were regressed on summer AMO; and September and November temperature and salinity were regressed on autumn AMO. The ocean temperature and salinity are from EN4.2.1. Temperature is contoured using a telescoping contour interval as indicated on the colorbar. Salinity is contoured every 0.05.

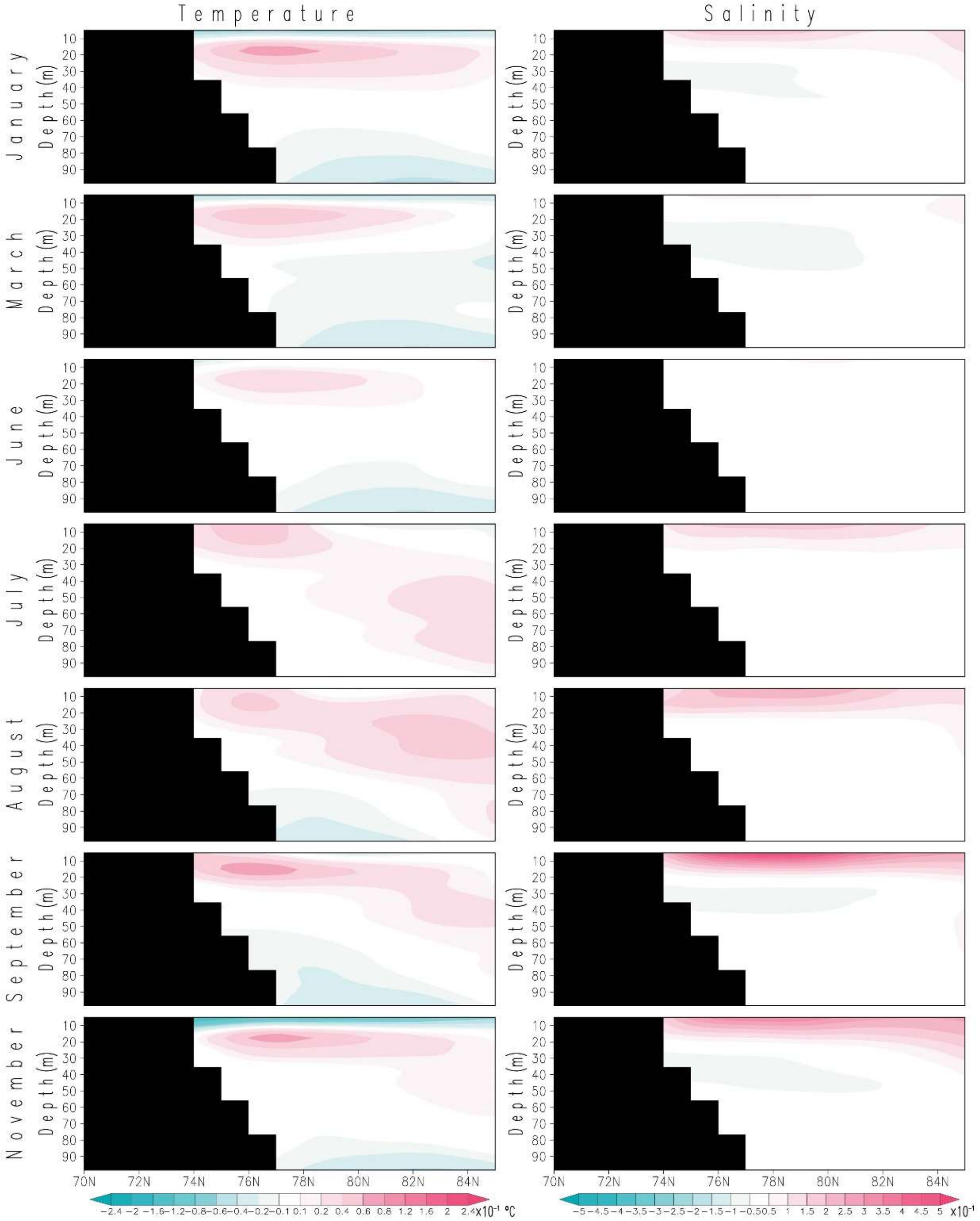

Figure 3.18. Monthly regressed ocean water temperature (left) and ocean salinity (right) anomalies from the mouth of the Lena River to 85°N on the PDV-PP PC time series. The rest is the same as in Figure 3.17.

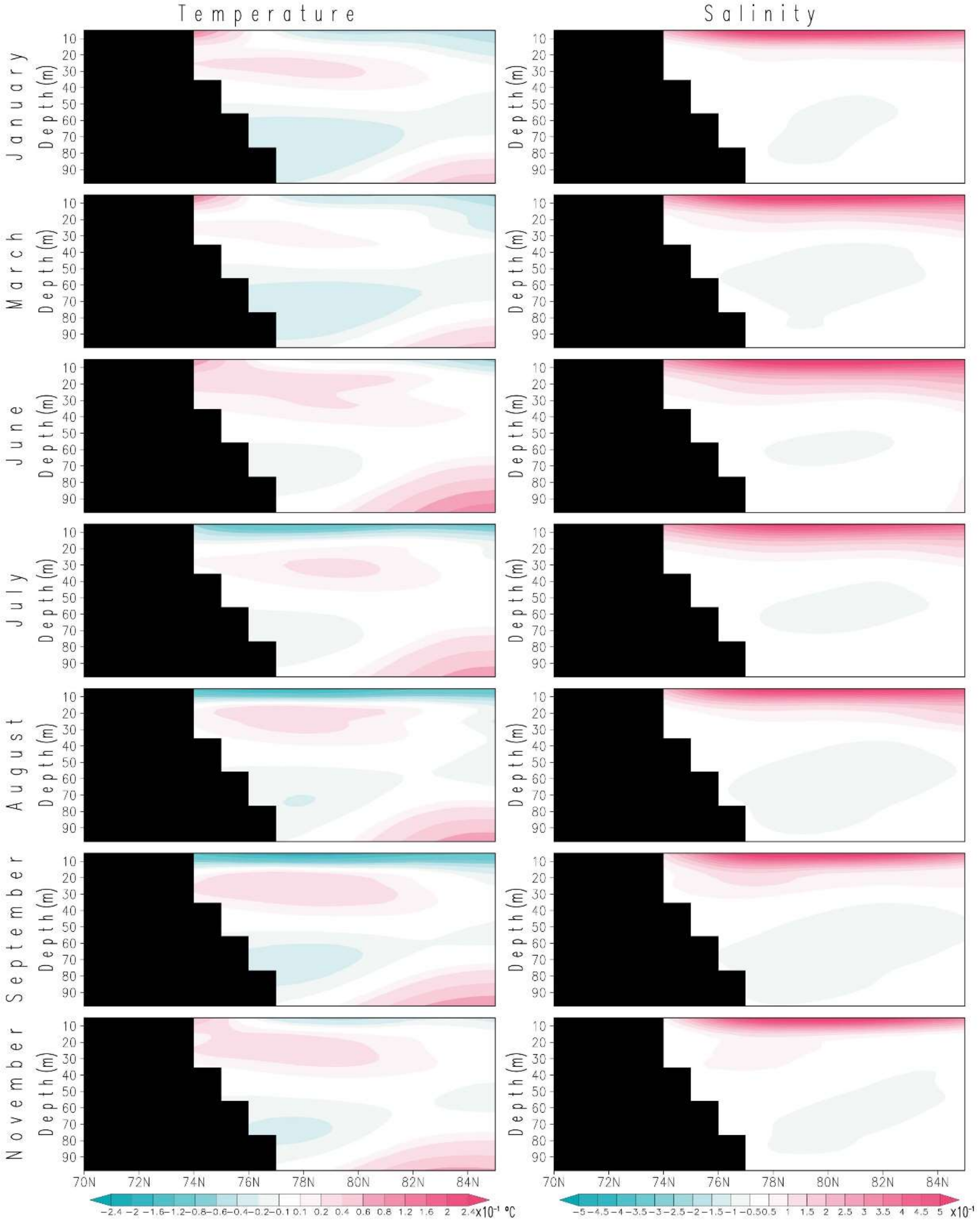

Figure 3.19. Monthly regressed ocean water temperature (left) and ocean salinity (right) anomalies from the mouth of the Lena River to 85°N on the PDV-NP PC time series. The rest is the same as in Figure 3.17.

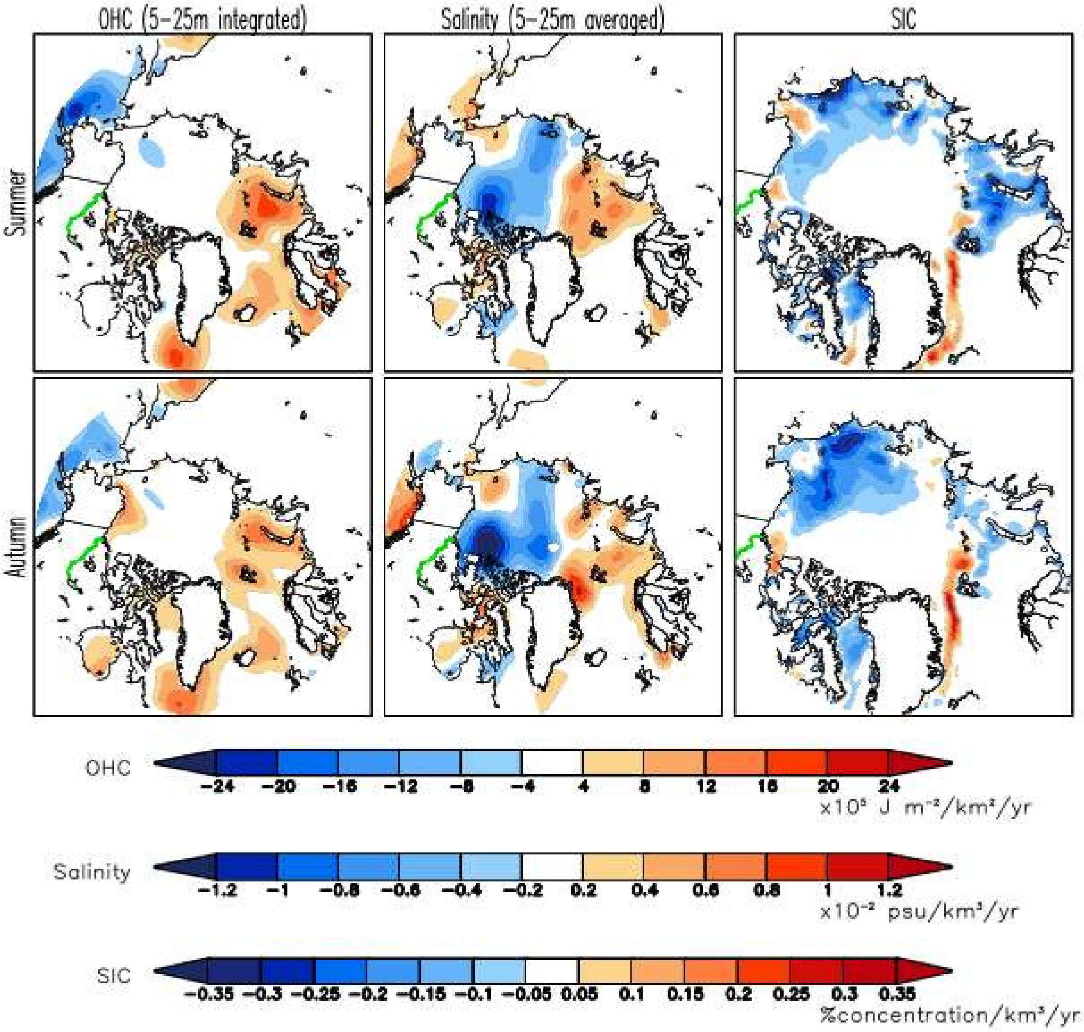

Figure 3.20. Seasonal regressed 5-25 m integrated OHC (left), 5-25 m average salinity (middle), and SIC (right) anomalies for the 1973-2013 time period. Linearly-detrended OHC, salinity, and SIC are regressed on the smoothed Mackenzie River discharge time series. The discharge time series was smoothed using a loess filter with an 8-year time window and then the anomaly was calculated as the difference from the 1973-2013 mean. OHC and salinity are from EN v4.2.1, SIC is from HadISST2.2, and discharge is from R-ArcticNET and ArcticGRO. OHC contours are plotted every 4x10^5 J m^{-2}, salinity contours are plotted every 0.002, and SIC is contoured every 0.05%/km^{3}yr^{-1}. The Mackenzie River is plotted in green.

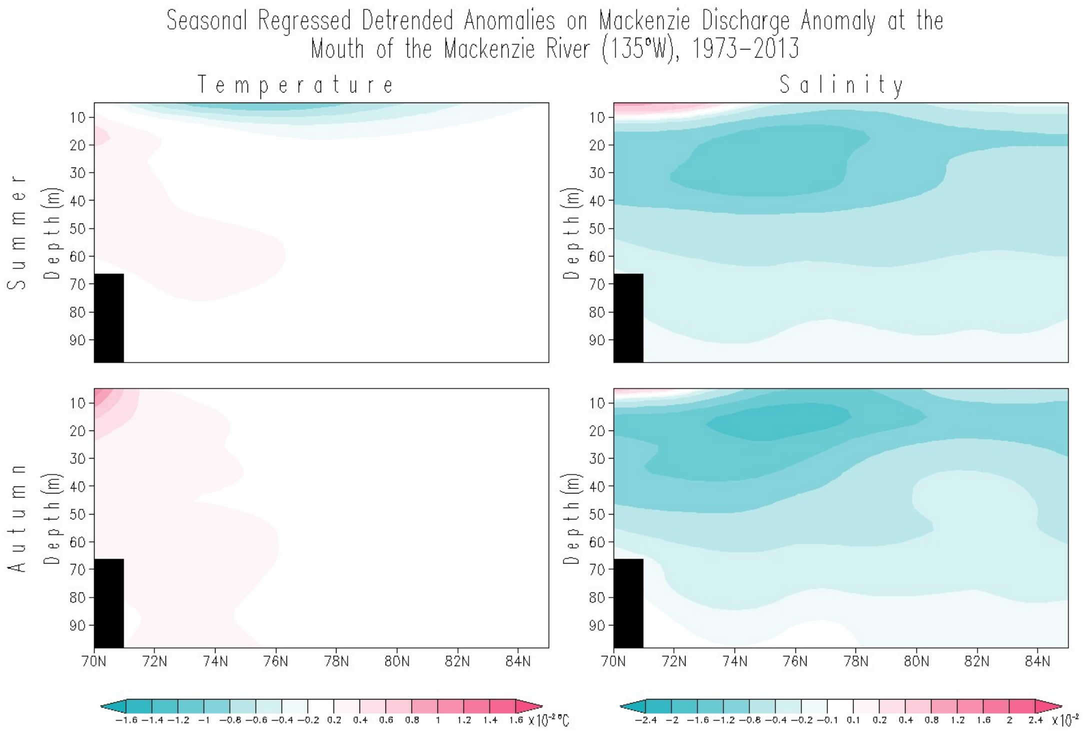

Figure 3.21. Seasonal regressed ocean water temperature (left) and ocean salinity (right) anomalies for the 1973-2013 period along 135°W from the mouth of the Mackenzie River to 85°N. Linearly-detrended ocean temperature and salinity are regressed on the smoothed annual Mackenzie River discharge time series. The total annual discharge time series was smoothed using a loess filter with an 8-year time window, and then the anomaly was calculated as the difference from the 1973-2013 mean. Ocean temperature and salinity are from EN v4.2.1. The contour interval for ocean temperature is 0.002°C and telescoping from 0.001 to 0.004 or salinity.

Chapter 4: Summary and Concluding Remarks

4.1 Outline and main issues

Arctic sea ice extent is one of the primary Global Climate Indicators, endorsed by the World Meteorological Organization, to describe climate change. Arctic sea ice extent has been in long-term decline since about the 1990s, reflecting both natural climate variability and anthropogenic climate change. The Arctic region as a whole is sensitive to the variability and change occurring in the adjoining oceans and continents and the overlying atmosphere, making diagnoses of regional Arctic climate variability and change challenging. Natural climate variability at interannual-to-decadal timescales that may impact the Arctic climate includes the NAO and PDO (Mysak 2001; Rigor and Wallace 2004; Polykov et al. 2005; Shimada et al. 2006). At multidecadal timescales, the AMO seems to play an important role in Arctic climate variability due to its strong footprint on North Atlantic sea surface temperatures (SST) and surface/subsurface salinity (Kavvada et al. 2013), on the hydroclimate of the adjoining continents (Nigam et al. 2011), and on winter/spring sea ice conditions in the preinstrumental record (Miles et al. 2014). While several studies have discussed the potential influence of the AMO on Arctic sea ice (Day et al. 2012; Miles et al. 2014; Yu et al. 2017), the mechanisms linking the AMO and sea ice are still unclear.

The goal of this research is to identify the contributions of low-frequency modes of climate variability on the observed summer sea ice trends, and establish the extent of the pathways linking sea ice variability with variability in the regional hydroclimate and river streamflow variability. Strong seasonal anomalies of salinity and ocean heat content in the Arctic, particularly in the vicinity of the Arctic river mouths, led to the following hypothesis: regional, multidecadal variations in Arctic sea ice concentration (SIC) can be attributed in part to the AMO through modifications to the temperature and quantity of freshwater inflow into the Arctic. The line of reasoning is that during the warm phase AMO, warmer river water entering the Arctic speeds basal ice melt while the fresh, warm water acts to stabilize the ocean surface layer. As the ice melts, the open surface waters are heated more easily by downward solar and thermal radiation. While sea ice melts annually, the warm phase of the AMO accentuates the ice loss in particular regions of the Arctic. To test this hypothesis, the influence of decadal and multidecadal climate variability on Arctic SIC is investigated through an observationally-based analysis using atmospheric, oceanic, hydroclimatological, and sea ice data sets.

To provide a backdrop for the analyses conducted throughout this dissertation, we first looked at the seasonal climatologies of the Arctic atmosphere, ocean, and sea ice (Chapter 1). Notable regional atmospheric circulation patterns include the Beaufort, Siberian, and North American Highs and the Icelandic and Aleutian Lows. The Aleutian and Icelandic Lows influence the transport of relatively warm North Pacific and North Atlantic waters into the Arctic. Inside the Arctic Basin, the Beaufort High helps to drive the Beaufort Gyre, which along with the Transpolar Drift Stream moves sea ice through and out of the Arctic, respectively. Downwelling radiation, near-surface air temperature and precipitation all exhibit strong seasonal cycles that reach a maximum in summer and a minimum in winter. Near-surface ocean salinity also exhibits strong seasonality, with late spring/early summer inputs of fresh river water entering the Arctic. Likewise, SIC above 15%, the concentration considered to be "ice-covered", exists throughout the Arctic basin from November through May. Sea ice begins to melt near the mouth of Arctic rivers in June and reaches a minimum in September.

This dissertation then investigated the influence of decadal and multidecadal climate variability on September Arctic sea ice (Chapter 2). The Beaufort-Chukchi Sea Area (BCSA) was identified as the region with the largest variability in the North American Arctic, and was the primary focus of the analysis in Chapter 2. To investigate how the SIC minimum is modulated by the natural low-frequency climate variability, linearly-detrended September SIC was regressed on the principal component time series of decadal and multidecadal modes of variability determined from a spatiotemporal analysis of global (20°S-80°N) SSTs (Nigam et al. 2020). The cumulative and individual contributions of each of these modes of variability on the September SIC trend were identified for the 1958-2013 and 1979-2013 time periods. While the non-linear secular trend mode of global SSTs has the largest impact on the declining September SIC trend, natural variability from modes such as the AMO, PDV-PP, and PDV-NP contributed next to the observed declining trend.

To better understand how the connection between the decadal and multidecadal climate variability modes and Arctic sea ice is established, the influence of these natural low-frequency variability modes on the Arctic atmosphere and ocean was investigated at both seasonal and monthly scales (Chapter 3). Linearly-detrended seasonal and monthly mean sea level pressure, ocean heat content, ocean salinity, and

SIC for the full Arctic region were regressed on the low-frequency modes (AMO, PDV-PP, and PDV-NP). Regression anomalies of subsurface ocean temperature and salinity in the Beaufort and Laptev Seas, at the mouths of the Mackenzie and Lena Rivers, were also calculated. To further investigate the link between continental hydrology and SIC, ocean heat content, ocean salinity, and SIC for the full Arctic region, and subsurface temperature and salinity in the Beaufort Sea at the mouth of the Mackenzie River, were regressed on the Mackenzie River discharge anomaly time series.

The main topics of this dissertation are summarized as follows:

- The seasonal climatology of the Arctic atmosphere, ocean, and SIC, based on observations (Chapter 1).
- Decadal-to-Multidecadal September SIC trend in a region of the Beaufort and Chukchi Seas that includes the maximum variability in the North American Arctic (Chapter 2).
- The contribution of five modes of natural low-frequency (decadal-to-multidecadal: PDV-PP, PDV-NP, AMO, LF-NAO and SADV) variability to the overall decline in September Arctic SIC (Chapter 2).
- Decadal-to-multidecadal variations of the Arctic Ocean and Arctic atmosphere in relation to the AMO, PDV-PP, and PDV-NP, with a particular focus on the Beaufort and Laptev Seas (Chapter 3).
- Possible mechanisms linking the AMO, PDV-PP, and PDV-NP to sea ice concentration variability, including through variabilities of atmospheric

circulation, oceanic heat content, and freshwater from rivers flowing into the Arctic basin (Chapter 3).

4.2 Summary

The analysis of the variability of Arctic SIC, and specifically the SIC in the Beaufort-Chukchi Sea Area (BCSA) found that over the 1958-2013 time period, the observed September SIC trend is -12.12% decade^{-1}, while it is -24.12% decade^{-1} over the satellite era from 1979-2013. Additionally, when there are negative September SIC anomalies in the BCSA, there are also negative SIC anomalies in the East Siberian Sea from August through October and in the Laptev and Kara Seas in October. The regression analysis of the July to October monthly SIC on the autumn-only principal component time series of the PDV-PP, PDV-NP, AMO, LF-NAO, and SADV found that positive phases (and trends) of the AMO, SADV, and PDV-NP are associated with SIC loss, while positive phases (and trends) of the PDV-PP and LF-NAO are associated with SIC gain. In the BCSA over the 1979-2013 period, the AMO contributes to SIC decline in the BCSA of nearly 4% decade^{-1}, while the PDV-PP contributes to a decline of just over 3% decade^{-1}. The SADV and PDV-NP each contribute just over 1% decade^{-1} loss each. The LF-NAO contributes a gain of 0.1% decade^{-1}. In the BCSA, the trend in the reconstructed SIC due to the five low-frequency climate variability modes is -9.75% decade^{-1} while the observed trend is -24.12% decade^{-1}. This suggests that low-frequency variability accounts for about 40% of the September SIC loss since 1979.

The research then focused on identifying the mechanisms linking the SST-based modes of climate variability on SIC variability in the Arctic, considering the atmospheric, oceanic, and continental pathways. The monthly climatologies of hydrological parameters (precipitation, evapotranspiration, runoff, and discharge) in the Mackenzie and Lena River basins, and the SIC, ocean surface salinity, and ocean surface temperature in the Beaufort and Laptev Seas were investigated to help identify the sequence of impacts. Melting of winter and spring solid precipitation over the Mackenzie and Lena River basins leads to river runoff peaks in May and June, with peak river discharge near the mouth of the rivers in June. The calculated heat flux from the Mackenzie and Lena Rivers into the Beaufort and Laptev Seas in June is about 2,900 PJ and 5,400 PJ, respectively, with annual totals of about 10,000 PJ and 17,000 PJ. The precipitation maximum occurs at the same time as the evapotranspiration maximum, which leads to a reduction of the amount of water that becomes runoff. The fresh river discharge peak drives the Beaufort and Laptev Sea salinity June minima. Warming of the ocean surface, though, is primarily driven by the reduction in SIC, which allows for heating of the open water and a peak in ocean temperature during the months with the lowest SIC.

Modification of the atmospheric circulation on decadal-to-multidecadal time scales impacts warm inflow from the North Atlantic and North Pacific into the Arctic basin, and also leads to redistribution of sea ice in the Arctic. The positive phase AMO leads to a positive anomaly in MSLP in the central Arctic and the North Pacific. This anomalous circulation pattern is preferential to SIC loss, with increased inflow of relatively warm North Pacific waters through Bering Strait and a warm OHC anomaly in the Chukchi Sea. Along with anomalous lows over land, the anomalous high in the central Arctic causes anomalous easterlies in the Beaufort and

Chukchi Seas, leading to ice transport away from the coast. Transport of ice away from the coast reduces SIC near the coasts, leaving open water and the opportunity for ocean heating by downward solar radiation, increasing the OHC in the Beaufort and Chukchi Seas in summer and autumn. In addition, with the Mackenzie River and the Beaufort Sea, a link to river discharge and continental hydrology is clear. The positive phase AMO leads to warm ocean temperature and salinity anomalies near the surface at the mouth of the Mackenzie River that begins in June and persists through the summer, coinciding with the months of high river discharge. By November, the temperature anomaly has detached from the coast and then progresses further north and begins to descend in the Beaufort Gyre region, building a pool of anomalously warm and fresh water in the Beaufort Sea.

On the Siberian side of the Arctic, the positive phase AMO's positive MSLP anomaly over the central Arctic and Greenland leads to a reduction in the transport of warm North Atlantic waters into the Barents Sea, resulting in a negative OHC anomaly in the Barents and Kara Seas. At the same time, a positive salinity anomaly and normal OHC exist with largely negative SIC anomalies in the Laptev Sea throughout the year (except for small pockets of positive SIC anomalies in summer). The positive salinity anomaly could be caused by a combination of the anomalous high driving anomalous easterlies along the coast and opposing the typical eastward flowing coastal current of relatively fresh surface waters from the Kara Sea into the Laptev Sea and reduced freshwater input from the Lena River. The anomalous atmospheric circulation pattern also leads to ice drift away from the coast, with resulting negative SIC anomalies in the Kara and Laptev Seas in autumn. At the shorter monthly scale, the positive phase AMO leads to a positive salinity/SIC anomaly extending north from the mouth of the Lena River.

The influence of the positive phase of the PDV-PP on atmospheric circulation, ocean temperature and salinity, and SIC is in many ways opposite to that of the AMO. Positive PDV-PP results in a negative MSLP anomaly over the central Arctic, which leads to anomalous westerly winds that cause sea ice divergence and ice drift toward the coasts surrounding the Arctic Ocean. This leads to a positive SIC anomaly in much of the Arctic.

The positive phase PDV-NP leads to reduced SIC around the Arctic in summer and autumn, although small regions of positive SIC anomalies are present at the mouths of the Ob, Yenisey, and Lena Rivers in summer. The anomalous circulation pattern generated by the positive phase PDV-NP on seasonal time scales does not provide a clear answer to the mechanism behind the negative SIC anomalies, as the position of the anomalous low pressure offshore would result in westerly winds along the Siberian coast, accompanied by ice drift toward the coast, and thus more ice instead of less ice. At the shorter monthly time scale, the central Arctic is dominated by a positive MSLP anomaly in September, leading to sea ice convergence toward the central Arctic and the maximum spatial extent of the negative SIC anomaly.

A final analysis was carried out for the Mackenzie River in order to explore its impact on the coastal domain by regressing ocean heat content, ocean salinity, and SIC on the river discharge time series. Increased Mackenzie River discharge was found to be associated with positive OHC and negative salinity anomalies, as expected by the addition of relatively warm, fresh river waters. However, increased

Mackenzie River discharge was also associated with a positive SIC anomaly at the mouth of the Mackenzie River in summer, which is unexpected, given increased river discharge and presumably increased heat flux into the Beaufort Sea. Understanding the impact of the Mackenzie River on the Beaufort Sea is challenging as the surface forcing due to atmospheric circulation anomalies is important for sea ice variability, while the deeper footprint of the river discharge must also be understood. On this regard, it must be said that monitoring the Arctic rivers is essential and must be maintained and expanded now that the fresh water cycle is changing due to increased temperatures. This analysis highlights the complex relationship between the atmospheric circulation in the Arctic, the Arctic Ocean and its marginal seas, continental hydrology, and Arctic sea ice.

4.3 Future Work

To further explore the connection between decadal and multidecadal climate variability and Arctic sea ice, the following should also be investigated:

- Expand analysis to include the impact of natural low-frequency climate variability on sea ice drift data, as this should agree with the impacts on atmospheric circulation, keeping in mind the influence of Ekman transport on the sea ice drift which causes ice to drift slightly to the right of the mean wind direction.
- Investigate vertical profile data collected by ship using CTDs for finer temporal and spatial resolution during the summer melt season to better trace river discharge in the water column in the vicinity of the Mackenzie and other Arctic rivers.

- Investigate how changing precipitation, evapotranspiration, and the difference precipitation minus evapotranspiration patterns may be impacting runoff and river discharge in the Arctic. This is complicated by limited observations and both human and natural impoundment of water changing the timing when water that originally falls as precipitation is discharged into the Arctic Ocean. However, a better understanding of precipitation and evapotranspiration trends and variability in the Arctic would be beneficial not only to improve the understanding of the potential link between continental hydrology and Arctic sea ice, but also to inform resource management particularly for the hydropower industry that leverages Arctic rivers.

References

Aagaard, K., & Carmack, E.C. (1989). The role of sea ice and other fresh water in the Arctic circulation. *Journal of Geophysical Research: Oceans*, 94(C10), 14485-14498. https://doi.org/10.1029/JC094iC10p14485

Amante, C. and Eakins, B.W. (2009). ETOPO1 1 arc-minute global relief model: Procedures, data sources, and analysis. (NOAA Tech. Memo. NESDIS NGDC-24, 25pp.), Retrieved from https://www.ngdc.noaa.gov/mgg/global/relief/ETOPO1/docs/ETOPO1.pdf

Bacon, S., Reverdin, G., Rigor, I. G., and Snaith, H. M. (2002). A freshwater jet on the east Greenland shelf. *Journal of Geophysical Research: Oceans*, 107(C7). https://doi.org/10.1029/2001JC000935

Bacon, S., Marshall, A., Holliday, N. P., Aksenov, Y., and Dye, S. R. (2014). Seasonal variability of the East Greenland Coastal Current. *Journal of Geophysical Research: Oceans*, 119, 3967– 3987. https://doi.org/10.1002/2013JC009279

Bauch, D., Hölemann, J.A., Nikulina, A., Wegner, C., Janout, M.A., Timokhov, L.A., & Kassens, H. (2013). Correlation of river water and local sea-ice melting on the Laptev Sea shelf (Siberian Arctic). *Journal of Geophysical Research: Oceans*, 118, https://doi.org/10.1002/jgrc.20076

Bellomo, K., Murphy, L.N., Cane, M.A., Clement, A.C., & Polvani, L.M. (2018). Historical forcings as main drivers of the Atlantic multidecadal variability in the CESM large ensemble. *Climate Dynamics*, 50(9-10), 3687-3698. https://doi.org/10.1007/s00382-017-3834-3

Bellucci, A., Mariotti, A., & Gualdi, S. (2017). The role of forcings in the twentieth-century North Atlantic multidecadal variability: The 1940-75 North Atlantic cooling case study. *Journal of Climate*, 30(18), 7317-7337. https://doi.org/10.1175/JCLI-D-16-0301.1

Booth, B.B., Dunstone, N.J., Halloran, P.R., Andrews, T., & Bellouin, N. (2012). Aerosols implicated as a prime drive of twentieth-century North Atlantic climate variability. *Nature*, 484(7393), 228-232. https://doi.org/10.1038/nature10946

Boyer, T.P., Antonov, J.I., Baranova, O.K., Coleman, C., Garcia, H.E., Grodsky, A., Johnson, D.R., Locarnini, R.A., Mishonov, A.V., O'Brien, T.D., Paver, C.R., Reagan, J.R., Seidov, D., Smolyar, I.V., & Zweng, M.M. (2013). *World Ocean Database 2013.* Sydney Levitus, Ed.; Alexey Mishonov, Technical Ed.; NOAA Atlas NESDIS 72, 209 pp.

Carmack, E., Winsor, P., Williams, W. (2015). The contiguous panarctic Riverine Coastal Domain: A unifying concept. *Progress in Oceanography*, 139, 13-23. https://doi.org/10.1016/j.pocean.2015.07.014

Carmack, E. C., Yamamoto-Kawai, M., Haine, T. W. N., Bacon, S., Bluhm, B. A., Lique, C., Melling, H., Polyakov, I. V., Straneo, F., Timmermans, M.-L., et al. (2016). Freshwater and its role in the Arctic Marine System: Sources, disposition, storage, export, and physical and biogeochemical consequences in the Arctic and global oceans, *Journal of Geophysical Research: Biogeosciences*, 121, 675– 717. https://doi.org/10.1002/2015JG003140

Castruccio, F.S., Ruprich-Robert, Y., Yeager, S.G., Danabasoglu, G., Msadek, R., & Delworth, T.L. (2019). Modulation of Arctic Sea ice Loss by Atmospheric Teleconnections from Atlantic Multidecadal Variability. *Journal of Climate*, 1419-1441. https://doi.org/10.1175/JCLI-D-18-0307.1

Chapman, W.L. & Walsh, J.E. (1991). Long-range prediction of regional sea ice anomalies in the Arctic, *Weather Forecasting*, 6(2), 271-288.

Chylek, P., Folland, C. K., Lesins, G., Dubey, M. K., & Wang, M. (2009). Arctic air temperature change amplification and the Atlantic Multidecadal Oscillation. *Geophysical Research Letters*, *36*(14), 2–6. https://doi.org/10.1029/2009GL038777

Clement, A., Bellomo, K., Murphy, L.N., Cane, M.A., Mauritsen, T., Rädel, G., & Stevens, B. (2015). The Atlantic multidecadal oscillation without a role for ocean circulation. *Science*, 350(6258), 320-324. https://doi.org/10.1126/science.aab3980

Comiso, J. C. (2006). Abrupt decline in the Arctic winter sea ice cover. *Geophysical Research Letters*, *33*(18), 1–5. https://doi.org/10.1029/2006GL027341

Comiso, J.C., Parkinson, C.L., Gersten, R., & Stock, L. (2008). Accelerated decline in the Arctic sea ice cover, *Geophysical Research Letters*, 35, L01703. https://doi.org/ 10.1029/2007GL031972

Curry, J.A., Ardeel, C.D., & Tian, L. (1990). Liquid water content and precipitation characteristics of stratiform clouds as inferred from satellite microwave measurements. *Journal of Geophysical Research: Atmospheres*, 95, D10, 16659-16671. https://doi.org/10.1029/JD095iD10p16659

Curry, J.A., Rossow, W.B., Randall, D., & Schramm, J.L. (1996). Overview of Arctic Cloud and Radiation Characteristics, *Journal of Climate*, 9, 1731-1764. https://doi.org/10.1175/1520-0442(1996)009<1731:OOACAR>2.0.CO;2

Curry, J.A., & Herman, G.F. (1985). Infrared radiative properties of summertime Arctic stratus clouds. *Journal of Applied Meteorology and Climatology,* 24, 526-538. https://doi.org/10.1175/1520-0450(1985)024<0525:IRPOSA>2.0.CO;2

Danabasoglu, G., Yeager, S.G., Kwon, Y.O., Tribbia, J.J., Phillips, A.S., & Hurrell, J.W. (2012). Variability of the Atlantic multidecadal overturning circulation in CCSM4. *Journal of Climate*, 25(15), 5153-5172. https://doi.org/10.1175-JCLI-D-11-00463.1

Danielson, S.L., Weingartner, T.J., Hedstrom, K.S., Aagaard, K., Woodgate, R., Curchitser, E., Stabeno, P.J. (2014). Coupled wind-forced controls of the Bering-Chukchi shelf circulation and the Bering Strait throughflow: Ekman transport, continental shelf waves, and variations of the Pacific-Arctic sea surface height gradient, *Progress in Oceanography*, 125, 40-61. https://doi.org/10.1016/j.pocean.2014.04.006

Day, J.J., Hargreaves, J.C., Annan, J.D., & Abe-Ouchi, A. (2012). Sources of multi-decadal variability in Arctic sea ice extent, *Environmental Research Letters*, 7, 034011. https://doi.org/10.1088/1748-9326/7/3/034011

Dean, K.G., Stringer, W.J., Ahlnäs, K., Searcy, C., & Weingartner, T. (1994). The influence of river discharge on the thawing of sea ice, Mackenzie River Delta: albedo and temperature analyses, *Polar Research*, 13, 83-94. https://doi.org/10.1111/j.1751-8369.1994.tb00439.x

Dee, D.P., and Coauthors (2011). The ERA-Interim reanalysis: Configuration and performance of the data assimilation system. *Quarterly Journal of the Royal Meteorological Society,* 137, 553-597, https://doi.org/10.1002/qj.828

Delworth, T. L., & Mann, M. E. (2000). Observed and simulated multidecadal variability in the Northern Hemisphere. *Climate Dynamics*, *16*(9), 661–676. https://doi.org/10.1007/s003820000075

Deser, C., & Teng, H. (2008). Evolution of Arctic sea ice concentration trends and the role of atmospheric circulation forcing, 1979-2007. *Geophysical Research Letters*, 35(2), 1–5. https://doi.org/10.1029/2007GL032023

Di Lorenzo, E., Schneider, N., Cobb, K.M., Franks, P.J.S., Chhak, K., Miller, A.J., McWilliams, J.C., Bograd, S.J., Arango, H., Curchitser, E., Powell, T.M., Rivière, P. (2008). North Pacific Gyre Oscillation links ocean climate and ecosystem change. *Geophysical Research Letters*, 35, L08607. https://doi.org/10.1029/2007GL032838

Ding, Q., Schweiger, A., L'Heureux, M., Battisti, D. S., Po-Chedley, S., Johnson, N. C., Blanchard-Wrigglesworth, E., Harnos, K., Zhang, Q., Eastman, R., &

Steig, E.J. (2017). Influence of high-latitude atmospheric circulation changes on summertime Arctic sea ice. *Nature Climate Change,* 7(4), 289–295. https://doi.org/10.1038/nclimate3241

Dunstone, N.J., Smith, D.M., Booth, B.B., Hermanson, L., & Eade, R. (2013). Anthropogenic aerosol forcing of Atlantic tropical storms. *Nature Geoscience*, 6(7), 534-539. https://doi.org/10.1038/ngeo1854

Enfield, D. B., Mestas-Nunez, A.M., & Trimble, P.J. (2001). The Atlantic multidecadal oscillation and its relation to rainfall and river flows in the continental U.S. *Geophysical Research Letters* 28, 2077–2080. https://doi.org/10.1029/2000GL012745

European Centre for Medium-Range Weather Forecasts (2012). ERA-Interim Project, Monthly Means. Research Data Archive at the National Center for Atmospheric Research, Computational and Information Systems Laboratory, Boulder CO. [Available online at http://rda.ucar.edu/datasets/ds627.1.] Accessed 01 March 2015.

Fetterer, F., Knowles, K., Meier, W.N., Savoie, M., and Windnagel, A.K. (2017, updated daily). Sea Ice Index, Version 3. September 1979-2019. Boulder, Colorado USA. NSIDC: National Snow and Ice Data Center. doi: https://doi.org/10.7265/N5K072F8. Accessed 21 September 2020.

Frankcombe, L.M., England, M.H., Kajtar, J.B., Mann, M.E., & Steinman, B.A. (2018). On the choice of ensemble mean for estimating the forced signal in the presence of natural variability. *Journal of Climate*, 31, 5681-5693. https://doi.org/10.1175/JCLI-D-17-0662.1

Frankcombe, L.M., England, M.H., Mann, M.E., & Steinman, B.A. (2015). Separating internal variability from the externally forced climate response. *Journal of Climate*, 28, 8184-8202. https://doi.org/10.1175/JCLI-D-15-0069.1

Ghiggi, G., Humphrey, V., Seneviratne, S.I., Gudmundsson, L. (2019). GRUN: An observations-based global gridded runoff dataset from 1902 to 2014. *Earth System Science Data* 11, 1655-1674, https://doi.org/10.5194/essd-11-1655-2019

Good, S.A., Martin, M.J., & Rayner, N.A. (2013). EN4: quality controlled ocean temperature and salinity profiles and monthly objective analyses with uncertainty estimates, *Journal of Geophysical Research: Oceans*, 118, 6704-6716. https://doi.org/10.1002/2013JC009067. Accessed October 2018.

Guan, B. & Nigam, S. (2008). Pacific sea surface temperatures in the twentieth century: An evolution-centric analysis of variability and trend. *Journal of Climate*, 21, 2790-2809.

Guan, B. & Nigam, S. (2009). Analysis of Atlantic SST variability factoring inter-basin links and the secular trend: Clarified structure of the Atlantic Multidecadal Oscillation. *Journal of Climate*, 22, 4228-4240.

Haine, T.W.N., Curry, B., Gerdes, R., Hansen, E., Karcher, M., Lee, C., Rudels, B., Spreen, G., de Steur, L., Stewart, K.D., & Woodgate, R. (2015). Arctic freshwater export: Status, mechanisms, and prospects. *Global and Planetary Change*, 125, 13-35. https://doi.org/10.1016/j.gloplacha.2014.11.013

Harris, I., Osborn, T.J., Jones, P., & Lister, D. (2020). Version 4 of the CRU TS monthly high-resolution gridded multivariate climate dataset. *Scientific Data*, 7, 109. https://doi.org/10.1038/s41597-020-0453-3

Herman, G.F. & Goody, R. (1976) Formation and persistence of summertime Arctic stratus clouds. *Journal of Atmospheric Science*, 33, 1537-1553. https://doi.org/10.1175/1520-0469(1976)033<1537:FAPOSA>2.0.CO;2

Holmes, R.M., McClelland, J.W., Peterson, B.J., Tank, S.E., Bulygina, E., Eglinton, T.I., Gordeev, V.V., Gurtovaya, T.Y., Raymond, P.A., Repeta, D.J., Staples, R., Striegl, R.G., Zhulidov, A.V., & Zimov, S.A. (2012). Seasonal and Annual Fluxes of Nutrients and Organic Matter from Large Rivers to the Arctic Ocean and Surrounding Seas. *Estuaries and Coasts*, 35(2), 369–382. https://doi.org/10.1007/s12237-011-9386-6

Holmes, R.M., McClelland, J.W., Tank, S.E., Spencer, R.G.M., & Shiklomanov, A.I. (2018). Arctic Great Rivers Observatory. Water Quality Dataset, Version 20180612. https://www.arcticgreatrivers.org/data

Holmes, R.M., Shiklomanov, A.I., Suslova, A., Tretiakov, M., McClelland, J.W., Spencer, R.G.M., & Tank, S.E. (2019). River Discharge [in "State of the Climate in 2018"]. *Bulletin of the American Meteorological Society*, 100(9), 161-163. https://doi.org/10.1175/2019BAMSStateoftheClimate.1

Hurrell, J.W. (1995). Decadal trends in the North Atlantic Oscillation: Regional temperatures and precipitation. *Science*, 269, 676-679. https://doi.org/10.1126/science.269.5224.676

Jones, E.P., Anderson, L.G., Jutterströmb, S., & Swift, J.H. (2008). Sources and distribution of freshwater in the East Greenland Current, *Progress in Oceanography*, 78, 37-44. https://doi.org/10.1016/j.pocean.2007.06.003

Kalnay, E., Kanamitsu, M., Kistler, R., Collins, W., Deaven, D., Gandin, L., Iredell, M., Saha, S., White, G., Woollen, J., Zhu, Y., Leetmaa, A., Reynolds, B., Chelliah, M., Ebisuzaki, W., Higgins, W., Janowiak, J., Mo, K.C., Ropelewski, C., Wang, J., Jenne, R., and Joseph, D. (1996) The NCEP/NCAR

40-Year Reanalysis Project. *Bulletin of the American Meteorological Society,* 77, 437-472. https://doi.org/10.1175/1520-0477(1996)077<0437:TNYRP>2.0.CO;2

Kavvada, A., Ruiz-Barradas, A., & Nigam, S. (2013). AMO's structure and climate footprint in observations and IPCC AR5 climate simulations. *Climate Dynamics*, 41, 1345-1364. https://doi.org/10.1007/s00382-013-1712-1

Kawai, Y., Osafune, S., Masuda, S., Komuro, Y. (2018). Relations between salinity in the northwest Bering Sea, the Bering Strait throughflow and sea surface height in the Arctic Ocean. *Journal of Oceanography*, 74, 239-261. https://doi.org/10.1007/s10872-017-0453-x

Kay, J.E., L'Ecuyer, T., Gettelman, A., Stephens, G., O'Dell, C. (2008). The contribution of cloud and radiation anomalies to the 2007 Arctic sea ice extent minimum. *Geophysical Research Letters,* 35, L08503. https://doi.org/10.1029/2008GL033451.

Kerr, R.A. (2000). A North Atlantic Climate Pacemaker for the Centuries. *Science*, 288(5473), 1984-1985. https://doi.org/10.1126/science.288.5473.1984

Knight, J.R., Allan, R.J., Folland, C.K., Vellinga, M., & Mann, M.E. (2005). A signature of persistent natural thermohaline circulation cycles in observed climate. *Geophysical Research Letters,* 32, L20708. https://doi.org/10.1029/2005GL024233

Kolling, H. M., Stein, R., Fahl, K., Perner, K., & Moros, M. (2017). Short-term variability in late Holocene sea ice cover on the East Greenland Shelf and its driving mechanisms. *Palaeogeography, Palaeoclimatology, Palaeoecology*, 485, 336–350. https://doi.org/10.1016/j.palaeo.2017.06.024

Lammers, R.B., Pundsack, J.W., & Shiklomanov, A.I. (2007a). ART-Russia River Temperature, Arctic Data Center, https://doi.org/10.5065/D60K26P0

Lammers, R.B., Pundsack, J.W., & Shiklomanov, A.I. (2007b). Variability in river temperature, discharge, and energy flux from the Russian pan-Arctic landmass. *Journal of Geophysical Research: Biogeosciences*, 112, G04S59. https://doi.org/10.1029/2006JG000370

Lammers, R.B., Shiklomanov, A.I., Vörösmarty, C.J., Fekete, B.M., & Peterson, B.J. (2001). Assessment of contemporary Arctic river runoff based on observational discharge records. *Journal of Geophysical Research: Atmospheres*, 106, 3321-3334. https://doi.org/10.1029/2000JD900444

Lapointe, F., Francus, P., Lamoureux, S. F., Vuille, M., Jenny, J. P., Bradley, R. S., Massa, C. (2017). Influence of North Pacific decadal variability on the western Canadian Arctic over the past 700 years. *Climate of the Past*, *13*(4), 411–420. https://doi.org/10.5194/cp-13-411-2017

Levitus, S., Antonov, J.I., Boyer, T.P., Locarnini, R.A., Garcia, H.E., & Mishonov, A.V. (2009a). Global ocean heat content 1955-2008 in light of recently revealed instrumentation problems. *Geophysical Research Letters*, 36, L07608. https://dx.doi.org/10.1029/2008GL037155

Levitus, S., Matishov, G., Seidov, D., & Smolyar, I. (2009b). Barents Sea multidecadal variability. *Geophysical Research Letters*, *36*(19), 1–5. https://doi.org/10.1029/2009GL039847

Liu, B., Yang, D., Ye, B., Berezovskaya, S. (2005). Long-term open-water season stream temperature variations and changes over Lena river basin in Siberia. *Global and Planetary Change*, 48(1-3), 96-111. https://dx.doi.org/10.1016/j.gloplacha.2004.12.007

Mahajan, S., Zhang, R., & Delworth, T. L. (2011). Impact of the atlantic meridional overturning circulation (AMOC) on arctic surface air temperature and sea ice variability. *Journal of Climate*, *24*(24), 6573–6581. https://doi.org/10.1175/2011JCLI4002.1

Mann, M.E. & Emanuel, K.A. (2006). Atlantic hurricane trends linked to climate change. *Eos*, *Transactions American Geophysical Union,* 87(24), 233-241. https://doi.org/10.1029/2006EO240001

Mann, M.E., Steinman, B.A., Brouillette, D.J., & Miller, S.K. (2021). Multidecadal climate oscillations during the past millennium driven by volcanic forcing. *Science*, 371 (6533), 1014-1019. https://doi.org/10.1126/science.abc5810

Mann, M.E., Steinman, B.A., & Miller, S.K. (2020). Absence of internal multidecadal and interdecadal oscillations in climate model simulations. *Nature Communications*, 11, 49. https://doi.org/10.1038/s41467-019-13823-w

Mann, M.E., Steinman, B.A., & Miller S.K. (2014). On forced temperature changes, internal variability and the AMO. *Geophysical Research Letters*, 41, 3211-3219. https://doi.org/10.1002/2014GL059233

Mantua, N.J, & Hare, S.R., (2002). The Pacific decadal oscillation. *Journal of Oceanography*, 58(1), 35-44. https://doi.org/10.1023/A:1015820616384

Mantua, N.J., Hare, S.R., Zhang, Y., Wallace, J.M., & Francis, R.C. (1997). A Pacific interdecadal climate oscillation with impacts on salmon production. *Bulletin of the American Meteorological Society*, 78, 1069-1079. https://doi.org/10.1175/1520-0477(1997)078<1069:APICOW>2.0.CO;2

Maslanik, J., Drobot, S., Fowler, C., Emery, W., & Barry, R. (2007a). On the Arctic climate paradox and the continuing role of atmospheric circulation in affecting sea ice conditions. *Geophysical Research Letters*, 34(3), 2–5. https://doi.org/10.1029/2006GL028269

Maslanik, J. A., Fowler, C., Stroeve, J., Drobot, S., Zwally, H.J., Yi, D., & Emery, W.J. (2007b). A younger, thinner Arctic ice cover: Increased potential for rapid, extensive sea ice loss. *Geophysical Research Letters*, 34, L24501. https://doi.org/10.1029/2007GL032043

Maslowski, W., Marble, D., Walczowski, W., & Semtner, A. (2001). On large-scale shifts in the Arctic Ocean and sea-ice conditions during 1979‒98. *Annals of Glaciology,* 33, 545-550. doi:10.3189/172756401781818978

Maslowski, W., Newton, B., Schlosser, P., Semtner, A., & Martinson, D. (2000). Modeling recent climate variability in the Arctic Ocean. *Geophysical Research Letters*, 27(22), 3743-3746. https://doi.org/10.1029/1999GL011227

Matthews, J.B. & Stringer, W.J. (1984). Spring break-up and flushing of an Arctic lagoon estuary. *Journal of Geophysical Research: Atmospheres,* 89(C2), 2073-2079. https://doi.org/10.1029/JC089iC02p02073

Matsuura, K. & Willmott, C.J. (2018a). Terrestrial Precipitation: 1900-2017 Gridded Monthly Time Series (Version 5.01), http://climate.geog.udel.edu/~climate/html_pages/Global2017/README.GlobalTsP2017.html

Matsuura, K. & Willmott, C.J. (2018b). Terrestrial Water Budget Data Archive: Monthly Time Series (1900-2017) (Version 4.01), http://climate.geog.udel.edu/~climate/html_pages/Global2017/README.GlobalWbTs2017.html.

McCarthy, G.D., Haigh, I.D., Hirschi, J.J.M., Grist, J.P., & Smeed, D.A. (2015). Ocean impact on decadal Atlantic climate variability revealed by sea-level observations. *Nature*, 521(7553), 508-510. https://doi.org/10.1038/nature14491

McClelland, J.W., Holmes, R.M., Dunton, K.H., & Macdonald, R.W. (2012). The Arctic Ocean estuary. *Estuaries and Coasts, 35,* 353-368. https://doi.org/10.1007/s12237-010-9357-3

McClelland, J.W., Tank, S.E., Spencer, R.G.M., & Shiklomanov, A.I. (2015). Coordination and sustainability of river observing activities in the Arctic. *Arctic*, 68, 59-68. https://doi.org/10.14430/arctic4448

Meehl, G. A., Chung, C. T. Y., Arblaster, J.M., Holland, M.M. & Bitz, C.M. (2018). Tropical decadal variability and the rate of Arctc sea ice decrease. *Geophysical Research Letters*, 45, 11,326–11,333. https://doi.org/10.1029/2018GL079989

Menne, M.J., Durre, I., Vose, R.S., Gleason, B.E., & Houston, T.G. (2012). An overview of the Global Historical Climatology Network-Daily Database. *Journal of Atmospheric and Oceanic Technology*, 29, 897-910. https://doi.org/10.1175/JTECH-D-11-00103.1

Miles, M.W., Divine, D.V., Furevik, T., Jansen, E., Moros, M., & Ogilvie, A.E.J. (2014). A signal of persistent Atlantic multidecadal variability in Arctic sea ice. *Geophysical Research Letters*, 41, 463-469. https://doi.org/10.1002/2013GL058084

Morison, J., Kwok, R., Peralta-Ferriz, C., Alkire, M., Rigor, I., Andersen, R., & Steele, M. (2012). Changing Arctic Ocean freshwater pathways. *Nature*, 481, 66-70. https://doi.org/10.1038/nature10705

Moros, M., Andrews, J. T., Eberl, D. D., & Jansen, E. (2006). Holocene history of drift ice in the northern North Atlantic: Evidence for different spatial and temporal modes. *Paleoceanography*, *21*(2), 1–10. https://doi.org/10.1029/2005PA001214

Mulligan, R.P., & Perrie, W. (2019). Circulation and structure of the Mackenzie River plume in the coastal Arctic Ocean. *Continental Shelf Research*, 177, 59-68. https://doi.org/10/1016/j.csr.2019.03.006

Murphy, L.N., Bellomo, K., Cane, M., & Clement, A. (2017). The role of historical forcings in simulating the observed Atlantic multidecadal oscillation. *Geophysical Research Letters*, 44, 2472-2480. https://doi.org/10.1002/2016GL071337

Mysak, L. (2001). Patterns of Arctic Circulation. *Science*, 293, 1269-1270. https://doi.org/10.1126/science.1064217

Newton, R., Schlosser, P., Mortlock, R., Swift, J., & MacDonald, R. (2013). Canadian Basin freshwater sources and changes: Results from the 2005 Arctic Ocean section. *Journal of Geophysical Research: Oceans*, 118, 2133-2154. http://doi.org/10.1002/jgrc.20101

Nghiem, S.V., Hall, D.K., Rigor, I.G., Li, P., & Neumann, G. (2014). Effects of Mackenzie River discharge and bathymetry on sea ice in the Beaufort Sea. *Geophysical Research Letters*, 41, 873-879. https://doi.org/10.1002/2013GL058956

Nghiem, S.V., Rigor, I.G., Perovich, D.K., Clemente-Colón, P., Weatherly, J.W., & Neumann, G. (2007). Rapid reduction of Arctic perennial sea ice. *Geophysical Research Letters*, L19504. https://doi.org/10.1029/2007GL031138

Nicolle, M., Debret, M., Massei, N., Colin, C., deVernal, A., Divine, D., et al. (2017). Climate variability in subarctic area for the last two millennia. *Climate of the Past Discussions*, (March), 1–24. https://doi.org/10.5194/cp-2017-33

Nigam, S., Guan, B., & Ruiz-Barradas, A. (2011). Key role of the Atlantic Multidecadal Oscillation in 20th century drought and wet periods over the Great Plains. *Geophysical Research Letters*, 38, L16713. https://doi.org/10.1029/2011GL048650

Nigam, S., Sengupta, A., & Ruiz-Barradas, A. (2020). Atlantic-Pacific links in observed multidecadal SST variability: Is the Atlantic Multidecadal Oscillation's phase reversal orchestrated by the Pacific Decadal Oscillation? *Journal of Climate*, 33, 5479-5505. https://doi.org/10.1175/JCLI-D-19-0880.1

Nikiforov, E.G. and A.O. Shpaikher, Formation of a large-scale oscillation of the hydrological regime of the Arctic Ocean, L. *Gidrometizdat*, p. 270, 1980.

Oelsmann, J., Borchert, L., Hand, R., Baehr, J., & Jungclaus, J.H. (2020). Linking ocean forcing and atmospheric interactions to Atlantic multidecadal variability in MPI-ESM1.2. *Geophysical Research Letters*, 47(10). https://doi.org/10.1029/2020GL087259

Ogi, M. & Wallace, J.M. (2007). Summer minimum Arctic sea ice extent and the associated summer atmospheric circulation. *Geophysical Research Letters* 34, L12705. https://doi.org/10.1029/2007GL029897

Ogi, M., Rigor, I.G., McPhee, M.G., & Wallace, J.M. (2008). Summer retreat of Arctic sea ice: Role of summer winds. *Geophysical Research Letters* 35, L24701. https://doi.org/10.1029/2008GL035672

Osadchiev, A.A., Pisareva, M.N., Spivak, E.A., Shchuka, S.A., & Semiletov, I.P. (2020). Freshwater transport between the Kara, Laptev, and East-Siberian seas. *Scientific Reports,* 10, 13041. https://doi.org/10.1038/s41598-020-70096-w

Otterå, O.H., Bentsen, M., Drange, H., & Suo, L. (2010). External forcing as a metronome for Atlantic multidecadal variability since 1870. *Nature Geoscience,* 3, 688-694. https://doi.org/10.1038/ngeo955

Overland, J. E., & Wang, M. (2005). The Arctic climate paradox: The recent decrease of the Arctic Oscillation. *Geophysical Research Letters*, 32(6), 1–5. https://doi.org/10.1029/2004GL021752

Overland, J.E., & Wang, M. (2010). Large-scale atmospheric circulation changes are associated with the recent loss of Arctic sea ice. *Tellus*, 62A, 1-9, https://doi.org/10.1111/j.1600-0870.2009.00421.x

Park, H., Watanabe, E., Kim, Y., Polyakov, I., Oshima, K., Zhang, X., Kimball, J.S., & Yang, D. (2020). Increasing riverine heat influx triggers Arctic sea ice decline and oceanic and atmospheric warming. *Science Advances*, 6(45), eabc4699. https://doi.org/10.1126/sciadv.abc4699

Parkinson, C.L. & Comiso, J.C., (2013). On the 2012 record low Arctic sea ice cover: Combined impact of preconditioning and an August storm. *Geophysical Research Letters,* 40, 1-6. https://doi.org/10.1002/grl.50349

Polyakov, I.V., Alekseev, G.V., Bekryaev, R.V., Bhatt, U.S., Colony, R., Johnson, M.A., Karklin, V.P., Walsh, D., & Yulin, A.V. (2003a). Long-term ice variability in Arctic marginal seas. *Journal of Climate*, 16(12), 2078–2085. https://doi.org/10.1175/1520-0442(2003)016<2078:LIVIAM>2.0.CO;2

Polyakov, I.V., Alekseev, G.V., Timokhov, L.A., Bhatt, U.S., Colony, R.L., Simmons, H. L., Walsh, D., Walsh, J.E., & Zakharov, V.F. (2004). Variability of the intermediate Atlantic water of the Arctic Ocean over the last 100 years. *Journal of Climate*, 17(23), 4485–4497. https://doi.org/10.1175/JCLI-3224.1

Polykov, I.V., Beszczynska, A., Carmack, E.C., Dmitrenko, I.A., Fahrbach, E., Frolov, I.E., Gerdes, R., Hansen, E., Holfort, J., Ivanov, V.V., Johnson, M.A., Karcher, M., Kauker, F., Morison, J., Orvik, K.A., Schauer, U., Simmons, H.L., Skagseth, Ø., Sokolov, V.T., Steele, M., Timokhov, L.A., Walsh, D., & Walsh, J.E. (2005). One more step toward a warmer Arctic. *Geophysical Research Letters*, 32, L17605. https://doi.org/10.1029/2005GL023740

Polyakov, I., Walsh, D., Dmitrenko, I., Colony, R. L., & Timokhov, L. A. (2003b). Arctic Ocean variability derived from historical observations. *Geophysical Research Letters*, 30(6), 1998–2001. https://doi.org/10.1029/2002GL016441

Prowse, T., Bring, A., Mård, J., & Carmack, E. (2015). Arctic Freshwater Synthesis: Introduction. *Journal of Geophysical Research: Biogeosciences*, 120, 2121-2131. https://doi.org/10.1002/2015JG003127

Reusen, J., van der Linden, E. & Bintanja, R. (2019). Differences between Arctic interannual and decadal variability across climate states. *Journal of Climate*, 32, 6035-6050. https://doi.org/10.1175/JCLI-D-18-0672.1

Rigor, I.G., & Wallace, J.M. (2004). Variations in the age of sea-ice and summer sea-ice extent. *Geophysical Research Letters*, 31, L09401. https://doi.org/10.1029/2004GL019492

Rudels, B., L. Anderson, P. Eriksson, E. Fahrbach, M. Jakobsson, E.P. Jones, H. Melling, S. Prinsenberg, U. Schauer, and T. Yao (2012), Observations in the ocean, in *Arctic Climate Change: The ACSYS Decade and Beyond, Atmospheric and Oceanographic Sciences Library,* vol. 43, chap. 4, edited by P. Lemke and H.-W. Jacobi, pp. 117-198, Springer, Dordrecht, Netherlands.

Schneider, U., Becker, A., Finger, P., Meyer-Christoffer, A., & Ziese, M. (2018). GPCC Full Data Monthly Product Version 2018 at 0.25°: Monthly Land-Surface Precipitation from Rain-Gauges built on GTS-based and Historical Data. https://doi.org/ 10.5676/DWD_GPCC/FD_M_V2018_025

Screen, J.A. (2013). Influence of Arctic sea ice on European summer precipitation. *Environmental Research Letters*, 8, 044015. https://doi.org/10.1088/1748-9326/8/4/044015

Screen, J. A., & Francis, J. A. (2016). Contribution of sea-ice loss to Arctic amplification is regulated by Pacific Ocean decadal variability. *Nature Climate Change*, *6*(9), 856–860. https://doi.org/10.1038/nclimate3011

Searcy, C., Dean, K., & Stringer, W. (1996). A river-coastal sea ice interaction model: Mackenzie River Delta. *Journal of Geophysical Research: Oceans*, 111(C4), 8885-8894. https://doi.org/10.1029/96JC00120

Serreze, M.C. & Barrett, A.P. (2011). Characteristics of the Beaufort Sea High. *Journal of Climate*, 24, 159-182. https://doi.org/10.1175/2010JCLI3636.1

Serreze, M.C., Barrett, A.P., Slater, A.G., Woodgate, R.A., Aagaard, K., Lammers, R.B., Steele, M., Moritz, R., Meredith, M., & Lee, C.M. (2006). The large-scale freshwater cycle of the Arctic. *Journal of Geophysical Research: Oceans*, 111, C11010. https://doi.org/10.1029/2005JC003424

Serreze, M.C., & Francis, J. A. (2006). The arctic amplification debate. *Climatic Change*, *76*(3–4), 241–264. https://doi.org/10.1007/s10584-005-9017-y

Serreze, M.C., Holland, M. M., & Stroeve, J. C. (2007). Perspectives on the Arctic's Shrinking Sea-Ice Cover. *Science*, 315(2), 1533–1537. https://doi.org/10.1126/science.1139426

Shiklomanov, A.I., Holmes, R.M., McClelland, J.W., Tank, S.E., & Spencer, R.G.M. (2018). Arctic Great Rivers Observatory. Discharge Dataset, Version 20191231. https://www.arcticrivers.org/data

Shiklomanov, A.I. & Lammers, R.B. (2014). River ice responses to a warming Arctic – recent evidence from Russian rivers. *Environmental Research Letters,* 9, 035008. https://doi.org/10.1088/1748-9326/9/3/035008

Shimada, K., Kamoshida, T., Itoh, M., Nishino, S., Carmack, E., McLaughlin, F., Zimmerman, S., & Proshutinsky, A. (2006). Pacific Ocean inflow: Influence on catastrophic reduction of sea ice cover in the Arctic Ocean. *Geophysical Research Letters*, 33, L08605. https://doi.org/10.1029/2005GL025624

Shpaikher, A.O., Fedorova, Z.P., and Yankina, Z.S. (1972). Inter-annual variations of the hydrological regime of the seas of the Siberian shelf as a response to atmospheric processes. *Proceedings of the Arctic and Antarctic Research Institute*, 306, 5-17.

Smedsrud, L. H., Halvorsen, M. H., Stroeve, J. C., Zhang, R., & Kloster, K. (2017). Fram Strait sea ice export variability and September Arctic sea ice extent over the last 80 years. *Cryosphere*, 11(1), 65–79. https://doi.org/10.5194/tc-11-65-2017

Stroeve, J., Serreze, M., Drobot, S., Gearheard, S., Holland, M., Maslanik, J., Meier, W., & Scambos, T. (2008). Arctic Sea Ice Extent Plummets in 2007. *EOS Transactions American Geophysical Union*, 89(2), 13-14. https://doi.org/10.1029/2008EO020001

Sutton, R.T., McCarthy, G.D., Robson, J., Sinha, B., Archibald, A.T., & Gray, L.J. (2018). Atlantic multidecadal variability and the UK ACSIS program. *Bulletin of the American Meteorological Society*, 99(2), 415-425. https://doi.org/10.1175/BAMS-D-16-0266.1

Thompson, D.W.J. & Wallace, J.M. (1998). The Arctic Oscillation signature in the wintertime geopotential height and temperature fields. *Geophysical Research Letters*, 25, 1297-1300.

Titchner, H.A. & Rayner, N.A. (2014). The Met Office Hadley Centre sea ice and sea surface temperature data set, version 2: 1. Sea ice concentrations. *Journal of Geophysical Research: Atmospheres,* 119, 2864–2889. https://doi.org/10.1002/2013JD020316

Treshnikov, A.F. (1985). Arctic Atlas (in Russian), 204 pp., Arkt.-Antarkt. Nauchno-Issled. Inst., Moscow.

University of East Anglia Climatic Research Unit; Harris, I.C.; Jones, P.D. (2017): CRU TS4.01: Climatic Research Unit (CRU) Time-Series (TS) version 4.01 of high-resolution gridded data of month-by-month variation in climate (Jan. 1901- Dec. 2016). Centre for Environmental Data Analysis, *04 December 2017*. doi:10.5285/58a8802721c94c66ae45c3baa4d814d0.

University of East Anglia Climatic Research Unit; Harris, I.C.; Jones, P.D. (2019): CRU TS4.02: Climatic Research Unit (CRU) Time-Series (TS) version 4.02

of high-resolution gridded data of month-by-month variation in climate (Jan. 1901- Dec. 2017). Centre for Environmental Data Analysis, *01 April 2019*. doi:10.5285/b2f81914257c4188b181a4d8b0a46bff.

van Vliet, M.T.H., Ludwig, F., Zwolsman, J.J.G., Weedon, G.P., & Kabat, P. (2011). Global river temperatures and sensitivity to atmospheric warming and changes in river flow. *Water Resources Research*, 47, W02544. https://doi.org/10.1029/2010WR009198

Walsh, J.E. (1978). A data set on Northern Hemisphere sea ice extent. World Data Center-A for Glaciology (Snow and Ice), Glaciological Data, Report GD-2, part 1, 49-51.

Walsh, J.E. & Chapman, W.L. (2001). Twentieth-century sea ice variations from observational data. *Annals of Glaciology*, 33, 444-448. https://doi.org/10.3189/172756401781818671

Walsh, J.E., Chapman, W.L., & Fetterer, F. (2015, updated 2016). Gridded monthly sea ice extent and concentration, 1850 onwards, Version 1.1. Boulder, Colorado USA: National Snow and Ice Data Center. Digital media. http://dx.doi.org/10.7265/N5833PZ5

Walsh, J.E., Fetterer, F., Stewart, J.S., & Chapman, W.L. (2017). A database for depicting Arctic sea ice variations back to 1850. *Geographical Review*, 107 (1), 89-107. https://doi.org/10.1111/j.1931-0846.2016.12195.x

Walsh, J.E. & Johnson, C.M. (1978). Analysis of Arctic sea ice fluctuations 1953-1977. *Journal of Physical Oceanography*, 9(3), 580-591. https://doi.org/10.1175/1520-0485(1979)009<0580:AAOASI>2.0.CO;2

Webb, B.W., & Nobilis, F. (1994). Water temperature behavior in the River Danube during the 20th century. *Hydrobiologia*, 291(2), 105-113. https://doi.org/10.1007/BF00044439

Webb, B.W., & Nobilis, F. (1997). Long-term perspective on the nature of the air-water temperature relationship: a case study. *Hydrological Processes*, 11(2), 137-147. https://doi.org/10.1002/(SICI)1099-1085(199702)11:2<137::AID-HYP405>3.0.CO;2-2

Webb, B.W., & Walling, D.E. (1993). Temporal variability in the impact of river regulation on thermal regime and some biological implications. *Freshwater Biology*, 29(1), 167-182. https://doi.org/10.1111/j.1365-2427.1993.tb00752.x

Weingartner, T. J., Danielson, S., Sasaki, Y., Pavlov, V., and Kulakov, M. (1999). The Siberian Coastal Current: A wind- and buoyancy-forced

Arctic coastal current. *Journal of Geophysical Research: Oceans*, 104(C12), 29697– 29713. https://doi.org/10.1029/1999JC900161

Willmott, C.J. & Robeson, S.M. (1995). Climatologically aided interpolation (CAI) of terrestrial air temperature. *International Journal of Climatology*, 15(2), 221-229. https://doi.org/10.1002/joc.3370150207

Willmott, C.J., Rowe, C.M., & Mintz, Y. (1985). Climatology of the Terrestrial Seasonal Water Cycle. *Journal of Climatology*, 5, 589-606. https://doi.org/10.1002/joc.3370050602

Wills, R.C., Armour, K.C., Battisti, D.S., & Hartmann, D.L. (2019). Ocean-atmosphere dynamical coupling fundamental to the Atlantic Multidecadal Oscillation. *Journal of Climate*, 32(1), 251-272. https://doi.org/10.1175/JCLI-D-18-0269.1

Woodgate, R.A., Weingartner, T.J., & Lindsay, R. (2012). Observed increases in Bering Strait oceanic fluxes from the Pacific to the Arctic from 2001 to 2011 and their impacts on the Arctic Ocean water column. *Geophysical Research Letters*, 39(L24603). https://doi.org/10.1029/2012GL054092

Yang, D., Marsh, P., & Ge, S. (2014). Heat flux calculations for Mackenzie and Yukon Rivers. *Polar Science*, 8, 232-241. https://dx.doi.org/10.1016/j.polar.2014.05.001

Yang, X.-Y., Wang, G., & Keenlyside, N. (2020). The Arctic sea ice extent change connected to Pacific decadal variability. *Cryosphere*, 14, 693-708. https://doi.org/10.5194/tc-14-693-2020

Yu, L., Zhong, S., Winkler, J. A., Zhou, M., Lenschow, D. H., Li, B., Wang, X., & Yang, Q. (2017). Possible connections of the opposite trends in Arctic and Antarctic sea-ice cover. *Scientific Reports*, 7. https://doi.org/10.1038/srep45804

Yu, L., Zhong, S., Zhou, M., Lenschow, D.H., Sun, B. (2019). Revisiting the linkages between the variability of atmospheric circulations and Arctic melt-season sea ice cover at multiple time scales. *Journal of Climate*, 32, 1461-1482. https://doi.org/10.1175/JCLI-D-18-0301.1

Zanchettin, D., Rubino, A., Matei, D., Bothe, O., & Jungclaus, J.H. (2013). Multidecadal-to-centennial SST variability in the MPI-ESM simulation ensemble for the last millennium. *Climate Dynamics*, 40, 1301-1318. https://doi.org/10.1007/s00382-012-1361-9

Zhang, R. (2015). Mechanisms for low-frequency variability of summer Arctic sea ice extent. *Proceedings of the National Academy of Sciences*, 112(15), 4570–

4575. https://doi.org/10.1073/pnas.1422296112

Zhang, R. (2017). On the persistence and coherence of subpolar sea surface temperature and salinity anomalies associated with the Atlantic multidecadal variability. *Geophysical Research Letters*, 44, 7865-7875. https://doi.org/10.1002/2017GL074342

Zhang, S., Gan, T.Y., & Bush, A.B.G. (2020). Variability of Arctic Sea Ice Based on Quantile Regression and the Teleconnection with Large-Scale Climate Patterns. *Journal of Climate*, 33, 4009-4025. https://doi.org/10.1175/JCLI-D-19-0375.1

Zhang, L. & Li, T. (2017) Physical processes responsible for the interannual variability of sea ice concentration in Arctic in boreal autumn since 1979. *Journal of Meteorological Research*, 31, 468-475. https://doi.org/10.1007/s13351-017-6105-7

Zhang, R., Sutton, R., Danabasoglu, G., Kwon, Y.-O., Marsh, R., Yeager, S. G., Amrhein, D.E., & Little, C.M. (2019). A review of the role of the Atlantic Meridional Overturning Circulation in Atlantic Multidecadal Variability and associated climate impacts. *Reviews of Geophysics*, 57, 316– 375. https://doi.org/10.1029/2019RG000644

Zhang, X. & Walsh, J.E. (2006). Towards a seasonally ice-covered Arctic Ocean: Scenarios from the IPCC AR4 simulations. *Journal of Climate*, 19(9), 1730-1747. https://doi.org/10.1175/JCLI3767.1

Zhang, J. & Zhang, R. (2015). On the evolution of Atlantic meridional overturning circulation footprint and implications for decadal predictability in the North Atlantic. *Geophysical Research Letters*, 42, 5419-5426. https://doi.org/10.1002/2015GL064596